Optoelectronic Properties of Novel Semiconductors



Christopher Lawrence Davies

St Cross College

University of Oxford

A thesis submitted for the degree of

Doctor of Philosophy

Trinity 2018

Abstract

Metal-halide perovskites and nanowires are both examples of novel semiconductors with the potential to further our light-harvesting capabilities. Realising their potential will rest on understanding their fundamental optoelectronic properties.

Metal-halide perovskites have been implemented in efficient photovoltaic devices whose efficiencies are rapidly improving. Once the Shockley-Queisser limit is reached, charge-carrier extraction will be limited only by radiative bimolecular recombination of electrons with holes. Yet, this fundamental process, is still poorly understood in these semiconductors. Here, bimolecular charge-carrier recombination in methylammonium lead triiodide perovskite can be fully explained as the inverse process of absorption. By correctly accounting for contributions to the absorption from excitons and electron-hole continuum states, the van-Roosbroeck-Shockley relation can be utilized to determine bimolecular recombination rate constants from absorption spectra. The sharpening of photon, electron and hole distribution functions is shown to significantly enhances bimolecular charge recombination as the temperature is lowered, mirroring trends in transient spectroscopy. The findings provide vital understanding of band-to-band recombination processes in this hybrid perovskite, which comprise direct, fully radiative transitions between thermalised electrons and holes.

While methylammonium lead triiodide ($MAPbI_3$) has received much attention, formamidinium lead triiodide ($FAPbI_3$) has been less explored. This thesis examines the temperature-dependent phonon absorption, exciton binding energy, and band-gap of $FAPbI_3$ polycrystalline thin films and finds remarkably different behaviour across the β–γ phase transition

compared with $MAPbI_3$. While $MAPbI_3$ has shown abrupt changes in the band-gap and exciton binding energy, values for $FAPbI_3$ vary smoothly over a range of 100 – 160 K in accordance with a more gradual transition. In addition this thesis finds that the charge-carrier mobility in $FAPbI_3$ exhibits a clear $T^{-0.5}$ trend with temperature, in excellent agreement with theoretical predictions for halide perovskites whose electron-phonon interactions are governed by the Fröhlich mechanism, but in contrast to the $T^{-1.5}$ dependence previously observed for $MAPbI_3$. Finally, intra-excitonic transitions were directly observed in $FAPbI_3$ at low temperature, from which a low exciton binding energy is determined of only 5.3 meV at 10 K.

Very low disorder is observed in high quality quantum well tubes (QWT) in GaAs-$Al_{0.4}Ga_{0.6}As$ core-multishell nanowires. Room-temperature photoluminescence spectra were measured from 150 single nanowires enabling a full statistical analysis of both intra- and inter-nanowire disorder. By modelling individual nanowire spectra, each nanowire can be assigned a quantum well tube thickness, a core disorder parameter and a QWT disorder parameter to each nanowire. A strong correlation was observed between disorder in the GaAs cores and disorder in the GaAs QWTs, which indicates that variations in core morphology effectively propagate to the shell layers. This highlights the importance of high quality core growth prior to shell deposition. Furthermore, variations in QWT thicknesses for different facet directions was found to be a likely cause of intra-wire disorder, highlighting the need for accurate shell growth.

This thesis, along with the work produced during its making, helps to contribute to our fundamental understanding of the optoelectronic properties of metal-halide perovskites and III-V nanowires.

Dedication

Firstly, I would like to thank my supervisor Prof. Michael B. Johnston for his continued support, guidance and tuition throughout my time at Oxford. I would also like to thank my effective (honorary) co-supervisor Prof. Laura M. Herz for her dedicated supervision and teachings both in science and communication of research. I am greatly indebted to Dr. Patrick Parkinson, my co-supervisor for my Masters, who helped excel my experimental and theoretical understandings and was always willing to discuss my queries in depth.

Scientific research is not a lone effort; I would like to show my appreciation for all members of the Johnston and Herz groups for their help, encouragement, discussions, ideas, curiosity, and support throughout my time as a graduate student - (Post-Docs and Alumni): Rebecca Milot, Jessica Boland, Juliane Gong, Chris Menelaou, James Ball, Laura M. Maestro, Sonia Conesa-Boj, and Qianqian Lin - (My fellow starters): Jay Patel, Adam Wright, Elizabeth Parrott and Waqaas Rehman - (Current Members): Timothy Crothers, Djamshid Damry, Sabrina Sterzl, Juliane Borchert, Chelsea Xia, Alex Knight, Kimberley Savill, Hannah Eggimann, Leo Buizza, and Kilian Lohmann. I would like to extend special thanks to those who have stayed late or come in early to help with helium experiments, given prolonged assistance with the FTIR, provided me with samples, and helped with terahertz spectroscopy. I am also grateful to our collaborators from Chennupati Jagadish's group at the Australian National University, specifically Nian Jiang, H. Hoe Tan, and Chennupati Jagadish, who we collaborated with for work on III-V nanowires.

Lastly, I thank my parents, sister and her husband, and my family and friends for all they have done for me throughout my life. I further thank my father for his continuing support and encouragement (and also his excellent shuttle service between Oxford and London). Ilija, thank you for all your support and putting up with me over the years. Finally, Evelyn - thank you for always being there for me, understanding and compassionate, loving and caring.

This thesis is dedicated to my mother.

Acknowledgements

In Chapter 4, $CH_3NH_3PbI_3$ samples were grown by Jay Patel. *ab initio* calculations were carried out by Marina R Filip and Carla Verdi from Feliciano Giustino's group from the Department of Materials at the University of Oxford. Timothy W. Crothers carried out numerical self-absorption corrections to previous transient terahertz measurements (Chapter 4) taken by Rebecca L Milot. Adam D Wright conducted temperature-dependent photoluminescence measurements.

In Chapter 5, formamidinium lead triiodide samples were grown by Juliane Borchert.

In Chapter 6, GaAs-AlGaAs quantum well tube nanowires were grown and TEM measurements were taken by Nian Jiang and H. Hoe Tan from Chennupati Jagadish's group from the Electronic Materials Engineering department at the Australian National University and further TEM support was provided by Sonia Conesa-Boj.

List of Publications

- **CL Davies**, P Parkinson, N Jiang, JL Boland, S Conesa-Boj, HH Tan, C Jagadish, LM Herz, MB Johnston, *Low Ensemble Disorder in Quantum Well Tube Nanowires*, Nanoscale, **7**, 20531–20538, (2015)

- **CL Davies**, MR Filip, JB Patel, TW Crothers, C Verdi, AD Wright, RL Milot, F Giustino, MB Johnston, LM Herz, *Bimolecular recombination in methylammonium lead triiodide perovskite is an inverse absorption process*, Nature Communications, **9**, *1*, 293, (2018)

- **CL Davies**, J Borchert, CQ Xia, RL Milot, H Kraus, MB Johnston, LM Herz, *Impact of the Organic Cation on the Optoelectronic Properties of Formamidinium Lead Triiodide*, J. Phys. Chem. Lett., **9**, 4502–4511 (2018)

- **CL Davies**, LM Herz, MB Johnston, *Temperature-Dependent Refractive Index of Quartz at Terahertz Frequencies*, J. Infrared Millim. Terahertz Waves, 1-13, (2018)

- JL Boland, S Conesa-Boj, P Parkinson, G Tütüncüoglu, F Matteini, D Rüffer, A Casadei, F Amaduzzi, F Jabeen, **CL Davies**, HJ Joyce, LM Herz, A i Morral, MB Johnston, *Modulation Doping of GaAs/AlGaAs Core–Shell Nanowires With Effective Defect Passivation and High Electron Mobility*, Nano Letters, **15**, *2*, 1336–1342, (2015)

- JL Boland, A Casadei, G Tütüncüoglu, F Matteini, **CL Davies**, F Jabeen, HJ Joyce, LM Herz, A Fontcuberta I Morral, MB Johnston, *Increased Photocon-*

ductivity Lifetime in GaAs Nanowires by Controlled n-Type and p-Type Doping, ACS Nano, **10**, *4*, 4219–4227, (2016)

- HJ Joyce, JL Boland, **CL Davies**, SA Baig, MB Johnston, *A review of the electrical properties of semiconductor nanowires: insights gained from terahertz conductivity spectroscopy*, Semiconductor Science and Technology, **31**, *10*, 103003, (2016)

- K Peng, P Parkinson, JL Boland, Q Gao, YC Wenas, **CL Davies**, Z Li, L Fu, MB Johnston, HH Tan, C Jagadish, *Broadband Phase-Sensitive Single InP Nanowire Photoconductive Terahertz Detectors*, Nano Letters, **16**, *8*, 4925–4931, (2016)

- J Borchert, RL Milot, JB Patel, **CL Davies**, AD Wright, L Martínez Maestro, HJ Snaith, LM Herz, MB Johnston, *Large-Area, Highly Uniform Evaporated Formamidinium Lead Triiodide Thin Films for Solar Cells*, ACS Energy Letters, **2**, *12*, 2799–2804, (2017)

- HJ Joyce, SA Baig, P Parkinson, **CL Davies**, JL Boland, HH Tan, C Jagadish, LM Herz, MB Johnston, *The influence of surfaces on the transient terahertz conductivity and electron mobility of GaAs nanowires*, Journal of Physics D: Applied Physics, **50**, *22*, 224001, (2017)

- JL Boland, G Tutuncuoglu, JQ Gong, S Conesa-Boj, **CL Davies**, LM Herz, A i Morral, MB Johnston, *Towards higher electron mobility in modulation doped GaAs/AlGaAs core shell nanowires*, Nanoscale, **9**, *23*, 7839–7846, (2017)

- JB Patel, Q Lin, O Zadvorna, **CL Davies**, LM Herz, MB Johnston, *Photocurrent Spectroscopy of Perovskite Solar Cells Over a Wide Temperature Range from 15 to 350 K*, The Journal of Physical Chemistry Letters, **9**, *1*, 263–268, (2018)

Contents

1 Introduction - Metal Halide Perovskites and Semiconductor Nanowires **1**

1.1 Perovskites . . . 3

1.1.1 Background . . . 3

1.1.2 Structure and Growth . . . 3

1.1.3 Devices . . . 5

1.1.4 Challenges and Future . . . 7

1.2 Nanowires . . . 8

1.2.1 Background . . . 8

1.2.2 Growth . . . 8

1.2.3 Surface Passivation . . . 9

1.2.4 Quantum Wells . . . 10

2 Electronic Processes in Inorganic Semiconductors **11**

2.1 Optical Absorption - Elliott Theory . . . 11

2.1.1 Excitonic energy states . . . 11

2.1.2 Optical Absorption by Excitons . . . 14

2.2 Calculating the Radiative Bimolecular Recombination Rate Constant (k_2) from the van-Roosbroeck and Shockley Relation . . . 17

2.2.1 Radiative recombination rate . . . 17

2.2.2 Intrinsic charge-carrier concentration. . . . 18

2.2.3 Bimolecular recombination rate. 20
2.3 Photoluminescence Modelling of a Quantum Well Tube Nanowire . . 20
2.3.1 Density of States 20
2.3.2 Band-to-band Recombination 24
2.3.3 Finite Well Model for the Band Structure 26
2.3.4 Surface-Area to Volume Ratio of Quantum Well Tube Nanowires 28

3 Experimental Techniques 30
3.1 Photoluminescence Spectroscopy 30
3.1.1 Micro-Photoluminescence 30
3.2 Fourier Transform Infrared Spectroscopy 32
3.2.1 What it is used for 32
3.2.2 Michelson interferometer 32
3.2.3 Spectral Range and Measurements 35
3.2.4 FTIR Experimental Setup 36
3.3 Terahertz Spectroscopy 38
3.3.1 Terahertz Time Domain Spectroscopy 38
3.3.2 Terahertz Generation 40
3.3.2.1 Generation by Optical Rectification of Nonlinear Crystals. 40
3.3.2.2 Generation using Spintronic Emitters. 40
3.3.3 Terahertz Detection 41
3.3.3.1 Detection by Electro-Optic sampling 41
3.3.3.2 Signal Recovery. 42
3.3.4 Optical Pump Terahertz Probe Spectroscopy 43
3.4 Analysis of Terahertz Spectroscopy 45
3.4.1 Thin Films 45
3.4.1.1 Dielectric Function 46

3.4.1.2 Photoconductivity 47
3.4.2 Thick films 48
3.4.2.1 Temperature-dependent complex refractive index of z-cut quartz 49
3.4.3 Mobility from Optical Pump Terahertz Probe Spectroscopy . . 54
3.4.4 Photoconductivity of Intra-excitonic Transitions 55

4 Bimolecular Recombination in Methylammonium Lead Triiodide Perovskite 57

4.1 Introduction and Background 57
4.2 Sample Fabrication 60
4.3 Results and Discussion 62
4.3.1 Absorption 62
4.3.2 Theoretical Calculations 69
4.3.3 Recombination 76
4.3.3.1 van-Roosbroeck Shockley Relation 76
4.3.3.2 Considerations of Coulomb Correlation and Mott Densities 78
4.3.3.3 Mott Density 81
4.3.3.4 Bimolecular Recombination 85
4.4 Summary 88

5 Impact of the Organic Cation on the Optoelectronic Properties of Formamidinium Lead Triiodide 90

5.1 Introduction 90
5.2 Experimental Details 94
5.2.1 $FAPbI_3$ thin film fabrication by vapour-deposition 94
5.2.2 Terahertz time-domain spectroscopy (TDS) 94

5.2.3 Optical pump terahertz probe spectroscopy (OPTPS) 95
5.2.4 Fourier transform infrared spectroscopy 95
5.3 Results and discussion 97
5.3.1 Excitonic Transitions 97
5.3.2 Temperature-dependent Absorption Coefficient 108
5.3.3 Charge Carrier Mobility in $FAPbI_3$ 114
5.4 Summary 116

6 Low Disorder GaAs-AlGaAs Quantum Well Tube Nanowires Investigated by Single Nanowire Photoluminescence 118
6.1 Method 120
6.1.1 Growth Method 120
6.1.2 Experimental Details 121
6.2 Results and Discussion 121
6.2.1 Model 121
6.2.2 Single Nanowire Photoluminescence and Statistical Correlations 125
6.2.3 Simulations 129
6.3 Summary 137

7 Conclusion 138
7.1 Outlook 140

Bibliography 142

Chapter 1

Introduction - Metal Halide Perovskites and Semiconductor Nanowires

Since the advent of fire, humans have been on a quest to harness, control and convert energy from one form to another. Fire gave us the means to cook food, which is more readily digested by our bodies than the raw form, and hence increased our energy harvesting efficiency [1]. The next major leap forward in fuelling humans came with the agricultural revolution around 10,000 years ago [2]. Whilst this revolution did not expand the diversity of food available nor increase our capability to consume food, it did increase the density of food available to humans in a given area. This allowed for the exponential increase of the human population [3]. The burden of energy source in early agricultural times fell mainly on animals. Animals were coerced into ploughing fields in preparation for seeds to be sown, converting food into mechanical labour to produce more food for humans, with the cycle being repeated on a seasonal basis.

With the industrial revolution came the commercialisation of the steam engine, a means for converting heat into mechanical work. As the population grew, so did our

dependence on these energy sources. However, the success story of humans has not come without consequences on the environment. The effect that burning fossil fuels has had on the environment is largely accepted worldwide. The Paris Agreement [4, 5] is an acknowledgement of this by world powers and for agreeing nations to transition to using clean energy sources instead of fossil fuels. The finite and diminishing supply of fossil fuels also leads to the economic argument for transitioning away from these non-renewable sources [6].

Renewable energy sources include energy from solar, wind, tides, plants, and geothermal heat, and these provide a promising alternative to the traditional fossil fuels. Of these energy sources, solar has received a great interest globally and is the main motivation for this thesis.

Silicon has been the dominant material in the commercial market used for solar cells although there still remain openings for further improvements. The two main paths being explored currently to improve the photovoltaic (PV) device cost-to-performance efficiency are the processing of cheaper alternative materials, or extending the single junction silicon PV device into tandem devices which could increase the efficiency for negligible overall cost. Metal-halide perovskites are an emerging material with the potential to fill both of these gaps in the market.

Over the last century the field of electronics has emerged and with this came the desire to make technology smaller, denser and more powerful. Born out from this desire were nanowires - nanoscale solid tubes of semiconducting material. The first growth of nanowires was in 1964 by Wagner and Ellis [7] and the fabrication quality has come a tremendous way since then. It is only in the last decade that we are in a position to start to produce nanowires with atomic precision. Nanowires have excellent light funnelling properties [8] making them an interesting avenue to explore for use in optoelectronic and PV devices.

Metal-halide perovskites and nanowires are both examples of novel semiconductors

with the potential to further our light-harvesting capabilities. Realising their potential will rest on understanding their fundamental optoelectronic properties. This thesis, along with the work produced during its making, helps to contribute to our fundamental understanding of the optoelectronic properties of nanowires and metal-halide perovskites.

1.1 Perovskites

1.1.1 Background

Metal-halide perovskites are an emerging class of materials showing high promise to be implemented as the active layer in commercial photovoltaic devices. Perovskite relates to the structure of the material, which is any material with an analogous crystal structure to calcium titanate, and in the following section the wide ranging possibilities of material combinations are discussed. The perovskite structure has been well known for over a century [9], although its use in optoelectronic devices has only occurred relatively recently. The main initial progress for metal-halide perovskites began in the 1990s with work by Mitzi, who demonstrated their use in light emitting diodes and transistors [10, 11, 12]. The use of metal-halide perovskites in photovoltaics was popularised in the early 2010s [9], and the performance of metal-halide perovskite based devices has seen a dramatic increase, with current certified devices achieving over 22% [13].

1.1.2 Structure and Growth

The perovskite structure of a material, commonly written as ABX_3, is any material that shares the same structure as calcium titanate ($CaTiO_3$). Here, the A site refers to an organic cation, such as methylammonium (MA or CH_3NH_3) and formamidinium (FA or $(NH_2)_2CH$), or the element cesium (Cs). The B site is the metal commonly

lead (Pb), although there are efforts to substitute lead for tin (Sn) owing to concerns of the toxicity of Pb. X is the halide site which is typically either bromide (Br) or iodide (I). The prototypical perovskite is $MAPbI_3$ and is the focus of Chapter 4, and the closely related perovskite $FAPbI_3$ is investigated in Chapter 5. A schematic of the structure is given in Figure 1.1. The perovskite structure forms a pseudo-cubic structure with corner-sharing BX_6 (Pb-I) octahedra with an organic cation at the centre (MA or FA).

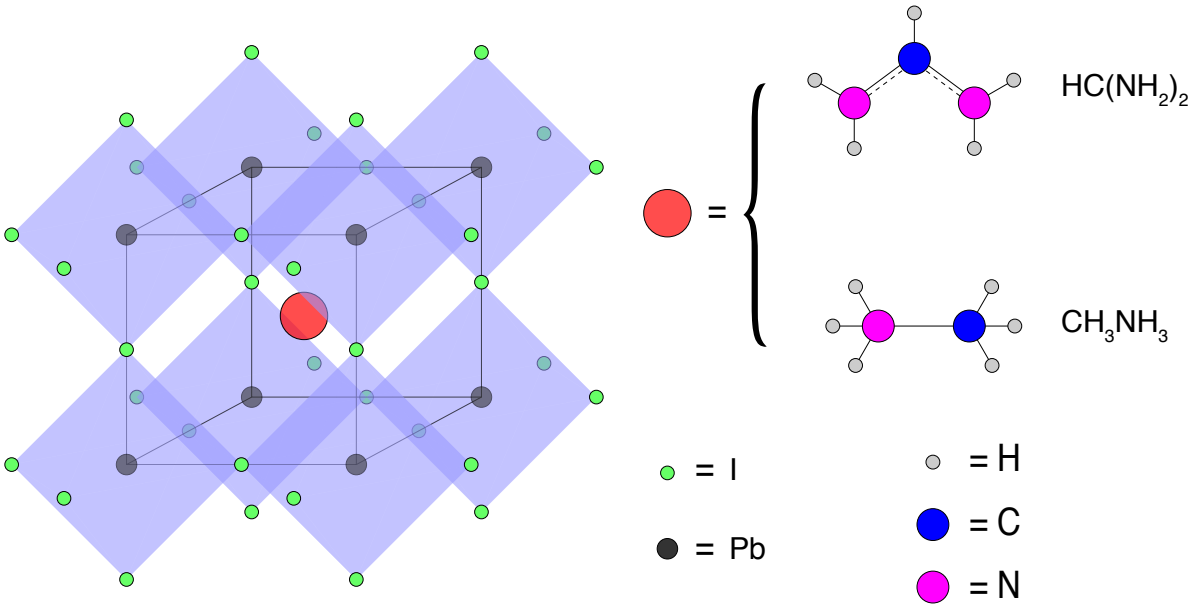


Figure 1.1: Structure of a metal-halide perovskite.

Metal-halide perovskites have a wide range of deposition techniques including spin-coating [14, 15], vapour deposition [16, 17, 18], and ink-jet printing [19]. The samples investigated in this thesis were grown by vapour deposition. Optically smooth polycrystalline thin films ($MAPbI_3$ or $FAPbI_3$) can be fabricated using thermal co-evaporation in a vacuum chamber. Using a dual source evaporation system, MAI (or FAI) and PbI_2 are placed in separate crucibles. Substrates are mounted on a rotating substrate holder to ensure a uniform film is deposited and the temperature of the substrate is held constant during deposition. During evaporation the pressure in the

chamber is typically held at 10^{-6} mbar. The crucibles are individually heated and once the deposition rate has stabilised the substrates are exposed to the vapour for a time of approximately a few hours. The thickness of the film produced is approximately a linear function of the time that the substrate is exposed to the vapour.

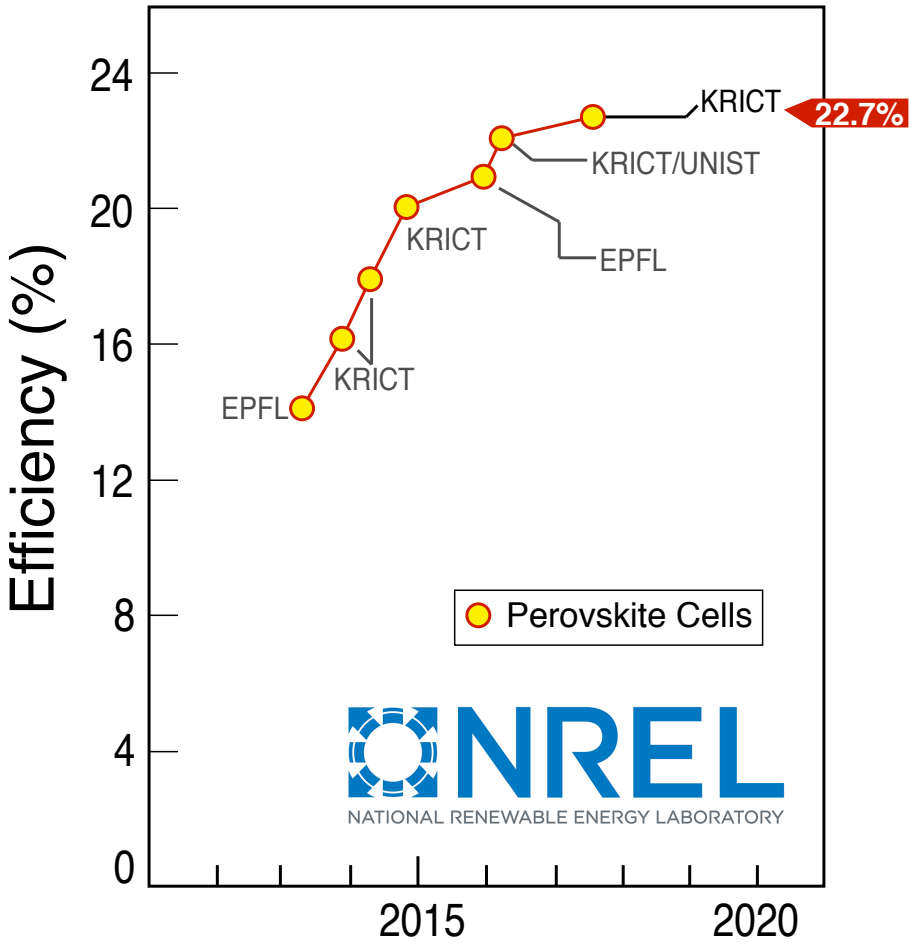


Figure 1.2: Adapted from [13], highlighting the rapid rise in efficiencies of metal-halide perovskite based photovoltaics.

1.1.3 Devices

The meteoric rise in photovoltaic device efficiencies over the last eight years has been a driving force in the research community, with current devices exceeding 22% [13].

Metal-halide perovskite based devices, although not stabilised, have even surpassed multi-crystalline silicon cells (22.3%). However single crystal silicon still has superior performance (25.8%). The perovskite structure is very versatile and can accommodate many different combinations of site substitutions. This versatility leads to metal-halide perovskites being highly tuneable with band-gaps ranging from the infrared to the near-UV region of the spectrum. The band gap of the absorbing layer in a photovoltaic device will determine its fundamental efficiency limit.

Physical processes governing charge-carriers in the absorbing layer of a solar cell device will place limits on the efficiency of the device. Charge-carrier mobility [20, 21], charge-carrier density [22], charge-carrier recombination [23, 24], diffusion length [25], absorption coefficient [26], conduction and valence band alignment with electron and hole transport layers [27] all will have an effect on the device performance. For energy from absorbed light to be harvestable, electrons and holes need to reach the electron and hole transport layers with a reasonably high probability [26]. Therefore the diffusion length, which is proportional to the square root of the charge-carrier mobility divided by the recombination rate, needs to be on the same order of magnitude or preferably less than the thickness of the absorbing layer. This gives us motivation to make the absorbing layer thinner, however, the layer needs to be thick enough such that the layer can absorb a high percentage of incident light. The charge-carrier density will be determined by a payoff between the rate at which light is absorbed (absorption coefficient), the rate of charge-carrier recombination, and the rate of extraction of charge-carriers which is limited by their mobility. The charge-carrier density along with the band gap of the absorbing material determines the splitting of the electron and hole quasi fermi levels whose difference in energy levels is related to the voltage of the device. The charge-carrier recombination dynamics can be split into three main regimes: monomolecular (trap-dominated recombination); bimolecular (band-edge recombination); and Auger recombination (higher order processes

involving more than two particles), and are discussed in Section 4.

Multi-junction tandem devices require precise tuning of the band gap to maximise the efficiency of the device and recently all-perovskite tandem devices have been reported [28, 29]. Tandem perovskite-silicon devices have also been demonstrated using a mixed-cation lead mixed-halide perovskite [30]. Hysteresis in current-voltage curves depending on scanning direction has been a concern, although there has been significant progress on this issue with the origin being attributed to a ion migration and capacitive effects at the interfaces [31, 17].

1.1.4 Challenges and Future

Looking towards the future of metal-halide perovskites, the main challenge that faces the commercialisation of the material is stability and repeatability. There are many different types of stability, or rather instability, including: thermal stability; stability under UV illumination; moisture stability; and heat stability. Overcoming issues of stability will require careful consideration of the different decay channels (decomposition reactions) and whether the initial perovskite material is more energetically favourable than the decay products [32]. Owing to the versatility of material substitutions that metal-halide perovskites allow for there is a large materials parameter space to explore and a lot of research still to be carried out.

1.2 Nanowires

1.2.1 Background

Semiconductor nanowires research has increased rapidly over the past decade owing to improved materials processing, and to their potential use in next generation electronic and optoelectronic devices. Nanowires are typically long prisms with a hexagonal cross-section with diameters ranging between 10 nm and 300 nm and with lengths greater than 1 μm. Their large aspect ratio along with their nanoscale size produces interesting physics not observed in the bulk, such as both cubic zincblende and hexagonal wurtzite phases are stable in group III-V nanowires whereas only the zincblende phase is stable in the bulk [33]. There are already many nanowire based devices that have been demonstrated, including solar cells [34, 35], terahertz detectors [36, 37, 38], field effect transistors [39, 40], and LED-based devices [41, 42].

1.2.2 Growth

Nanowires are typically grown by one of two methods - molecular beam epitaxy (MBE) or metal-organic chemical vapour deposition (MOCVD). Both MBE and MOCVD are bottom-up growth techniques, historically however, nanowires were grown by lithography and etching, a top-down growth technique. The transition from top-down to bottom-up growth has led to atomically precise growth of nanowires that we have today [43].

In Chapter 6, nanowires grown by MOCVD are investigated. In this paragraph, I outline the method of gold-catalyst assisted MOCVD nanowire growth. Au nanoparticles are distributed onto the substrate surface. The diameter of these particles is of approximately the same size as the diameter of the nanowires to be grown. III-V metal-organic precursors in the vapour phase enter the reaction chamber (800 °C). Trimethylgallium (TMGa), trimethylaluminium (TMAl), and arsine (AsH_3) can be

used as sources of Ga, Al, and As elements, respectively. At 800 °C, the Au catalyst is in the liquid phase, and the reactants can be absorbed into the nanoparticle. Nucleation and growth occurs between the substrate and the nanoparticle when the nanoparticle becomes supersaturated. A constant supply of precursors results in the vertical growth of a nanowire.

As well as the nanowire growing vertically (axial direction), we can alter the parameters of the reaction chamber (temperature, pressure, precursors and precursor rates) such that growth can occur in the radial direction [44]. By alternating between different precursors in the growth process, we can achieve growth of core-multishell nanowires.

1.2.3 Surface Passivation

Nanowires have a large aspect ratio and a large surface area-to-volume ratio. Hence, the physical properties at the surface will play a significant role in determining the optoelectronic properties of the nanowires. Trap states at the surface result in high surface recombination velocities and decrease the lifetime of photoexcited charge carriers in comparison with bulk [45]. The photoluminescence of bare GaAs nanowires, grown without shell layers, has been shown to be significantly quenched at room temperature in comparison with low temperature measurements as a result of these states [46]. InP nanowires in comparison with bare GaAs nanowires have a significantly increased charge carrier lifetime as a result of an ultra-low surface recombination velocity [47]. However, this does not resolve the fast surface recombination issue for GaAs nanowires. The issue of a large surface recombination velocity in GaAs nanowires was solved by growing shell layers of AlGaAs and GaAs [48]. AlGaAs has a larger band gap and produces a type I heterojunction with GaAs. This creates a barrier layer between the charge carriers GaAs and the surface of the nanowire - the charge carriers are confined to the core. To prevent oxidation of the aluminium a thin GaAs

cap layer can be grown.

1.2.4 Quantum Wells

The growth of radial heterostructures by varying the precursor gases allows for thin layers to be grown creating quantum well structures in the radial direction [49]. Here we briefly outline the growth of a GaAs-AlGaAs core-multishell nanowire. Typically, the nanowire core (GaAs) is grown vertically, then the reaction chamber parameters are changed to promote radial growth. A radial barrier layer (AlGaAs) of a larger band gap is grown, followed by growth of a thin quantum well tube layer (QWT - GaAs) and another barrier layer (AlGaAs). Finally, a capping layer (GaAs) to prevent oxidation of the nanowire is grown. Nanowires have also been fabricated with multiple quantum well tube layers by successively growing barrier and QWT layers repeatedly [50]. The quantum confined layers allow for tunability of the effective band gap (band gap + confinement energy) which is important for optoelectronic device applications such as lasers [51]. These types of quantum well tube nanowires are the subject of investigation in Chapter 6.

Chapter 2

Electronic Processes in Inorganic Semiconductors

2.1 Optical Absorption - Elliott Theory

2.1.1 Excitonic energy states

Elliott's theory of the intensity of optical absorption [52] by excitons is built upon the simple case of a system with two parabolic and isotropic bands (one conduction and one valence bands) in three-dimensional space with effective masses m_{e} and m_{h}. The dispersion relation of electrons in the conduction band is given by

$$E_{\mathrm{e}}(\mathbf{k}_{\mathrm{e}}) = E_{\mathrm{G}} + \frac{\hbar^2 k_{\mathrm{e}}^2}{2m_{\mathrm{e}}}, \tag{2.1}$$

and the dispersion relation of holes in the valence band is given by:

$$E_{\mathrm{h}}(\mathbf{k}_{\mathrm{h}}) = \frac{\hbar^2 k_{\mathrm{h}}^2}{2m_{\mathrm{h}}}. \tag{2.2}$$

Yu and Cardona [53] detailed that by writing the exciton wavefunction in terms of Wannier functions (Fourier transformed Bloch functions) and changing the coordinate system to a centre of mass coordinate $\mathbf{R}$ and a relative coordinate $\mathbf{r}$ the Schrödinger equation may be decoupled into two seperate equations,

$$-\frac{\hbar^2}{2M}\boldsymbol{\nabla}^2_{\mathbf{R}}\psi(\mathbf{R}) = E_R\psi(\mathbf{R}), \tag{2.3}$$

and

$$\left(-\frac{\hbar^2}{2\mu}\boldsymbol{\nabla}^2_{\mathbf{r}} - \frac{e^2}{4\pi\epsilon_0\epsilon_r r}\right)\psi(\mathbf{r}) = E_r\psi(\mathbf{r}), \tag{2.4}$$

with coordinates defined by,

$$\mathbf{R} = \frac{m_{\mathrm{e}}\mathbf{R}_{\mathrm{e}} + m_{\mathrm{h}}\mathbf{R}_{\mathrm{h}}}{m_{\mathrm{e}} + m_{\mathrm{h}}}, \tag{2.5}$$

and

$$\mathbf{r} = \mathbf{R}_{\mathrm{e}} - \mathbf{R}_{\mathrm{h}}. \tag{2.6}$$

The first equation describes the motion of a free particle of mass $M = m_{\mathrm{e}} + m_{\mathrm{h}}$ with wavevector $\mathbf{K} = \mathbf{k}_{\mathrm{e}} + \mathbf{k}_{\mathrm{h}}$. The eigen-energies of this wave equation are given by

$$E_R = \frac{\hbar^2 K^2}{2M}. \tag{2.7}$$

The second equation is analogous to the hydrogen atom but now with a reduced mass $\mu = (1/m_{\mathrm{e}} + 1/m_{\mathrm{h}})^{-1}$ and modified by the relative permittivity ϵ_r. Just like the case of the hydrogen atom, the exciton has bound states, now with energies given by

$$E_r = E_{\mathrm{G}} - \frac{E_{\mathrm{X}}}{n^2}, \tag{2.8}$$

where n is an integer and E_{G} is the energy of the state as n tends to infinity (the band gap) and E_{X} is the binding energy of the exciton. The allowed energy levels of

an exciton is then simply the sum of E_R and E_r and describes the dispersion relation of the exciton,

$$E_n = E_G + \frac{\hbar^2 K^2}{2M} - \frac{E_X}{n^2}. \tag{2.9}$$

Owing to the Coulombic force between the electron and hole, the dispersion relation of the coupled system can not accurately be represented in the common individual particle picture with conduction and valence bands. One must consider the dispersion of the exciton as a whole system. A schematic of this relations is shown in Figure 2.1

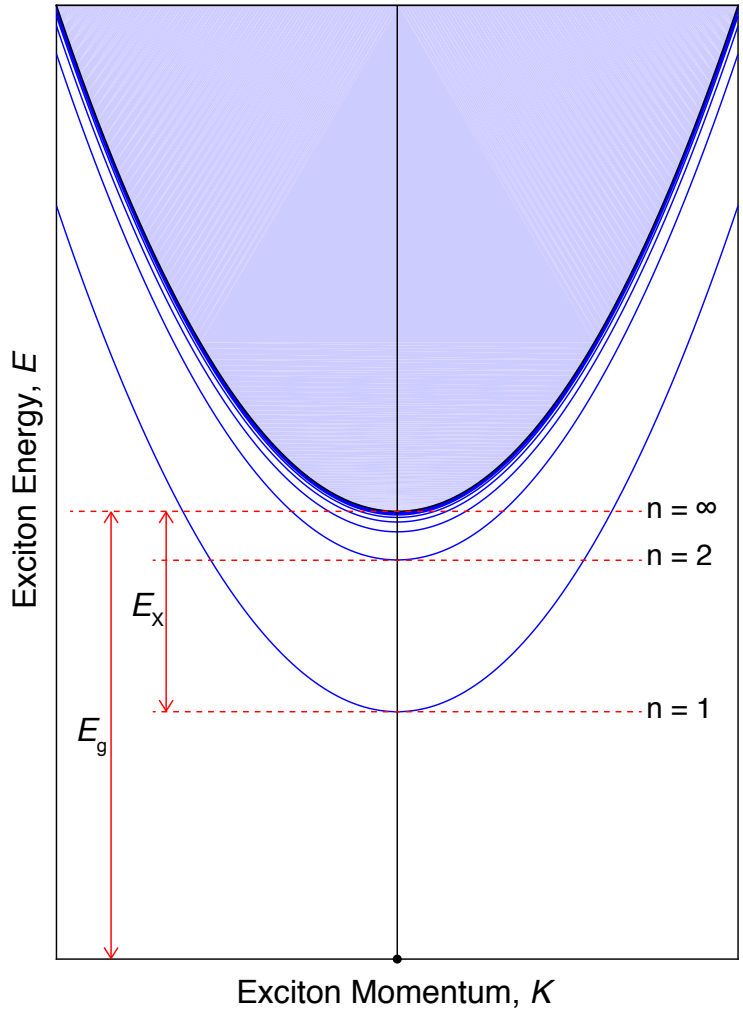


Figure 2.1: Dispersion relation of an exciton.

2.1.2 Optical Absorption by Excitons

Absorption in a direct semiconductor takes place when an electron in the valence band is photoexcited and generates a Coulomb correlated electron-hole pair. The crystal momentum of the pair must be conserved. The momentum of a photon is negligible when compared with the energy-momentum dispersion of an exciton, and an electron-hole pair in the ground state has zero momentum. Hence the photoexcited pair must have a total momentum of zero. The energy states of an exciton in a direct semiconductor are therefore,

$$E_n = E_{\mathrm{G}} - \frac{E_{\mathrm{X}}}{n^2}. \tag{2.10}$$

These energy states describe the bound states of the exciton. It is also possible to excite above the band gap E_g into the continuum where all energies are allowed. The wavefunctions of the bound and unbound states are distinct and the resulting absorption function of the two are also distinct. The absorption by excitons can be found by using Fermi's Golden Rule with the eigenfunctions of the exciton with consideration of momentum conservation [52, 53].

The absorption model, $\alpha(E)$, can be written as a linear combination of the absorption from bound excitons, $\alpha_{\mathrm{X}}(E)$, and electron-hole continuum states, α_{C}, and for a direct semiconductor is written as,

$$\alpha(E) = \alpha_{\mathrm{X}}(E) + \alpha_{\mathrm{C}}(E), \tag{2.11}$$

with,

$$\alpha(E) = b_0 \frac{|\langle \Psi_c | P | \Psi_v \rangle|^2}{E} \left(\sum_{n=1}^{\infty} \frac{4\pi E_{\mathrm{X}}^{3/2}}{n^3} \delta\left(E - \left(E_{\mathrm{G}} - \frac{E_{\mathrm{X}}}{n^2} \right) \right) + \frac{2\pi \sqrt{\frac{E_{\mathrm{X}}}{E - E_{\mathrm{G}}}}}{1 - \exp\left(-2\pi \sqrt{\frac{E_{\mathrm{X}}}{E - E_{\mathrm{G}}}} \right)} c_0^{-1} \mathrm{JDoS}(E) \right), \tag{2.12}$$

where b_0 is a proportionality constant, $\delta(x)$ is the Dirac delta function, c_0 is the Joint density of states constant and $\mathrm{JDoS}(E)$ is the joint density of states (JDoS) is given by

$$\mathrm{JDoS}(E) = \begin{cases} c_0 \sqrt{E - E_{\mathrm{G}}}, & \text{for } E > E_{\mathrm{G}} \\ 0, & \text{otherwise} \end{cases} \tag{2.13}$$

where

$$c_0 = \frac{1}{(2\pi)^2} \left(\frac{2\mu}{\hbar^2} \right)^{3/2} \times 2 \ . \tag{2.14}$$

The first term in brackets in Equation 2.12 is the contribution from bound excitonic states and has the form of a line series at energies $-E_{\mathrm{X}}/n^2$ below the band gap (E_{G}) where n is a positive integer and the magnitude is proportional to $1/n^3$. A pseudo-continuum is produced as n tends to infinity, which is continuous with the absorption of continuum states at the band gap. The absorption associated with continuum states deviates from the expected square-root form for direct-gap semiconductors. Even though electrons and holes in the continuum are unbound, the Coulombic attraction enhances the absorption coefficient of these states. The Coulombic enhancement factor, ξ (equivalent to Equation 3.11 in the original article

by Elliott [52] and appearing in Equation 2.12) is given by

$$\xi = \frac{2\pi\sqrt{\frac{E_{\mathrm{X}}}{E-E_{\mathrm{G}}}}}{1-\exp\left(-2\pi\sqrt{\frac{E_{\mathrm{X}}}{E-E_{\mathrm{G}}}}\right)}. \tag{2.15}$$

It represents the probability of an electron and a hole existing in the same space and is proportional to the overlap of the electron and hole wavefunctions [53]. However, we also need to be in a position to evaluate the absorption coefficient in a system where the Coulombic attraction is not felt between electrons and holes. Physically, this can occur when the attraction is screened owing to a high background charge-carrier density in the system (i.e. above the Mott transition, as discussed further below). Turning off the Coulombic attraction is exactly equivalent to evaluating the limit of the absorption coefficient as the exciton binding energy tends towards zero, since

$$\lim_{E_{\mathrm{X}}\to 0}\xi = 1. \tag{2.16}$$

Taking this limit for Equation 2.12 defines the absorption coefficient $\alpha_{\mathrm{Free}}(E)$ as the value expected when Coulomb interactions are fully screened

$$\alpha_{\mathrm{Free}}(E) \equiv \lim_{E_{\mathrm{X}}\to 0}\alpha(E) = \lim_{E_{\mathrm{X}}\to 0}\alpha_{\mathrm{C}}(E). \tag{2.17}$$

Hence, we obtain from Equation 2.12

$$\alpha_{\mathrm{C}}(E) = \xi(E)\alpha_{\mathrm{Free}}(E), \tag{2.18}$$

with

$$\alpha_{\mathrm{Free}}(E) = b_0\frac{|\left\langle\Psi_c\right| P \left|\Psi_v\right\rangle|^2}{E}c_0^{-1}\mathrm{JDoS}(E-E_{\mathrm{G}}). \tag{2.19}$$

Therefore, in summary, we may write our expression for the total absorption coeffi-

cient α as the sum of bound excitonic (below-gap) absorption and the free (screened) electron-hole absorption multiplied by the Coulombic enhancement factor

$$\boxed{\alpha(E) = \alpha_{\mathrm{X}}(E) + \xi(E)\,\alpha_{\mathrm{Free}}(E)\,.} \tag{2.20}$$

2.2 Calculating the Radiative Bimolecular Recombination Rate Constant (k_2) from the van-Roosbroeck and Shockley Relation

2.2.1 Radiative recombination rate

In 1954 van Roosbroeck and Shockley [54] presented a theory by which the absorption spectrum of a material can be related to the radiative recombination rate. The relation is based on the principle of detailed balance; the radiative recombination rate (R_{Rad}) at thermal equilibrium for an infinitesimal energy interval dE at energy E is equal to the generation rate of electron-hole pairs by thermal radiation at that energy. This rate is $P(E,T)\rho(E,T)$ per unit volume and energy interval, where $\rho(E,T)d(E)$ is the density of photons in the material in the interval dE, and $P(E,T)$ is the probability per unit time that a photon of energy E is absorbed. The total radiative recombination rate per unit volume may be written as the integral over E,

$$R_{\mathrm{rad}}(T) = \int_0^\infty \rho(E,T)\,P(E,T)\,dE\ . \tag{2.21}$$

Equation 14 of van Roosbroeck and Shockley's article [54] gives $P(E)\rho(E)$ in terms of frequency ν and absorption index κ,

$$P(\nu)\rho(\nu)d\nu = \frac{32\pi^2\kappa n^3}{c^3}\nu^3\frac{1}{\exp(h\nu/k_{\mathrm{B}}T)-1}d\nu. \tag{2.22}$$

Replacing the expression for the absorption index κ with the absorption coefficient $\alpha = 4\pi n_{\mathrm{r}}\kappa\nu/c$ where n_{r} is the refractive index and c is the speed of light, and using a change of variables $h\nu = E$ gives

$$P(E)\rho(E)dE = \frac{\alpha}{\hbar^3}\left(\frac{n_{\mathrm{r}}E}{\pi c}\right)^2 \frac{1}{e^{\beta E}-1}dE \ , \tag{2.23}$$

where β is the reciprocal of the thermodynamic temperature. We make the approximation [55] that the refractive index in the medium is constant relative to large variations in the photon distribution ρ with temperature; with $n_{\mathrm{r}} = 2.4$ for the case of $CH_3NH_3PbI_3$ [56]. We consider this assumption to be reasonable since the refractive index is directly linked with absorption through the Kramers-Kronig relations [53]. While the magnitude of the absorption coefficient may theoretically vary with temperature, such changes are very minor for $CH_3NH_3PbI_3$ near the band edge (see Figure 4.2b) suggesting that changes in refractive index are similarly negligible.

Since $e^{\beta E} \gg 1$ near the band gap, the Bose-Einstein distribution term in Equation 2.23 can be written as $e^{-\beta E}$. Using this approximation we obtain the following expression for the total radiative recombination rate per unit volume,

$$R_{\mathrm{rad}}(T) = \int_0^\infty \frac{\alpha(E,T)}{\hbar^3}\left(\frac{n_{\mathrm{r}}\,E}{\pi c}\right)^2 e^{-\beta E}dE \ . \tag{2.24}$$

2.2.2 Intrinsic charge-carrier concentration.

The electron density n_0 in the conduction band is given by

$$n_0 = \int_{E_{\mathrm{C}}}^\infty \text{Electronic density of states} \times \text{Fermi-Dirac distribution}\ dE, \tag{2.25}$$

$$n_0 = \int_{E_{\mathrm{C}}}^\infty \frac{2}{(2\pi)^2}\left(\frac{2m_{\mathrm{e}}^*}{\hbar^2}\right)^{3/2}\sqrt{E-E_{\mathrm{C}}} \times \frac{1}{1+e^{(E-E_{\mathrm{F}})\beta}}dE, \tag{2.26}$$

where m_e^* is the effective mass for the electrons, E_C is the conduction band energy level and E_F is the Fermi energy level. For an intrinsic semiconductor, the Fermi energy level is near the middle of the band gap and hence far away from both the conduction and valence bands and so the Fermi-Dirac distribution may be approximated by the Boltzmann distributions. Hence we can write

$$n_0 = \int_{E_C}^{\infty} \frac{2}{(2\pi)^2} \left(\frac{2m_e^*}{\hbar^2}\right)^{3/2} \sqrt{E - E_C} \times e^{-(E-E_F)\beta} dE, \tag{2.27}$$

which is equivalent to

$$n_0 = \frac{2}{(2\pi)^2} \left(\frac{2m_e^*}{\hbar^2}\right)^{3/2} e^{-(E_C-E_F)\beta} \int_{E_C}^{\infty} \sqrt{E - E_C} e^{-(E-E_C)\beta} dE. \tag{2.28}$$

Using a change of variables ($x = (E - E_C)\beta$; $dx = \beta dE$),

$$n_0 = \frac{2}{(2\pi)^2} \left(\frac{2m_e^*}{\hbar^2}\right)^{3/2} e^{-(E_C-E_F)\beta} \beta^{-3/2} \int_0^{\infty} \sqrt{x} e^{-x} dE. \tag{2.29}$$

The integral evaluates to $\sqrt{\pi}/2$, and so the density of electrons in the conduction band is

$$n_0 = 2 \left(\frac{m_e^* k_B T}{2\pi\hbar^2}\right)^{3/2} e^{-(E_C-E_F)\beta}, \tag{2.30}$$

where T is the temperature and k_B is the Boltzmann constant. Similarly, the density of holes p_0 can be expressed as,

$$p_0 = 2 \left(\frac{m_h^* k_B T}{2\pi\hbar^2}\right)^{3/2} e^{-(E_F-E_V)\beta}, \tag{2.31}$$

where m_h^* is the effective mass for the holes and E_V is the valence band energy level. For an intrinsic semiconductor $n_0 = p_0 = n_i$ where n_i is the intrinsic charge-carrier density. Using $n_0 p_0 = n_i^2$ we can eliminate E_F and obtain an expression for n_i in

terms of m_{e}^*, m_{h}^* and E_{G} (Equation 47 in Varshni's review article [55]),

$$n_{\mathrm{i}} = 2\left(\frac{k_{\mathrm{B}}T}{2\pi\hbar^2}\right)^{3/2}(m_{\mathrm{e}}^* m_{\mathrm{h}}^*)^{3/4} e^{-\frac{1}{2}E_{\mathrm{G}}\beta}. \tag{2.32}$$

2.2.3 Bimolecular recombination rate.

The intrinsic charge-carrier density may be used to convert the radiative recombination rate to the bimolecular recombination constant k_2, according to

$$k_2(T) = \frac{R_{\mathrm{rad}}(T)}{n_{\mathrm{i}}(T)^2}\ . \tag{2.33}$$

2.3 Photoluminescence Modelling of a Quantum Well Tube Nanowire

2.3.1 Density of States

The density of states describes the number of states available in a system per unit energy. This function is needed when considering the energy distribution of charge carriers in a semiconductor and has a direct relation to the emission spectrum of the material, as discussed in 2.3.2. Consider an N–dimensional (N-D) box of side L (Volume= L^N). A particle inside this box experiences a potential V given by

$$V(x_i) = 0 \text{ for } 0 < x_i < L\ , \tag{2.34}$$

$$V(x_i) = \infty \text{ for } x_i < 0 \text{ or } L < x_i\ , \tag{2.35}$$

where x_i are the orthogonal coordinates of the system, for example for a 3–dimensional system $x_i = x, y$ or z. In position representation the time–independent Schrödinger

equation for a non-relativistic particle for the i^{th} coordinate is given by

$$-\frac{\hbar^2}{2m}\frac{\partial^2\Psi(\mathbf{x})}{\partial x_i^2} + V(\mathbf{x})\Psi(\mathbf{x}) = E\Psi(\mathbf{x}) \ . \tag{2.36}$$

Equation (2.35) requires $\Psi(\mathbf{x}) \to 0$ at $x_i = 0$ and $x_i = L$. For $0 < x_i < L$ we have that

$$\frac{\partial^2\Psi(\mathbf{x})}{\partial x_i^2} = -\frac{2mE}{\hbar^2}\Psi(\mathbf{x}) \ , \tag{2.37}$$

let us write

$$\Psi(\mathbf{x}) = \prod_{i=1}^{N}\psi(x_i) \ , \tag{2.38}$$

equation (2.37) then reduces to

$$\frac{\partial^2\psi(x_i)}{\partial x_i^2} = -\frac{2mE}{\hbar^2}\psi(x_i) \ . \tag{2.39}$$

By considering the boundary equations (2.34 and 2.35) the normalised wave function for the i^{th} component must be given by

$$\psi(x_i) = \frac{1}{L^{\frac{1}{2}}}\sin(k_i x_i) \ , \tag{2.40}$$

with $k_i = n_i\pi/L$, and so the overall wave–function is given by

$$\psi(x) = \frac{1}{V^{\frac{1}{2}}}\prod_{i=1}^{N}\sin(k_i x_i) \ . \tag{2.41}$$

The volume occupied by each k-state in k-space is

$$V_k = \left(\frac{\pi}{L}\right)^N \ . \tag{2.42}$$

The number of allowed states with $|\mathbf{k}| \in [k, k+dk]$ is shown in Figure 2.2 and

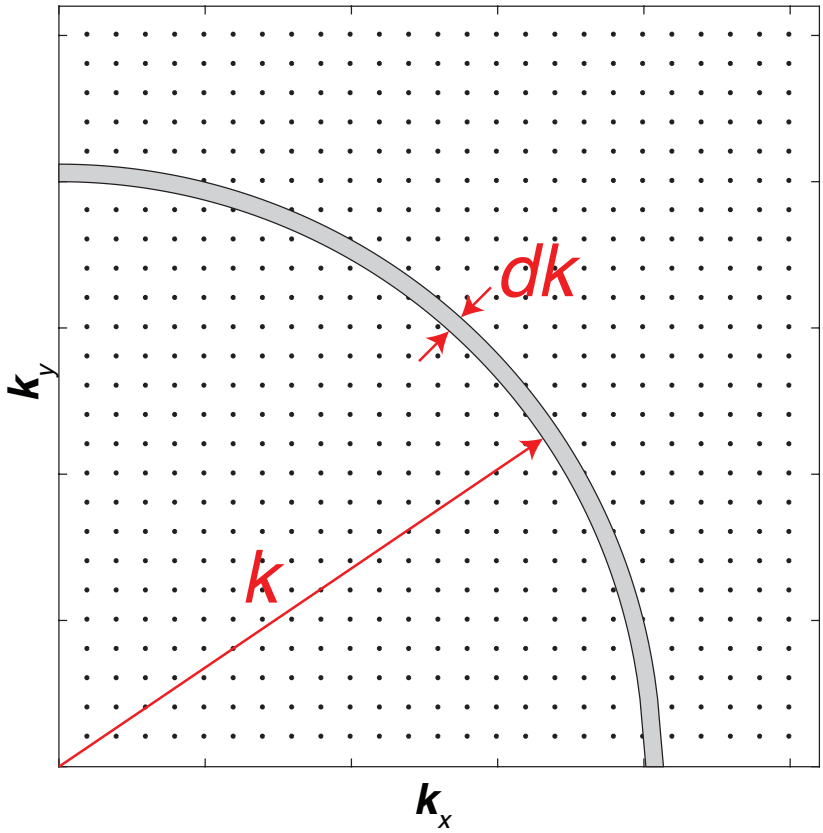


Figure 2.2: Schematic of the allowed k-states in k-space shown as black dots. The density of states function is defined as the number of states in the enclosed volume shown as a shaded grey area.

described by the function $g(k)\mathrm{d}k$ where $g(k)$ is the density of states given by

$$g(k)\mathrm{d}k = \frac{\text{V in k-space of a shell of an } N\text{-D sphere}}{\text{V in k-space occupied per allowed state}} \times \frac{1}{2^N} \times 2 \ , \tag{2.43}$$

where the factor 2 accounts for spin degeneracy, and the factor $1/2^N$ accounts for wavefunctions with $\pm k_i$ being indistinguishable and therefore must only be counted for once. For the case of $N = 3$ and $N = 2$ we have

$$g_{3\mathrm{D}}(k)\mathrm{d}k = \frac{4\pi k^2 \mathrm{d}k}{(2\pi)^3} \times 2 \ , \tag{2.44}$$

$$g_{2\mathrm{D}}(k)\mathrm{d}k = \frac{2\pi k \mathrm{d}k}{(2\pi)^2} \times 2 \ . \tag{2.45}$$

Now rewriting in terms of energy using, $E = \frac{\hbar^2}{2m}k^2$ and $\mathrm{d}E = \frac{\hbar^2}{2m}2k\mathrm{d}k$ we have

$$g_{3\mathrm{D}}(E)\mathrm{d}E = \frac{1}{(2\pi)^2}\left(\frac{2m}{\hbar^2}\right)^{3/2} \ E^{\frac{1}{2}} \ \mathrm{d}E \times 2 \ , \tag{2.46}$$

$$g_{2\mathrm{D}}(E)\mathrm{d}E = \frac{1}{4\pi}\left(\frac{2m^*}{\hbar^2}\right) \ \mathrm{d}E \times 2 \ . \tag{2.47}$$

2.3.2 Band-to-band Recombination

In a semiconducting material, radiative bimolecular recombination occurs between electrons in the conduction band and holes in the valence band. When this takes place a photon of energy E will be emitted. The energy dependence of this emission spectrum is proportional to the Fermi-Dirac distribution multiplied by the joint density of states; a schematic diagram of this is shown in Figure 2.3. For a semiconductor

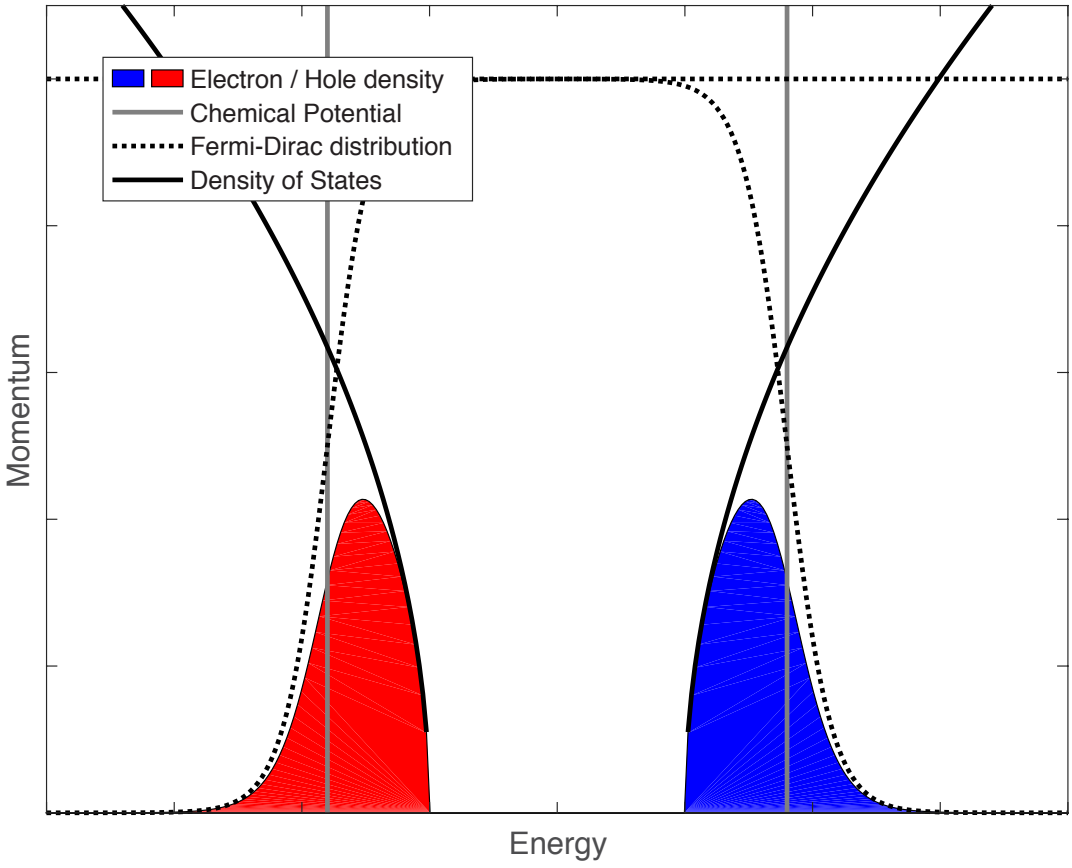


Figure 2.3: Schematic showing the distribution of electrons and holes for a semiconductor in an excited state.

the Fermi-Dirac distribution for electrons in the conduction band and holes in the valence band is given by

$$f_{\mathrm{e,h}} = \frac{1}{\exp((E - E_{\mathrm{f}}^{\mathrm{c,v}})\beta) + 1} \ , \tag{2.48}$$

where $\beta = 1/k_{\mathrm{B}}T$, T is the electron temperature, and $E_{\mathrm{f}}^{\mathrm{c,v}}$ is the Fermi energies of the electrons and holes. In the high temperature limit, the constant $+1$ in the denominator is negligible, and the electron and hole occupancies will follow Boltzmann statistics,

$$f_{\mathrm{e,h}} \propto \exp(-E\beta) \ . \tag{2.49}$$

The rate of emission is proportional to the occupancy of the electrons multiplied by the occupancy of the holes. That is

$$f(E) \propto f_{\mathrm{e}} f_{\mathrm{h}} \propto \exp(-(E_{\mathrm{e}} + E_{\mathrm{h}})\beta) \ , \tag{2.50}$$

$$f(E) \propto \exp(-(E - E_{\mathrm{G}})\beta) \ , \tag{2.51}$$

where E is the energy of the photon emitted on recombination and E_{G} is the band gap of the semiconductor material. Hence, the energy dependence of the emission spectrum in the classical limit is proportional to the Boltzmann distribution, with an energy-offset equal to the band gap energy, multiplied by the joint density of states for the electrons and holes,

$$I(E) \propto g(E) f(E) \ , \tag{2.52}$$

where $f(E)$ is as above and $g(E)$ is the joint density of states for the electrons and holes. The functional form of the density of states will depend on the dimensionality of the structure as discussed in Section 2.3.1.

2.3.3 Finite Well Model for the Band Structure

In Chapter 6 quantum well tube (QWT) nanowires are investigated that consist of a core and multiple shell layers. A schematic of the radial band structure is shown in Figure 2.4. Here, a relation is derived between the width and height of a finite well and the shift in the energy level of the lowest excited state level. This model is used to approximate the band structure of the QWT.

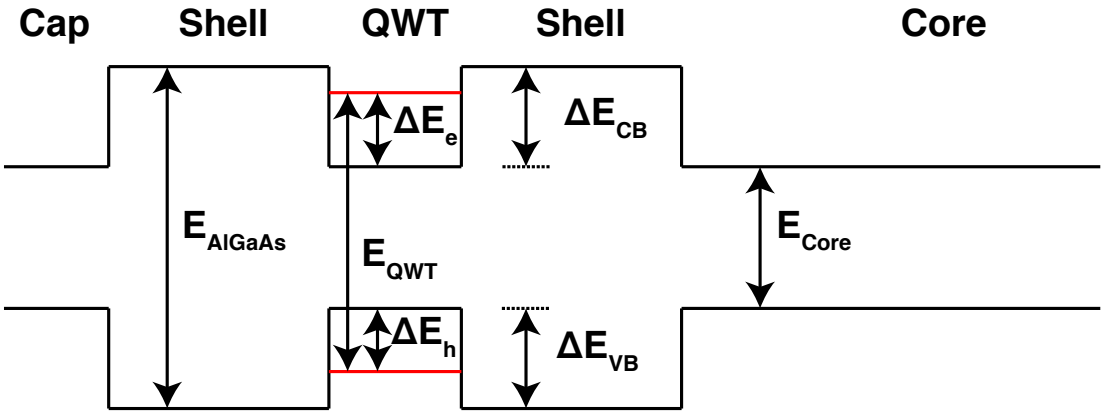


Figure 2.4: A schematic diagram showing the band gap of a GaAs/$Al_{0.4}Ga_{0.6}As$ quantum well. The horizontal red lines represent the energy level of the ground state for a bound particle in the potential well where ΔE_{CB} and ΔE_{VB} are the barrier heights. CB and VB are the conduction and valence band respectively.

The wavefunction of excited electrons and holes in the QWT layer will undergo a perturbation due to quantum confinement effects from the finite potential well created from the difference in band gap between the $Al_{0.4}Ga_{0.6}As$ barrier layers and the GaAs QWT layers. As stated previously this confinement will increase the energy of the ground state transition. The increase in energy due to confinement is needed to be able to deduce the width of the well. Consider a finite well of width d and depth V centred on $x = 0$, and a particle whose effective mass differs in the barrier, m_b^* ($Al_{0.4}Ga_{0.6}As$), and the QWT, m_q^* (GaAs) (b = QWT; q = Core). The wavefunction

of the particle is given by

$$\psi_{\mathrm{q}}(x) = C\exp(\pm kx) \qquad \text{for } |x| < d/2 \ , \tag{2.53}$$

$$\psi_{\mathrm{b}}(x) = C'\exp(\pm \kappa x) \qquad \text{for } |x| > d/2 \ , \tag{2.54}$$

where

$$k = \sqrt{\frac{2m^*_{\mathrm{q}}E}{\hbar^2}} \qquad \text{and} \qquad \kappa = \sqrt{\frac{2m^*_{\mathrm{b}}}{\hbar^2}(V-E)} \ . \tag{2.55}$$

Continuity conditions (ψ and its derivative with respect to x are continuous) restrict the allowed k-states to solutions of

$$\tan\left(\frac{kd}{2}\right) = \frac{m^*_{\mathrm{q}}\kappa}{m^*_{\mathrm{b}}k} \ , \tag{2.56}$$

rearranging this equation to be in terms of energy gives

$$\tan\left(\sqrt{\frac{2m^*_{\mathrm{q}}E}{\hbar^2}}\ \frac{d}{2}\right) = \sqrt{\frac{m^*_{\mathrm{q}}}{m^*_{\mathrm{b}}}\left(\frac{V}{E}-1\right)} \ . \tag{2.57}$$

The model for the quantum well we used is shown in Figure 2.4. The electrons are bound to a potential well of depth ΔE_{CB} and the holes are bound to a well of depth ΔE_{VB}. The values we measure from the photoluminescence are E_{QWT} and E_{Core}. From these values we can deduce the width of the well by solving the following set of simultaneous equations,

$$\Delta E = E_{\mathrm{QWT}} - E_{\mathrm{Core}} = \Delta E_{\mathrm{e}} + \Delta E_{\mathrm{h}} \ , \tag{2.58}$$

$$\tan\left(\sqrt{\frac{2m^*_{\mathrm{q,e}}\Delta E_{\mathrm{e}}}{\hbar^2}}\ \frac{d}{2}\right) = \sqrt{\frac{m^*_{\mathrm{q,e}}}{m^*_{\mathrm{b,e}}}\left(\frac{\Delta E_{\mathrm{CB}}}{\Delta E_{\mathrm{e}}}-1\right)} \ , \tag{2.59}$$

$$\tan\left(\sqrt{\frac{2m^*_{\mathrm{q,h}}\Delta E_{\mathrm{h}}}{\hbar^2}}\ \frac{d}{2}\right) = \sqrt{\frac{m^*_{\mathrm{q,h}}}{m^*_{\mathrm{b,h}}}\left(\frac{\Delta E_{\mathrm{VB}}}{\Delta E_{\mathrm{h}}}-1\right)} \ , \tag{2.60}$$

where the subscripts for the effective mass q and b denote the regions for the QWT layer and the boundary layer respectively, and the subscripts e and h denote the electron and hole respectively. Taking the inverse tangent of the latter two equations and substituting the first equation in, we can solve numerically for E_e and E_h. Substituting these back in and rearranging we can find the width of the well, d given by

$$d = 2\sqrt{\frac{\hbar^2}{2m^*_{\mathrm{q,e}}\Delta E_{\mathrm{e}}}}\arctan\left(\sqrt{\frac{m^*_{\mathrm{q,e}}}{m^*_{\mathrm{b,e}}}\left(\frac{\Delta E_{\mathrm{CB}}}{\Delta E_{\mathrm{e}}}-1\right)}\right) . \tag{2.61}$$

2.3.4 Surface-Area to Volume Ratio of Quantum Well Tube Nanowires

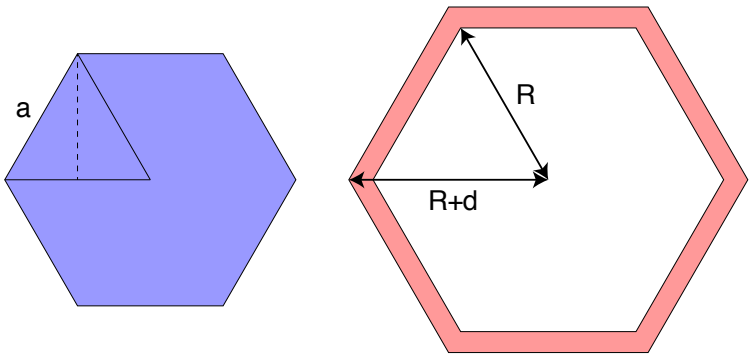


Figure 2.5: Schematic of a hexagonal cross-section of the core (left; blue) and quantum well (right; red) layer of a QWT nanowire. The core is represented by a solid hexagon with side length a. The quantum well layer is represented by a hollow hexagon with inner side length R and outer side length $R + d$.

Later in Chapter 6, the interface between different shell layers in a quantum well tube nanowire is found to have an effect on its optoelectronic properties. The core and multi-shell layers of a QWT nanowire may be approximated by concentric hexagonal prisms. Here we calculate the surface-area to volume ratio of the core, a solid prism with side length a, and the surface-area to volume ratio of the quantum well layer, a hollowed prism with inner radius R and outer radius $R + d$. The surface area and

volume of a prism with side a are given by

$$S = 6l \times a \ , \tag{2.62}$$

$$V = 6l \times a^2 \frac{\sqrt{3}}{4} \ , \tag{2.63}$$

where l is the depth of the prism. Therefore, the surface area to volume ratio of the core is

$$SV_{\text{Core}} = \frac{6l \times a}{6l \times a^2\sqrt{3}/4} = \frac{4\sqrt{3}}{3a} \ , \tag{2.64}$$

and the surface area to volume ratio of the QWT layer is given by

$$SV_{\text{QWT}} = \frac{6l \times (R + (R + d))}{6l \times \frac{\sqrt{3}}{4}((R + d)^2 - R^2)} \ , \tag{2.65}$$

$$SV_{\text{QWT}} = \frac{(2R + d)}{(2Rd + d^2)\frac{\sqrt{3}}{4}} = \frac{4\sqrt{3}}{3d} \ . \tag{2.66}$$

As such, the ratio of the surface area to volume ratio of the QWT and the core is simply a/d.

Chapter 3

Experimental Techniques

3.1 Photoluminescence Spectroscopy

3.1.1 Micro-Photoluminescence

Micro-photoluminescence (μ-PL) spectroscopy is an excellent technique to probe optical properties of a material with micrometer resolution. Owing to the techniques ability to resolve very small objects makes it ideal for investigating the properties of individual nanowires. Local fluctuations during growth of nanowires can lead to differences in the optical properties between individual nanowires. Micro-photoluminescence therefore allows us to gain an insight into the variability of nanowires from a single growth. In Chapter 6, micro-photoluminescence is utilised to investigate quantum well tube nanowires with the experimental setup described here.

Two 50:50 beam splitters were used in the system to observe, excite and collect PL from the nanowires. Incident light was focused onto the sample using a 40× infinity objective with a numerical aperture of 0.65 and the spot size measured to be $1.5 \pm 0.1\,\mu$m. The Abbe diffraction limit of this setup was approximately 400 nm, small enough to observe single nanowires under back illumination due to efficient

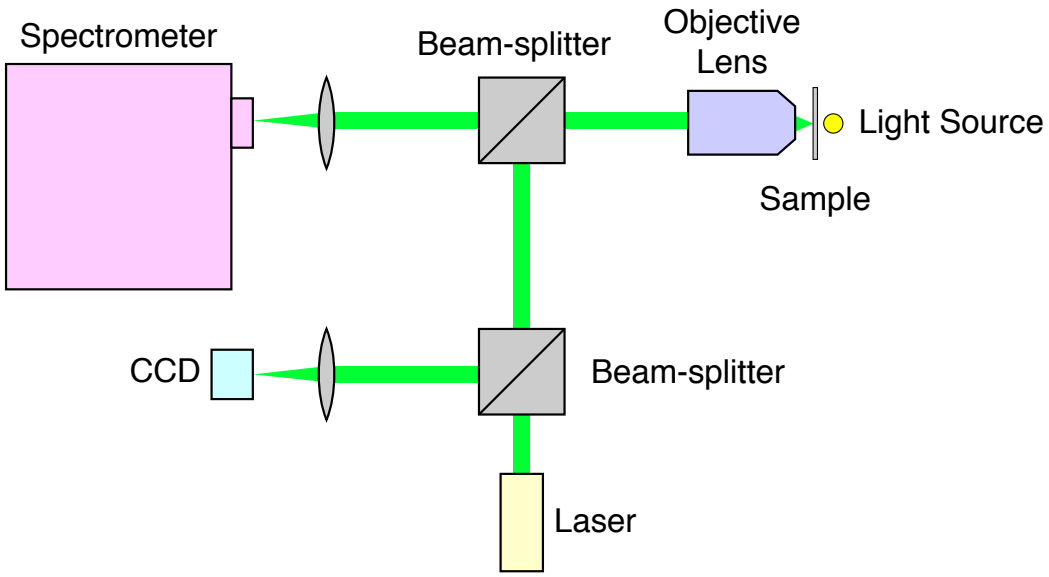


Figure 3.1: Schematic of a micro-photoluminescence spectroscopy setup.

light scattering. Single nanowires were located by back illumination of the sample and observed through the same objective used to focus the laser. A Ti:Sapphire laser combined with a optical parametric oscillator (OPO) was used to excite the sample with 100 fs pulses of 532 nm (2.33 eV) photons at a repetition rate of 80 MHz. The average power used was 3 μW (equivalent to 2.2 μJcm^{-2} per pulse). Excitation power dependent measurements were taken to confirm emitted PL was in the linear regime. The PL was detected using a grating spectrometer and liquid nitrogen cooled charge coupled device (CCD) array. The system was corrected for spectral response. Reflections and scatter of the laser from the sample substrate were blocked using a 575 nm and 590 nm long pass filter.

3.2 Fourier Transform Infrared Spectroscopy

3.2.1 What it is used for

Fourier Transform Infrared (FTIR) spectroscopy is a spectroscopic method predominantly used for measuring the reflection and transmission spectra, and hence absorption spectra of semiconducting materials. The method is highly versatile and offers many advantages over older techniques that use dispersive gratings to measure the properties of materials as a function of wavelength, including faster scanning speeds, higher resolution and a greater spectral range. A modern system can be equipped with readily interchangeable detectors, light sources and beamsplitters allowing for measurements from the far-Infrared continuously through to the ultraviolet part of the spectrum. Semiconductors for photovoltaic applications typically have a band gap in the range from 0.5 to 3 eV for multi-junction cells and an optimal band gap of 1.34 eV for single junction cells. FTIR spectroscopy is therefore an excellent choice for studying the absorption properties near the band gap. The mid to far-Infrared part of the spectrum also allows for phonon modes to be probed.

3.2.2 Michelson interferometer

FTIR spectroscopy utilises a Michelson interferometer that interferes a broadband source with itself creating interference fringes which can later be converted by a Fourier transform to reconstruct the power spectrum of the source as a function of wavenumber. Light is collected from a broadband source and split into two paths using a beam splitter which are then reflect back towards the beam splitter. One path travels a fixed distance L, while the other has a variable path length $(L + \delta)$ by means of a translation stage. Owing to a difference in path length, the two beams interfere with each other once they recombine at the beam splitter. The light is now guided towards a sample where the reflected (transmitted) light is collected by

a detector.

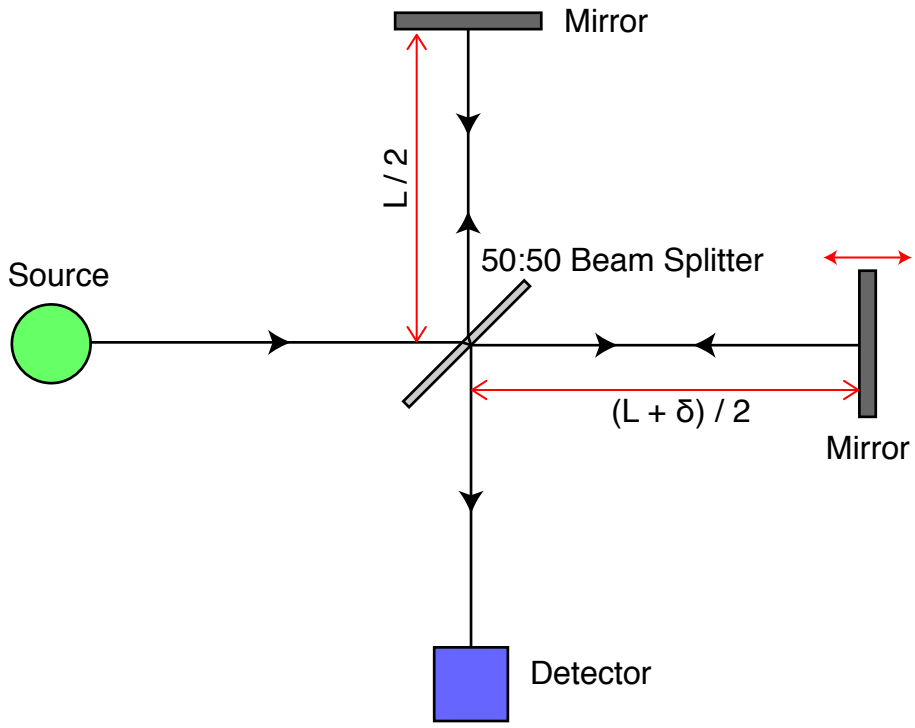


Figure 3.2: Schematic diagram of a Michelson Interferometer.

Consider a monochromatic plane wave that is used as the source for a Michelson Interferometer. The wave may be described in complex form as

$$u = u_0 \exp(i(kz - \omega t)). \tag{3.1}$$

The beam is split in two beams (v and w) by a 50:50 beamsplitter with one beam travelling a distance L and the other $L + \delta$

$$v = \frac{u_0}{2} e^{i(k(L+z)-\omega t)}, \tag{3.2}$$

$$w = \frac{u_0}{2} e^{i(k(L+\delta+z)-\omega t)}. \tag{3.3}$$

The amplitude of the recombined wave is the linear sum of v and w that produces an interfered beam a,

$$\begin{aligned} a &= u_0 \frac{e^{i(k(L+z)-\omega t)} + e^{i(k(L+\delta+z)-\omega t)}}{2}, \\ &= u_0\, e^{i(k(L+z)-\omega t)}\, \frac{1}{2}\,(1 + e^{ik\delta}). \end{aligned} \tag{3.4}$$

The resultant intensity of the interfered beam is given by the modulus squared of w,

$$I(\delta) = |a|^2 = I_0(1 + cos(k\delta)). \tag{3.5}$$

Hence, a Michelson interferometer that uses a monochromatic light source produces a sinusoidally oscillating intensity with path length difference. Now consider a broad-band source with a wavevector dependent intensity profile, $F(k)$. The intensity of interfered light can be described by the integral

$$I(\delta) = \int_0^\infty (1 + cos(k\delta))F(k)dk, \tag{3.6}$$

and rearranging gives

$$I(\delta) = \int_0^\infty F(k)dk + \int_0^\infty \frac{1}{2}(e^{ik\delta} + e^{-ik\delta})F(k)dk. \tag{3.7}$$

$$I(\delta) = I_0 + \frac{1}{2}\int_{-\infty}^\infty F(k)e^{ik\delta}dk \tag{3.8}$$

By rearranging further we can see that the intensity of the exiting beam from the Michelson interferometer can be related to the spectrum of the light source (and rewriting instances of δ with x)

$$f(x) \equiv \frac{I(x) - I_0}{\sqrt{2\pi}} = \frac{1}{\sqrt{2\pi}}\int_{-\infty}^\infty F(k)e^{ikx}dk. \tag{3.9}$$

Here we have a relation from wavevector-space (or wavenumber) to traditional-space by means of a Fourier transform. Utilising the properties of Fourier transforms the inverse direction can also be performed from space to wavevector-space. Hence, we can transform the detected intensity of light as a function path-length difference to a spectrum as a function of wavevector by means of a Fourier transform.

3.2.3 Spectral Range and Measurements

Above we have discussed the basic principles of an interferometer. Here we discuss the practical considerations of measurements consisting of the spectral range of detectors and sources along with reference measurements and reflection-transmission measurements and relating these back to Equation 3.9. Both the emission source intensity ($\phi(k)$) and detector efficiency ($D(k)$) vary as a function of wavevector. The largest spectral range for a pair of sources and detectors will be defined by the range at which the multiple of these two function is above the signal to noise threshold.

Consider now a transmission measurement, $t(x)$ through a sample. We wish to obtain the transmission spectrum of the sample as a function of wavevector, $T(k)$. Our measurement of the sample will allow us to obtain $F(k)$, however $F(k) = \phi(k)\, D(k)\, G_T(k)\, T(k)$, where $G_T(k)$ is a geometrical factor to represent the different optics in the reflection and transmission paths. The desired transmission function of the sample may be decoupled from the other function by means of a reference measurement. The transmission of vacuum is 1 and therefore a measurement of vacuum will give us $F_{\text{vac}} = \phi(k)\, D(k)\, G_T(k)$ and hence we can obtain the transmission spectrum of the sample as a function of wavevector:

$$T(k) = \frac{F(k)}{F_{\text{vac}}(k)} \tag{3.10}$$

The case for reflection is analogous to transmission, except we need to use a reference

mirror with a known reflection spectrum.

3.2.4 FTIR Experimental Setup

For the measurements in this thesis a Fourier transform infrared spectrometer (Bruker Vertex 80v) was used in conjunction with a gas exchange cryostat (Oxford Instruments OptistatCF2) to measure the temperature dependent reflectance (R_s) and transmittance (T_s) spectra. A tungsten halogen lamp source, a calcium fluoride beamsplitter and silicon detector were used. The angle of incident light to the normal of the sample was $\theta = 11°$. Figure 3.3a shows a schematic diagram of the setup used. Figure 3.3b shows the reflection and transmission spectra of a $CH_3NH_3PbI_3$ sample at 4 K. Below the band gap (1.3 to 1.6 eV) the sum of the R_s and T_s of the sample is approximately equal to 1, as expected, since light is not absorbed in this region. However, there are large modulations in R_s and T_s which are Fabry-Perot oscillations. This demonstrates the excellent surface quality of the material and indicates negligible scattering of light at the surface which is important for accurate calculation of the absorption spectrum, in particular near its onset.

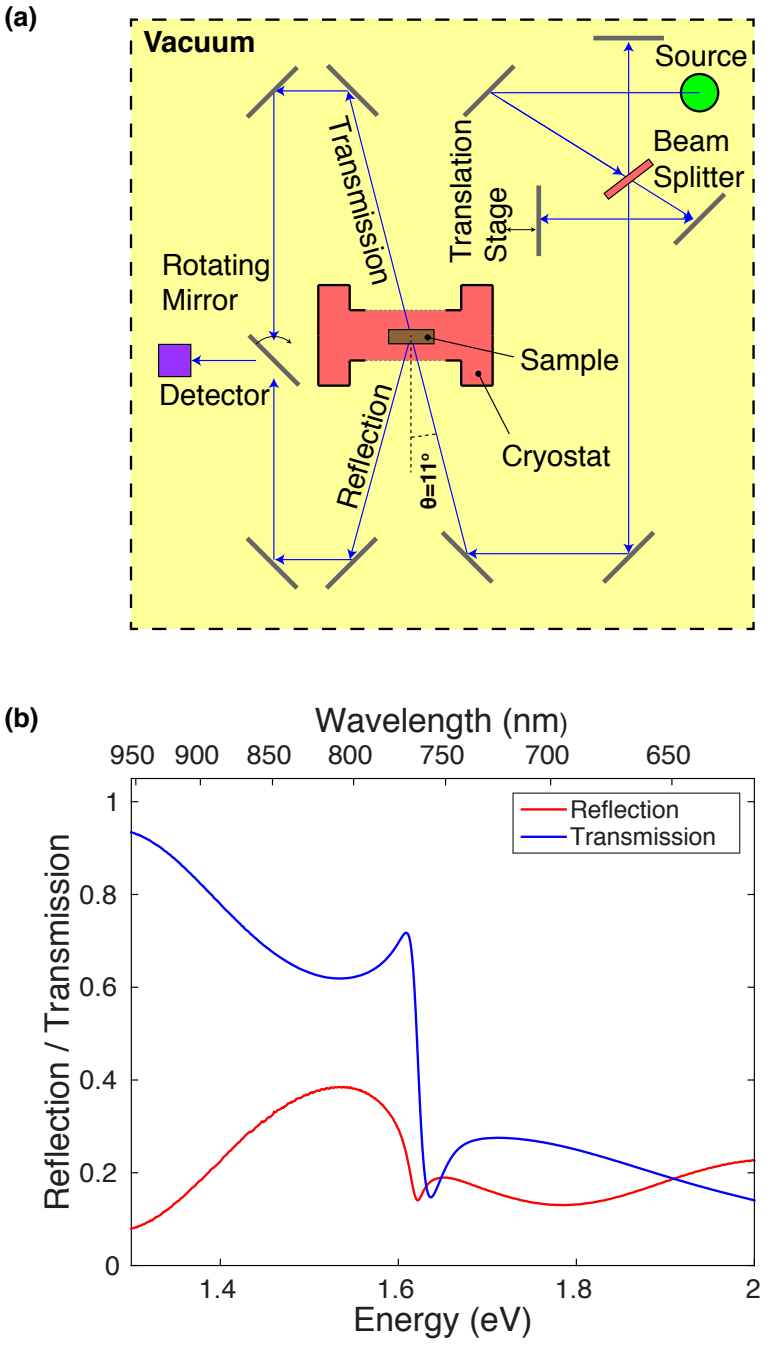


Figure 3.3: Fourier transform infrared spectroscopy. (a) Schematic diagram of the Fourier transform infrared spectrometer with a sample mounted inside a cryostat. (b) Reflection and transmission spectra of $CH_3NH_3PbI_3$ at 4 K.

3.3 Terahertz Spectroscopy

The terahertz region lies between the microwave and infrared part of the electromagnetic spectrum (0.1-30 THz = 3.3-1000 cm^{-1} = 3-0.01 mm = 0.414-124 meV). The generation and detection of terahertz radiation is not possible by conventional electronic and optical devices and requires the use of novel techniques and devices. Terahertz spectroscopy is a non-contact method to probe a wide range of optoelectronic properties of materials on an ultrafast timescale. These optoelectronic properties include: intra-excitonic transitions; phonon modes; plasmon modes; effective masses; charge carrier lifetimes; carrier scattering rates; charge carrier recombination dynamics; charge carrier mobilities; doping densities; and surface recombination velocities. Below discusses the techniques of terahertz time-domain spectroscopy and optical pump terahertz probe spectroscopy, including details on methods for terahertz generation and detection.

3.3.1 Terahertz Time Domain Spectroscopy

Terahertz time-domain spectroscopy (TDS) is a useful method to probe the dielectric function, complex refractive index, and absorption of materials in the terahertz region. For the metal-halide perovskites, phonon modes of the inorganic cage structure, for instance Pb-I for $MAPbI_3$, have energies of a few milli-electron volts and therefore THz-TDS is an ideal method to probe these phonon modes. With TDS (Figure 3.4), the output of an amplified laser system with 30 fs pulses at a repetition rate of 5 kHz with a central wavelength of 800 nm and an average power of 4 W is split into two beam paths: a probe beam; and a gate beam. Terahertz pulses are generated by the methods described below in Section 3.3.2. Terahertz pulses are detected by electro-optic sampling (see Section 3.3.3) using a 0.2 mm thick GaP(110) crystal, Wollaston prism and a pair of balanced photodiodes. Temperature-dependent TDS

measurements of $FAPbI_3$ in Chapter 5 were performed using a cold-finger cryostat (Oxford Instruments). By measuring $FAPbI_3$ on a quartz substrate and reference measurement of a quartz substrate, we can obtain the terahertz transmission in the time domain.

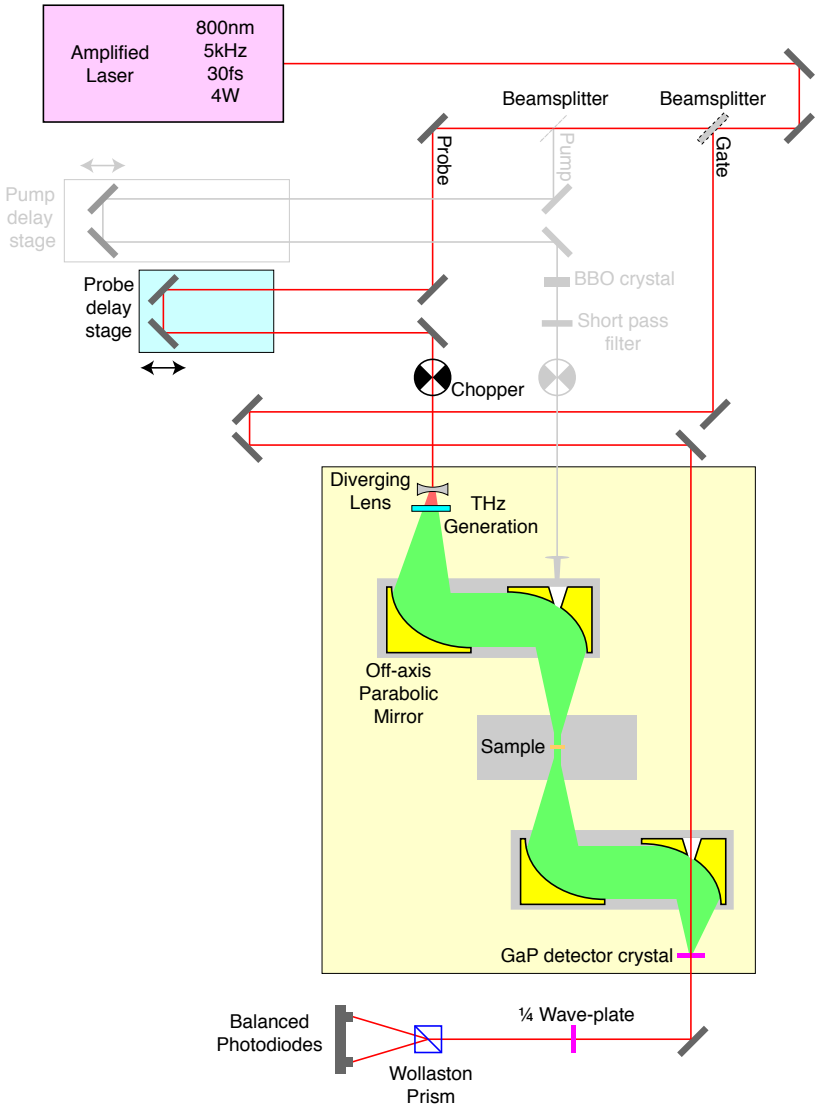


Figure 3.4: Schematic of time-domain terahertz spectroscopy. The section in light grey is for optical pump terahertz probe spectroscopy detailed in Section 3.3.4.

3.3.2 Terahertz Generation

Terahertz spectroscopy is a maturing technique and there currently exist numerous methods for generating terahertz including: optical rectification using nonlinear crystals [57, 58, 59, 60]; spintronic emitters [61, 62]; photoconductive generation [63, 64]; and air plasma generation [65, 66]. In this thesis I have utilised both optical rectification and spintronic emitters to generate terahertz pulses.

3.3.2.1 Generation by Optical Rectification of Nonlinear Crystals.

Generation of terahertz pulses by the method of optical rectification can occur when an ultrafast pulse is incident on a nonlinear crystal. Non-centrosymmetric crystals can give rise to a significant nonlinear susceptibility where in the presence of an external field, E, the polarization is given by $P = P_0 + \epsilon_0(\chi_1 E + \chi_2 E^2 + ...)$. An ultrafast pulse propagating through a crystal with non-zero χ_2 emits a terahertz pulse with an amplitude proportional to the second time derivative of the polarization, and therefore the square of the incident electric field [67, 68, 57, 69]. Consider an ultrafast optical pulse with a temporal Gaussian envelope function with a FWHM of τ equivalent to a standard deviation of $\sigma_\tau = 2\sqrt{2\ln 2}\,\tau$. The terahertz pulse produced by this pulse follows the shape of the second derivative of this Gaussian. For generation of broadband terahertz pulses in the frequency domain, we therefore require as short as possible pulses in the time domain. Two of the most commonly used crystals for terahertz generation by this method are ZnTe [57] and GaP [60]. Each has its own advantage - ZnTe produces pulses with favourable signal-to-noise below $\sim$2 THz however GaP has a larger bandwidth.

3.3.2.2 Generation using Spintronic Emitters.

Recent progress in the field of spintronics has given way to an exciting new class of terahertz emitters with increased broadband emission in comparison to their older

alternatives. Spintronic emitters exploit the inverse spin Hall effect to convert a spin polarised current pulse into a terahertz pulse. The terahertz emitters consist of a ferromagnetic material ($Co_{20}Fe_{60}B_{20}$ – 3 nm) and non-ferromagnetic (Ta, Pt or Ir – 3 nm) metal thin film positioned in an external magnetic field of 10 mT. Terahertz pulses are generated as follows [61, 62]; an ultrafast optical pump (10 fs) excites electrons in the metals above the Fermi energy. Owing to differences in transport properties and lifetimes of spin-up (majority) and spin-down (minority) electrons in the ferromagnetic layer, a strongly spin-polarised current is setup in the z-direction, perpendicular to the plane of the films. When this spin-current transports to the non-ferromagnetic layer, opposing spins are driven in opposite directions (perpendicular to the z-axis, and y-axis of the external magnetic field) by spin-orbit coupling. This produces a charge current along the x-axis which results in the emission of a terahertz pulse. Unlike the generation of terahertz by optical rectification which is a second-order process, the power of emitted terahertz radiation by spintronic emitters scales linearly with pump power.

3.3.3 Terahertz Detection

A variety of techniques also are used for terahertz detection which include: Electro-Optic sampling [70, 58]; photoconductive detection [71, 72]; and air biased coherent detection [73, 74].

3.3.3.1 Detection by Electro-Optic sampling

The detection of terahertz pulses by electro-optic sampling is similar to the inverse of optical rectification. Here, a similar non-linear crystal is utilised with the addition of an ultrafast gate pulse (linearly polarised) which has a duration much shorter than the duration of the terahertz pulse (linearly polarised). The gate pulse will be used to effectively observe brief snapshots of the terahertz pulse, and the entire terahertz

pulse can be measured by varying the delay between the terahertz pulse and the gate pulse. When the terahertz pulse transmits through the nonlinear crystal (non-zero χ_2), the electric field of the terahertz pulse induces a birefringence proportional to the amplitude of the terahertz amplitude. When the gate pulse transmits through the crystal and overlaps in time with a fraction of the terahertz pulse, the polarisation of the gate beam is rotated owing to this induced birefringence. The change in polarisation is detected as follows: the linearly polarised light is converted to elliptically polarised light by a quarter-wave plate; and the horizontal and vertical components are split by a Wollaston prism and detected by a pair of balanced photodiodes. In the absence of a terahertz signal there is no change in polarisation of the gate beam, circularly polarised light exits the quarter-wave plate, and the horizontal and vertical components have equal intensity. In the presence of a terahertz signal the polarisation of the gate beam is rotated by an amount proportional to the amplitude of the signal, elliptically polarised light exits the quarter-wave plate, and the horizontal and vertical components have a difference in intensity proportional to the amplitude of the terahertz signal.

3.3.3.2 Signal Recovery.

The signals produced in terahertz experiments are extremely low in comparison with background noise and so further intricacies are required to recover a signal. Two methods for signal recovery are lock-in amplification and box car integration. For lock-in amplification, the signal is modulated normally by means of a chopper at a given frequency f. For time-domain terahertz spectroscopy the terahertz pulse is chopped before terahertz generation at a frequency f_{THz} and the gate pulse is unchanged. The resulting signal will modulate between a signal with and without terahertz pulses. This modulated signal is then mixed (multiplied) with a reference signal, typically a sine-wave, with the same frequency f_{THz}. By averaging over a time-

period that is much greater than $1/f_{\mathrm{THz}}$ the noise will average out and the signal that remains will be proportional to the terahertz signal. Alternatively, box car integration can measure individual pulses, integrate over a chosen section of a pulse and calculate the difference between alternate pulses when the terahertz is passed and blocked by the chopper. Box-car integration does not need to average over a large time-period, which is a significant advantage for optical pump terahertz probe spectroscopy where a double modulation of the signal is required. For the lock-in method, OPTPS requires a double lock-in measurement and results in a large part of the signal being wasted owing to the averaging procedure. The box-car method however, will utilise every single pulse and is therefore the preferred method.

3.3.4 Optical Pump Terahertz Probe Spectroscopy

Optical pump terahertz probe spectroscopy (OPTPS) was used to measure the photoconductivity of $FAPbI_3$ in Chapter 5. OPTPS extends the TDS method to measure a sample in the photoexcited state. Figure 3.5 shows a schematic of the OPTPS setup. In OPTPS, the sample is photoexcited by an optical pump, and after a short time delay is probed with a terahertz pulse. The generation and detection of the terahertz pulse is the same as in the TDS method detailed above. Transformation from the change in transmission with photoexcitation to photoconductivity is detailed in Section 3.4.1.2. Magneto-photoconductivity measurements were measured by magneto-OPTPS, which is the same as OPTPS but in the presence of a magnetic field (Oxford Instruments Spectromagnet). For magneto-OPTPS, terahertz pulses were generated using optical rectification using a ZnTe crystal and were detected using a ZnTe crystal [75].

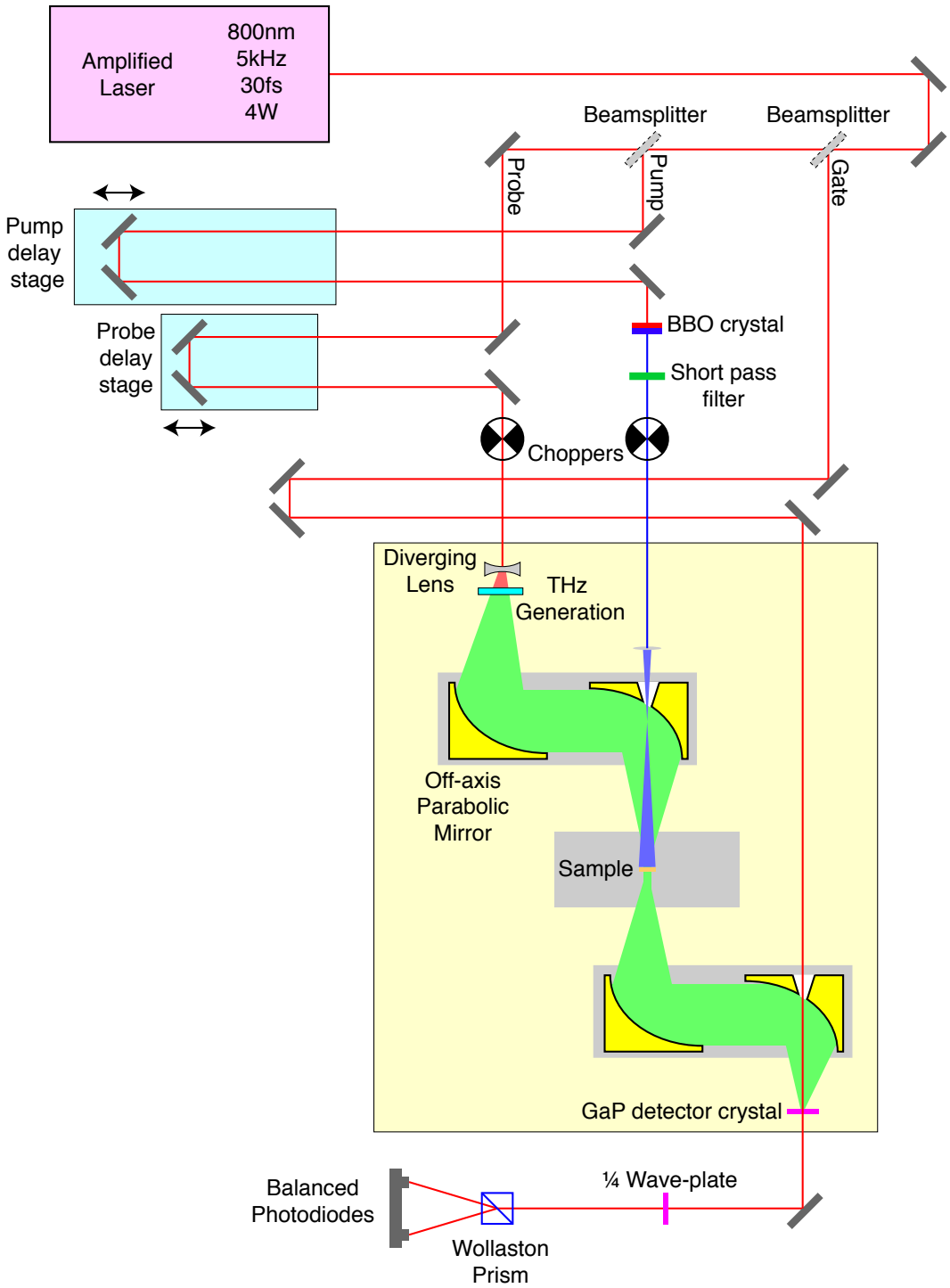


Figure 3.5: Schematic of a optical pump terahertz probe spectroscopy system.

3.4 Analysis of Terahertz Spectroscopy

3.4.1 Thin Films

The physical interest in terahertz measurements lies in the extraction of the dielectric and conductivity properties of a material, and therefore also the complex refractive index. To extract these properties a suitable reference measurement with respect to the sample of interest needs to be considered. As with most nanoscale materials, fabrication of a free standing film is beyond the current methods available and will therefore be grown on a substrate. Figure 3.6 shows the transmission of a terahertz pulse through (**a**) a reference of thickness L, (**b**) a sample of thickness d on a reference substrate, and (**c**) a photoexcited sample on a substrate.

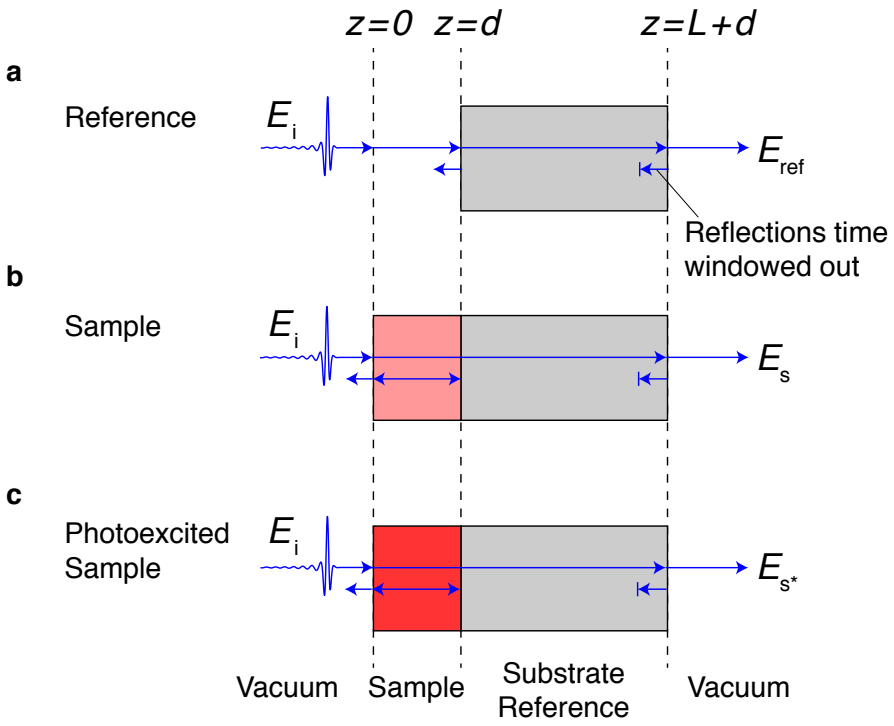


Figure 3.6: Transmission of a terahertz pulse through: **a** a reference; **b** a sample on a substrate; and **c** a photoexcited sample on a substrate. The reference substrate has thickness L and the sample has thickness d.

Consider an incident propagating monochromatic wave, $E_{\mathrm{i}} = E_0 e^{i(kz-\omega t)}$ with a

dispersion relation $k = \tilde{n}\omega/c$ where $\tilde{n}$ is the complex refractive index of a material. The transmitted electric field E for **a**, **b** and **c** in the *frequency* domain is given by

$$E_{\mathrm{ref}} = t_{\mathrm{v,r}}\, t_{\mathrm{r,v}}\, e^{i(\tilde{n}_{\mathrm{v}}d+\tilde{n}_{\mathrm{r}}L)\omega/c} E_{\mathrm{i}} \tag{3.11}$$

$$E_{\mathrm{s}} = t_{\mathrm{v,s}}\, t_{\mathrm{s,r}}\, t_{\mathrm{r,v}}\, \mathrm{FP}_{\mathrm{vsr}} e^{i(\tilde{n}_{\mathrm{s}}d+\tilde{n}_{\mathrm{r}}L)\omega/c} E_{\mathrm{i}} \tag{3.12}$$

$$E_{\mathrm{s}^*} = t_{\mathrm{v,s}^*}\, t_{\mathrm{s}^*,\mathrm{r}}\, t_{\mathrm{r,v}}\, \mathrm{FP}_{\mathrm{vs}^*\mathrm{r}} e^{i(\tilde{n}_{\mathrm{s}^*}d+\tilde{n}_{\mathrm{r}}L)\omega/c} E_{\mathrm{i}}, \tag{3.13}$$

where the subscripts v, r and s denote vacuum, reference and sample, $t_{i,j} = 2\tilde{n}_i/(\tilde{n}_i + \tilde{n}_j)$ is the Fresnel transmission at the boundary between materials i and j. FP_{ijk} is the Fabry-Pérot term that is the contribution from multiple internal reflections in material j situated between i and k, and is defined by

$$\mathrm{FP}_{ijk}(\omega) = \sum_{p=0}^{N} \left(r_{jk} r_{ji} \exp(2i\tilde{n}\omega d/c)\right)^p, \tag{3.14}$$

where $r_{ij} = (\tilde{n}_i - \tilde{n}_j)/(\tilde{n}_i + \tilde{n}_j)$ are the Fresnel reflection coefficients and N is the number of Fabry-Pérot echos.

Our measurements will have an additional unknown frequency dependence owing to the efficiency of the terahertz emitter and detector, however this function of frequency will be constant in time and common to all measurements provided that the laser pulses are consistent over the measurement period. These unknowns can be eliminated by dividing the measurement of interest by a suitable reference.

3.4.1.1 Dielectric Function

The terahertz transmission function, T, of a thin film is defined by

$$T = \frac{E_{\mathrm{s}}}{E_{\mathrm{r}}}. \tag{3.15}$$

For thin film samples ($\omega d/c \ll 1$) the number of Fabry-Pérot echoes can be assumed to tend to infinity ($N \to \infty$) and we can make the approximation $e^{\pm in\omega d/c} = 1 \pm in\omega d/c$. Hence, in the thin film limit and after some rearrangement the terahertz transmission (Equation 3.15) becomes

$$T(\omega) = \left(1 - \frac{i\omega d}{c}\frac{\tilde{n}_\mathrm{r} + \tilde{n}_\mathrm{s}^2}{1 + \tilde{n}_\mathrm{r}}\right)^{-1}. \tag{3.16}$$

For non-magnetic materials, their relative permeability is 1 and hence we can write the dielectric function simply as $\epsilon_\mathrm{s} = \tilde{n}_\mathrm{s}^2$. Using this substitution in Equation 3.16 and rearranging, the dielectric function can be obtained, given by

$$\epsilon_\mathrm{s}(\omega) = \frac{ic(1 + \tilde{n}_\mathrm{r})}{\omega d}\left(\frac{1}{T(\omega)} - 1\right) - \tilde{n}_\mathrm{r}. \tag{3.17}$$

3.4.1.2 Photoconductivity

The change in transmission of a material upon photoexcitation with respect to the transmission of a sample in the dark, $\Delta T/T$, is defined by

$$\frac{\Delta T}{T} = \frac{E_{\mathrm{s}*} - E_\mathrm{s}}{E_\mathrm{s}} = \frac{E_{\mathrm{s}*}}{E_\mathrm{s}} - 1. \tag{3.18}$$

Taking the thin film limit, ($\omega d/c \ll 1$) as discussed above, leads to

$$\frac{\Delta T(\omega)}{T(\omega)} = \frac{i\omega d}{c}\frac{\tilde{n}_{\mathrm{s}*}^2 - \tilde{n}_\mathrm{s}^2}{1 + \tilde{n}_\mathrm{r}}. \tag{3.19}$$

The squared complex refractive indices may be written in terms of the photoconductivity $\Delta\sigma = (-i\epsilon_0\omega/c)(\tilde{n}_{\mathrm{s}*}^2 - \tilde{n}_\mathrm{s}^2)$. Making this substitution and rearranging gives the photoconductivity

$$\Delta\sigma(\omega) = -\frac{\epsilon_0 c(1 + \tilde{n}_r)}{d}\frac{\Delta T}{T}. \tag{3.20}$$

3.4.2 Thick films

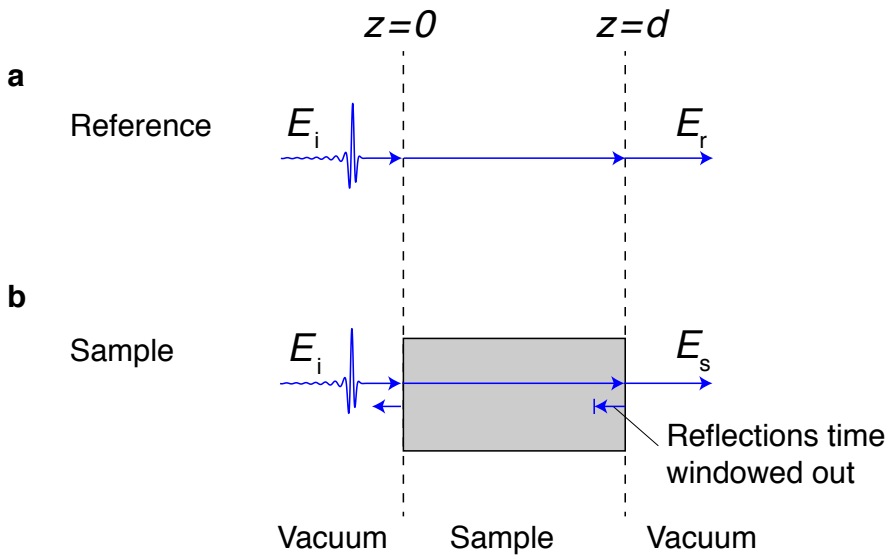


Figure 3.7: Transmission of a terahertz pulse through: **a** vacuum and **b** a thick sample of thickness d.

The transmission though a thick film can be defined similarly to the thin film case except now the Fabry-Pérot echoes can be time windowed out by the experiment. Consider a monochromatic plane wave incident on **a** vacuum and **b** a thick sample, the electric fields E_r and E_s transmitted are defined by

$$E_\mathrm{r} = e^{i(\tilde{n}_\mathrm{v} d)\omega/c} E_\mathrm{i} \tag{3.21}$$

$$E_\mathrm{s} = t_{\mathrm{v,s}}\, t_{\mathrm{s,v}}\, e^{i(\tilde{n}_\mathrm{s} d)\omega/c} E_\mathrm{i}, \tag{3.22}$$

The transmission is given by

$$T(\omega) = \frac{E_\mathrm{s}}{E_\mathrm{r}} = \frac{4\tilde{n}_\mathrm{s}}{(1+\tilde{n}_\mathrm{s})^2}\, e^{i((\tilde{n}_\mathrm{s}-1)d)\omega/c}. \tag{3.23}$$

There are no analytic solutions for the complex refractive index, $\tilde{n}_\mathrm{s}$, for the above equation so $\tilde{n}_\mathrm{s}$ will need to be found numerically. Owing to the complex exponent in Equation 3.23, $T(\omega)$ is oscillatory in n-space which would lead to convergence issues if

a standard least squares fitting method is applied. To overcome this potential fitting difficulty, an alternate error function is used [76, 77] in the fitting algorithm, given by

$$\xi(n,\kappa) = \xi^2_{\mathrm{mod}}(n,\kappa) + \xi^2_{\mathrm{arg}}(n,\kappa), \tag{3.24}$$

where n and κ are the real and imaginary parts of the complex refractive index. The functions ξ_{mod} and ξ_{arg} are defined by

$$\xi_{\mathrm{mod}}(\omega; n,\kappa) = \log(|T(\omega; n,\kappa)|) - \log(|T_{\mathrm{meas}}(\omega)|) \tag{3.25}$$

$$\xi_{\mathrm{arg}}(\omega; n,\kappa) = \arg(T(\omega; n,\kappa)) - \arg(T_{\mathrm{meas}}(\omega)), \tag{3.26}$$

where T_{meas} is the measured value and T is the fitted value.

3.4.2.1 Temperature-dependent complex refractive index of z-cut quartz

Optical characterisation of thin films and non-freestanding samples requires the use of a suitable substrate. In the terahertz region of the electromagnetic spectrum, z-cut quartz is an ideal substrate owing to low terahertz absorption below 3 THz and an approximately constant refractive index. Accurate knowledge of the substrate's complex refractive index is important as this is used to deduce the photoconductivity of a sample (Equation 3.20). Optical constants have previously been measured using a grating infrared spectrometer at 10 K and 300 K [78]. I expand on this work using terahertz time-domain spectroscopy to analyse the complex refractive index between 0.5 THz and 6 THz at 10, 40, 80, 120, 160 200 and 300 K (Figure 3.8). A phonon mode is present that blue-shifts from 3.86 THz at 300 K to 3.96 THz at 10 K.

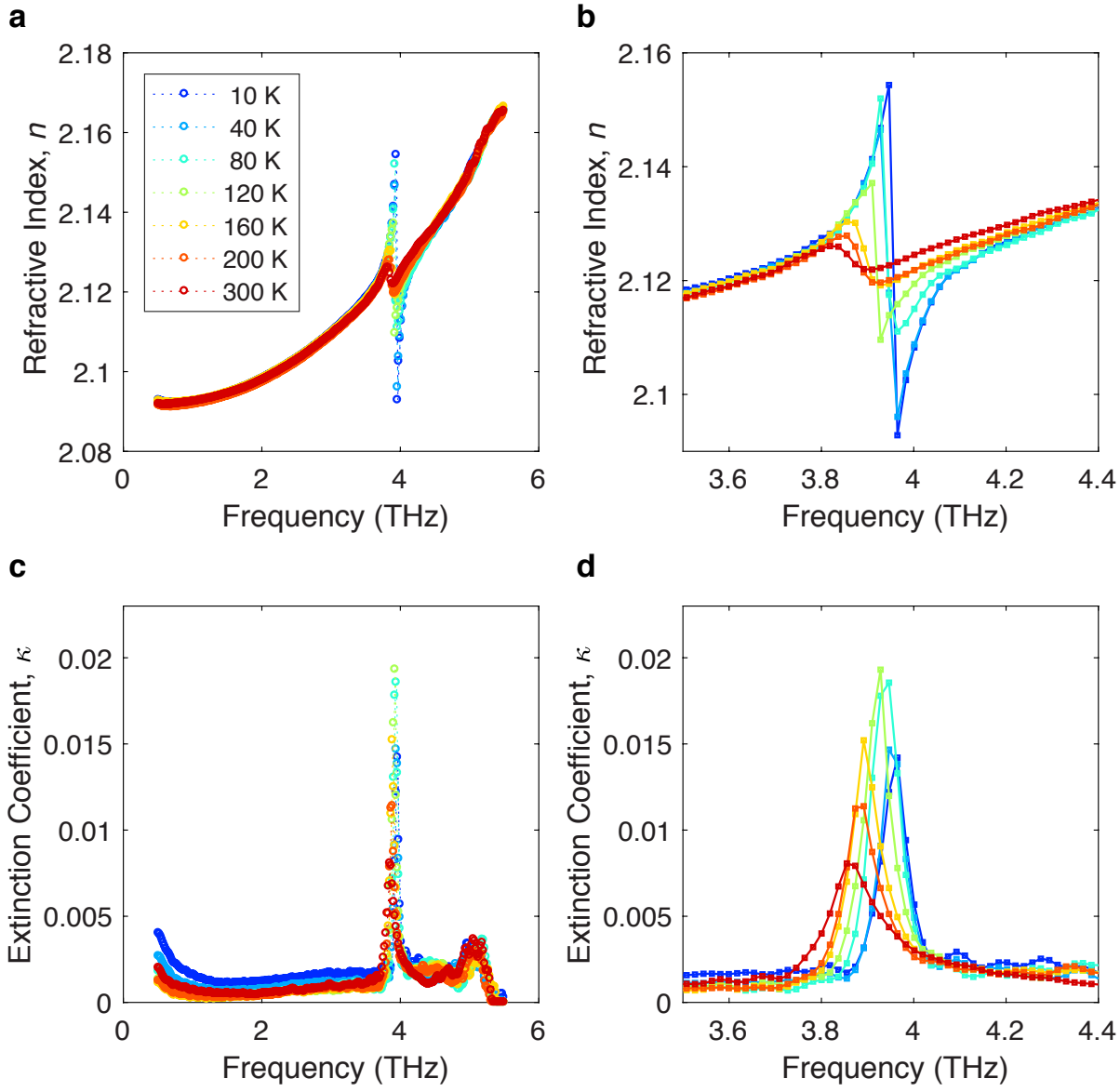


Figure 3.8: **a** and **b** Refractive index and **c** and **d** extinction coefficient of z-cut quartz between 0.5 and 6 THz. Measurements were taken using terahertz time-domain spectroscopy using a cold-finger cryostat at 10, 40, 80, 120, 160, 200 and 300 K. **b** and **d** are enlarged regions near the ∼3.9 THz phonon mode.

The temperature-dependence of the 3.9 THz phonon mode in z-cut quartz (Figure 3.9) is modelled by a Lorentz oscillator. The refractive index is fitted using two Lorentz oscillators to account for the ∼3.9 THz phonon mode and the presence of a broad phonon mode at ∼8 THz (=265 cm^{-1}) [78]. The refractive index is fitted with the following function

$$n(\omega) = \sqrt{\frac{|\tilde{\epsilon}_L(\omega)| + \mathrm{Re}\{\tilde{\epsilon}_L(\omega)\}}{2}}, \tag{3.27}$$

where ϵ_L is the relative dielectric function of two Lorentz oscillators given by

$$\tilde{\epsilon}_L(\omega) = \epsilon_\infty - \sum_{j=1}^{2} \frac{A_j \omega_j^2}{\omega^2 - \omega_j^2 - i\Gamma_j \omega}, \tag{3.28}$$

where ϵ_∞ is the high frequency dielectric constant, A_j is the oscillator strength, ω_j is the resonant phonon frequency with $\omega_{j=2}$ fixed at 8 THz [78], and Γ_j is the damping parameter.

Figure 3.10 shows (a) the oscillator strength, (b) the phonon resonant frequency, and (c) the damping parameter as a function of temperature that were extracted by fitting the model, Equation 3.27. The damping parameter, Γ increases with increasing temperature as expected. The oscillator strength decreases with increasing temperature and the phonon resonance redshifts with increasing temperature.

The complex refractive index of z-cut quartz at terahertz frequencies (0.5 THz to 5.5 THz) at temperatures between 10 K and 300 K has been presented above. These results will assist with future optical characterisation of non-free standing samples in the terahertz region, which rely on accurate knowledge of the refractive index and extinction coefficient of the substrate.

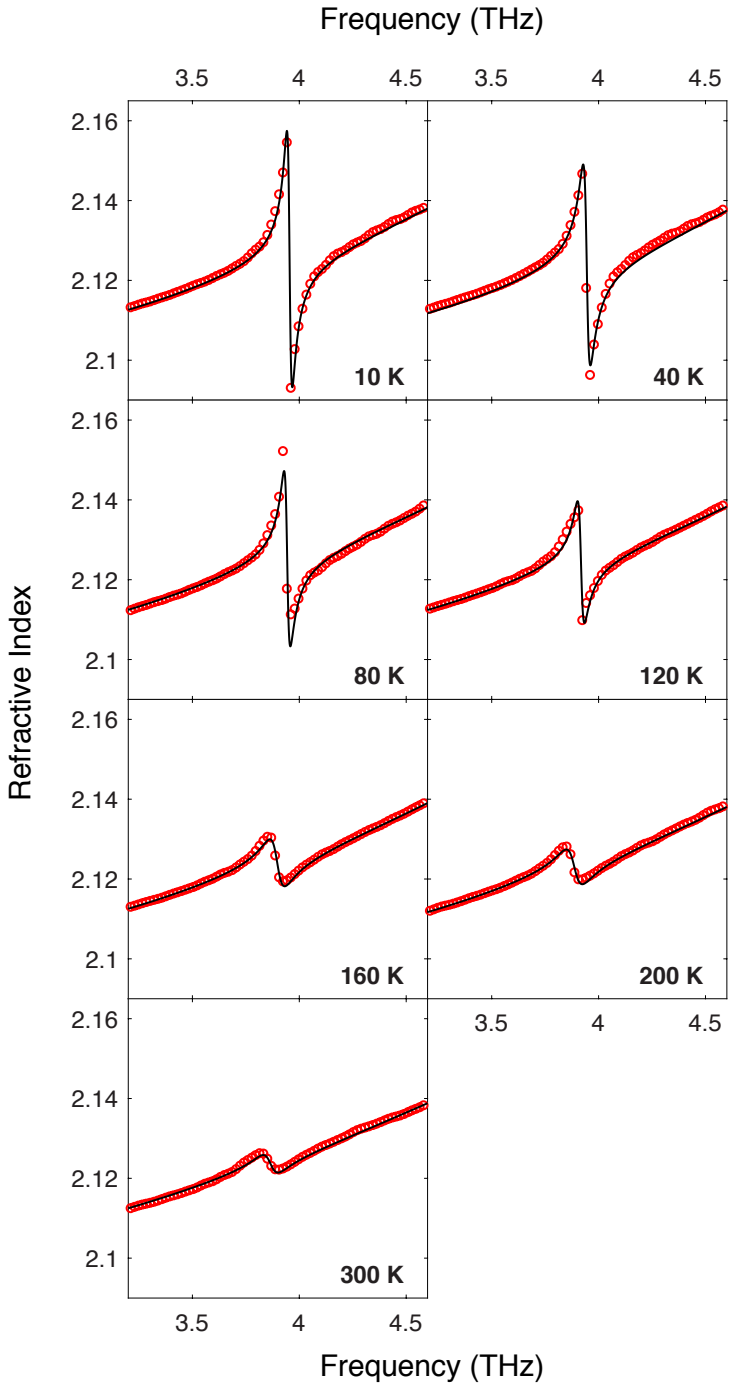


Figure 3.9: Refractive index of z-cut quartz near the 3.9 THz phonon mode with the data shown as red circles and fits shown as blue lines. The fitted data are modelled by a Lorentz oscillator as described in the text (Equation 3.27).

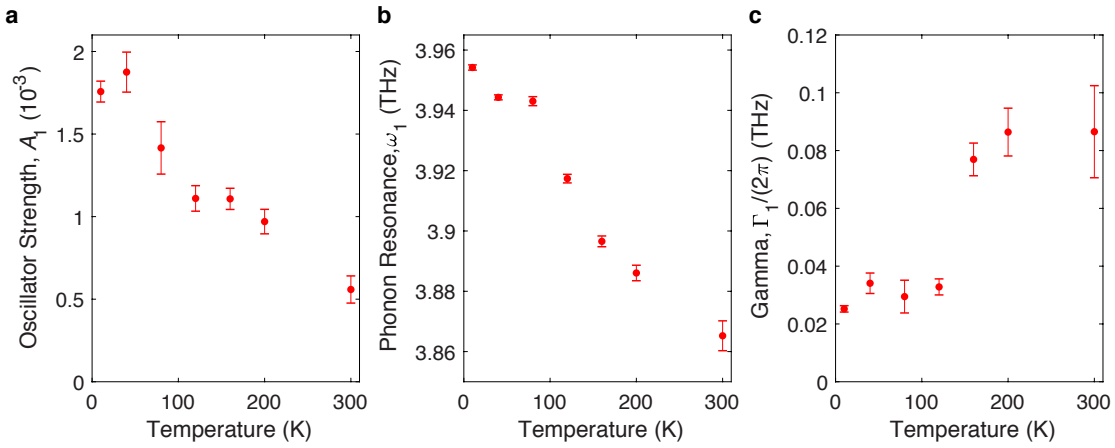


Figure 3.10: Extracted parameters from fitting an oscillator model (Equation 3.27) to the refractive index near the 3.9 THz phonon mode (Fig. 3.9) showing **a** the oscillator strength, **b** the phonon resonant frequency, and **c** the damping parameter as a function of temperature.

3.4.3 Mobility from Optical Pump Terahertz Probe Spectroscopy

The effective mobility of charge carriers $\phi\mu$ is given by [79],

$$\phi\mu = \frac{\Delta S}{en_{\text{eff}}}, \tag{3.29}$$

where ϕ is the excitation-photon-to-generated-free-charge branching ratio of bound to unbound electron and hole pairs generated and $\Delta S = \Delta\sigma d$ is the sheet conductivity. n_{eff} is the effective areal density of charge carriers, which takes into account the Gaussian profiles of the optical pump beam that excites charge carriers and the terahertz probe beam have Gaussian profiles. The effective areal charge carrier density is calculated by

$$n_{\text{eff}} = \frac{E_{\text{pulse}}}{E_{\text{photon}}}\frac{1}{A_{\text{eff}}}(1-R)(1-T), \tag{3.30}$$

where E_{pulse} and E_{photon} are the energies of the pump pulse and the photons (400 nm). R and T are the reflection and transmission coefficients at the a wavelength of 400 nm. The effective area, A_{eff} is given by

$$A_{\text{eff}} = \int_0^{\infty}\int_0^{2\pi} G(\zeta_{\text{pump}};r)G(\zeta_{\text{probe}};r)rdrd\theta, \tag{3.31}$$

where $G(r)$ are gaussian functions with full width half maxima of the pump (ζ_{pump}) and the (ζ_{probe}) beams. Evaluating A_{eff} gives

$$A_{\text{eff}} = \frac{\pi}{4\ln 2}\left(\zeta_{\text{pump}}^2 + \zeta_{\text{probe}}^2\right). \tag{3.32}$$

Substituting these expressions into Equation 3.29 gives

$$\phi\mu = \left(-\epsilon_0 c(1+\tilde{n}_{\text{r}})\frac{\Delta T}{T}\right)\frac{1}{e}\frac{E_{\text{photon}}}{E_{\text{pulse}}}\frac{\pi}{4\ln 2}\frac{\zeta_{\text{pump}}^2+\zeta_{\text{probe}}^2}{(1-R)(1-T)}. \tag{3.33}$$

3.4.4 Photoconductivity of Intra-excitonic Transitions

Excitonic states in semiconductors consist of discrete bound states and a continuum of unbound states analogous to a hydrogenic system. The photoconductivity response, $\Delta\sigma$, of transitions from the 1s state to np states and continuum states is described, as a function of angular frequency ω, by the sum of Lorentz oscillators with an oscillator strength given by Fermi's Golden Rule. [80, 81, 82] The photoconductivity of intra-excitonic transitions is given by

$$\Delta\sigma(\omega) \propto -i\omega\epsilon_0 \left(\sum_{n=2}^{\infty} \frac{f_{1s\to np}}{\omega_n^2 - \omega^2 - i\omega\Gamma} + \int_{E_X/\hbar}^{\infty} \frac{f_{1s\to\infty}(\omega')d\omega'}{\omega'^2 - \omega^2 - i\omega\Gamma} \right), \tag{3.34}$$

where Γ is a broadening parameter, ϵ_0 is the permittivity of vacuum, ω_n is the transition energy, and $f_{1s\to np}$ and $f_{1s\to\infty}$ are the oscillator strengths for the 1s $\to$ np and 1s $\to \infty$ transitions, respectively. The transition energy is given by

$$\omega_n = \frac{E_X}{\hbar}\left(1 - \frac{1}{n^2}\right), \tag{3.35}$$

where E_X is the exciton binding energy. The oscillator strengths are determined using Fermi's Golden Rule

$$f_{i\to f} = \frac{2\pi}{\hbar}(E_f - E_i) \,|\, \langle\psi_f|\hat{x}|\psi_i\rangle \,|^2, \tag{3.36}$$

where subscripts i and f denote the initial and final states. The matrix elements for bound and unbound states have been evaluated by Hee-Won Lee[81] and leads to oscillator strengths given by

$$f_{1s\to np} = 2\pi\omega_n \left(2^4 n^{7/2} \frac{(n-1)^{n-5/2}}{(n+1)^{n+5/2}} \right)^2 \tag{3.37}$$

and

$$f_{1s\to\infty}(\omega) = 2\pi\omega \frac{2^4}{\sqrt{3}(1+x^2)^{5/2}} \frac{e^{-\frac{2}{x}\tan^{-1}(x)}}{(1-e^{-2\pi/x})^{1/2}}, \tag{3.38}$$

where $x = \sqrt{\hbar\omega/E_{\mathrm{X}} - 1}$. The contribution to the photoconductivity for transitions to the continuum states is negligible, and the contributions are fitted for states from $n = 1$ to $n = 40$.

Chapter 4

Bimolecular Recombination in Methylammonium Lead Triiodide Perovskite

4.1 Introduction and Background

The past five years have seen intense research into the nature of hybrid lead halide perovskites used as active layers in photovoltaic devices [27, 25, 83]. Improvements in fabrication processes have led to rapid increases in light-to-electrical power conversion efficiencies beyond 22%, placing these semiconductors at the centre of potentially cheap and sustainable energy production [13, 84]. Such rapid advances have brought into question the fundamental physical mechanisms that set the ultimate limits to essential properties such as charge-carrier mobilities [20], exciton binding energies[85] and intrinsic (bimolecular) recombination between electrons and holes.

At the heart of a solar cell is the absorbing layer, which is the only layer by design in which incident light should excite charge-carriers. Following absorption of photons, excited electrons and holes are only of use if they can be extracted at electrodes

to contribute to a photocurrent. Such extraction is impeded by competing charge-carrier recombination processes, which can occur through a variety of mechanisms [24]. The fundamental physical processes governing the dynamics of charge-carriers in the absorbing layer hence play a dominant role in the conversion process of photons into storable energy.

Previous transient spectroscopic experiments have revealed the value of rate constants associated with different charge-recombination processes in hybrid perovskites, based on the measurements of transient absorption [86, 87, 88, 89], photoluminescence [90, 91, 92], and terahertz photoconductivity [79, 93] dynamics. The significance of each process varies with the density of charge-carriers in the material and thus the intensity of incident light. Under low-level illumination, monomolecular (Shockley-Read-Hall [94]) processes mediated by trap sites such as elemental vacancies, substitutions or interstitials [95] will dominate charge-carrier recombination. However, with increasing charge-carrier density, bimolecular (radiative) recombination between unbound electrons and holes will begin to take over, while at even higher densities, many-body Auger recombination will contribute [25].

Any analysis of charge-carrier recombination mechanisms therefore has to be placed in the context of solar irradiation levels (AM1.5) at which Auger recombination was found insignificant [93]. Instead, charge-recombination under AM1.5 results from a trade-off between trap-related monomolecular and intrinsic bimolecular electron-hole recombination [25], with the latter dominating when monomolecular recombination lifetimes exceed $10\,\mu$s. Reductions in trap concentration through rapidly improving material processing protocols mean that this limit is already being approached [96, 97], opening the prospect of single-junction solar cells operating near the Shockley-Queisser limit [98].

Such developments have brought into sharp focus the fundamental nature of bimolecular recombination between electrons and holes in the continuum states of the

conduction- and valence-bands, which will operate in defect-free metal halide perovskites under solar illumination. Despite the importance of this process, relatively little is known about its mechanism to date. While studies have shown bimolecular recombination in hybrid perovskites to be highly non-Langevin [79, 99, 22, 100, 101], there is currently no consensus on suitable alternative models. Some studies have suggested that direct band-to-band transitions govern bimolecular recombination, including fully theoretical work which however currently cannot account for the complexities of Coulomb correlations [102], and experimental work examining the switch-over point of luminescence intensity between the trap-mediated recombination regime at low charge-carrier densities, and the bimolecular regime at higher densities [103]. However, other studies have hypothesised a range of more exotic influences, including: Rashba spin-orbit coupling [104]; a mixture of indirect and direct band gap states [105]; and relativistic effects [106]. Identification of the correct mechanism can be further complicated by the potential presence of electronic transitions between multiple and non-parabolic bands and an energy-dependence of the associated matrix element, which have not been evaluated with certainty to date.

In this chapter, bimolecular electron-hole recombination in lead iodide perovskites is shown unambiguously to be able to be understood in terms of the inverse process to absorption, analogous to the case of GaAs [107, 108, 109] and silicon [110, 111]. With the help of insights gained from *ab initio* calculations regarding the validity and applicability of Elliott's theory to $CH_3NH_3PbI_3$, the contributions to absorption from bound electron-hole pairs (excitons) from those of unbound electrons and holes in the continuum states of the semiconductor can be correctly unravelled. This approach allows a demonstration of a clear correlation between the temperature-dependent changes in absorption spectra of charge-carriers and the rate of bimolecular charge-carrier recombination.

4.2 Sample Fabrication

Dual-source thermal evaporation was used to grow thin films of $CH_3NH_3PbI_3$ on z-cut quartz substrates under high vacuum as reported previously [17]. CH_3NH_3I and PbI_2 were placed in separate crucibles, and the substrates were mounted on a rotating substrate holder to ensure a uniform film was deposited. The temperature of the substrates was kept at 20 °C throughout the deposition and the chamber was allowed to reach a high vacuum (10^{-6} mbar). Once the deposition rate for CH_3NH_3I and PbI_2 had stabilised, the substrates were exposed to the vapour for 2 hours at a nominal growth rate of 0.6 Ås^{-1}. The deposition rates of both CH_3NH_3I and PbI_2 were monitored using a quartz crystal microbalance to ensure that a 1:1 molar ratio was achieved in the final composition of the film.

The thickness of the $CH_3NH_3PbI_3$ thin film was measured by a Hitachi S-4300 scanning electron microscope (SEM) image to be 435 ± 5 nm (Figure 4.1).

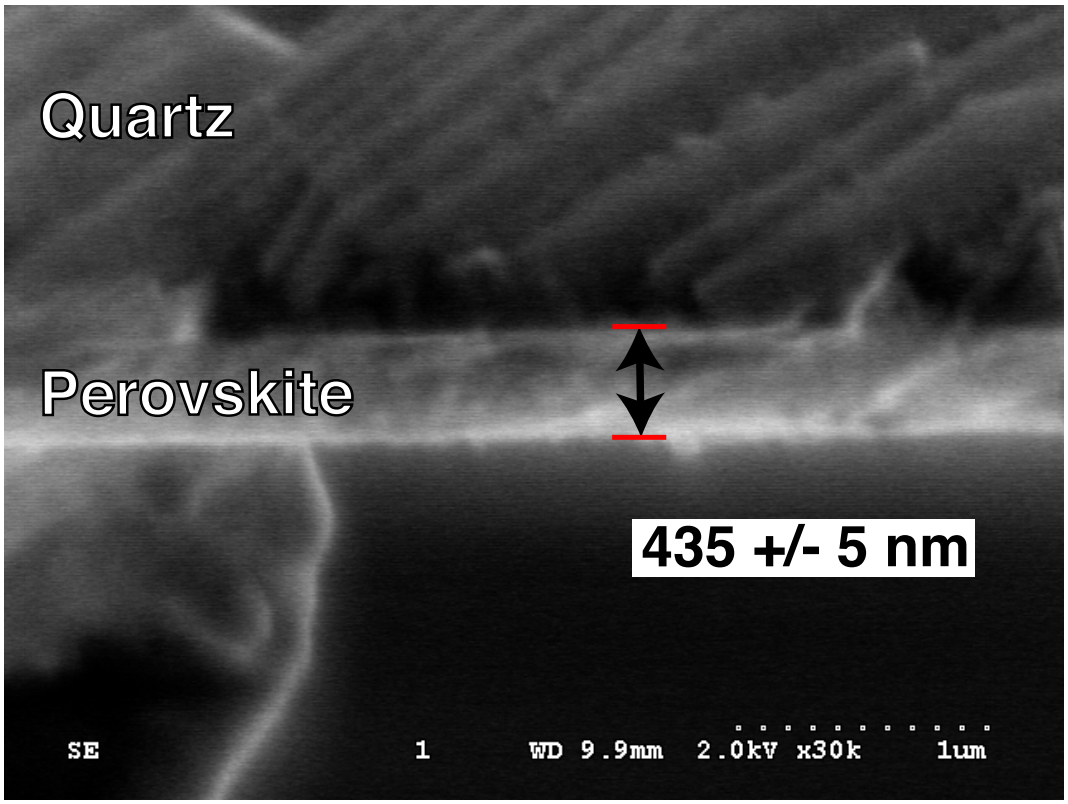


Figure 4.1: Cross-sectional scanning electron microscopy (SEM) image of a $CH_3NH_3PbI_3$ perovskite film, showing a thickness of $435 \pm 5\,\mathrm{nm}$.

4.3 Results and Discussion

4.3.1 Absorption

To probe whether bimolecular recombination between unbound electrons and holes is the reversal of absorption, an accurate separation of the contributions to the absorption from continuum states and from Coulombically bound electron-hole pairs (excitonic states) is needed. Such separation is usually achieved through Elliott's theory [52], however, previous attempts for metal halide perovskites have found significant deviations from experimental data for this theory at energies sufficiently above the band gap [89, 112, 113], which calls into question the rationale for using this model. Below, an analysis of absorption spectra for the most frequently investigated metal halide perovskite, $CH_3NH_3PbI_3$, is performed in combination with high-accuracy GW *ab initio* calculations to unravel the causes of such effects.

To determine the temperature-dependent absorption spectra of $CH_3NH_3PbI_3$ (Figure 4.2) reflection-transmission measurements were performed on thin films by use of a Fourier transform infrared (FTIR) spectrometer (see Section 3.2 for details). Thin films were fabricated through dual-source vapour deposition which yields smooth, uniform surfaces [114], as evidenced from the observation of Fabry-Perot oscillations (see Section 3.2) and sharp absorption onsets devoid of scattering effects that would otherwise complicate the modelling. Figure 4.3a shows the absorption spectra of $CH_3NH_3PbI_3$ at 4 K along with a fit based on Elliott's theory [52] within the first 100 meV above the band edge (full details are included in Section 2.1). Within this energy range, this theory is found to reproduce accurately the spectral shape of the absorption, however, at higher energies significant deviations occur.

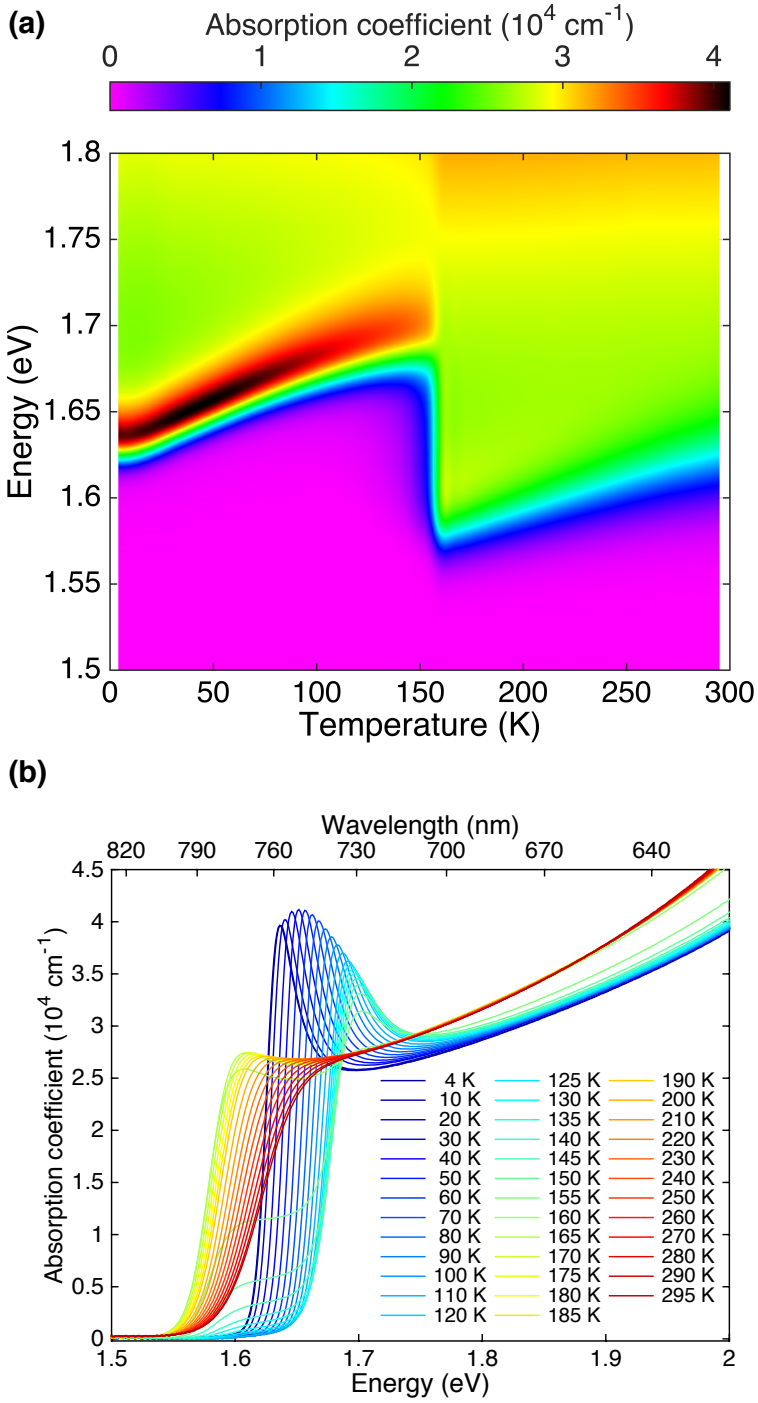


Figure 4.2: Absorption of $CH_3NH_3PbI_3$. (a) 2D colour map of the absorption spectra of $CH_3NH_3PbI_3$ as a function of energy and temperature. (b) Absorption spectra of $CH_3NH_3PbI_3$ as a function of energy at each temperature.

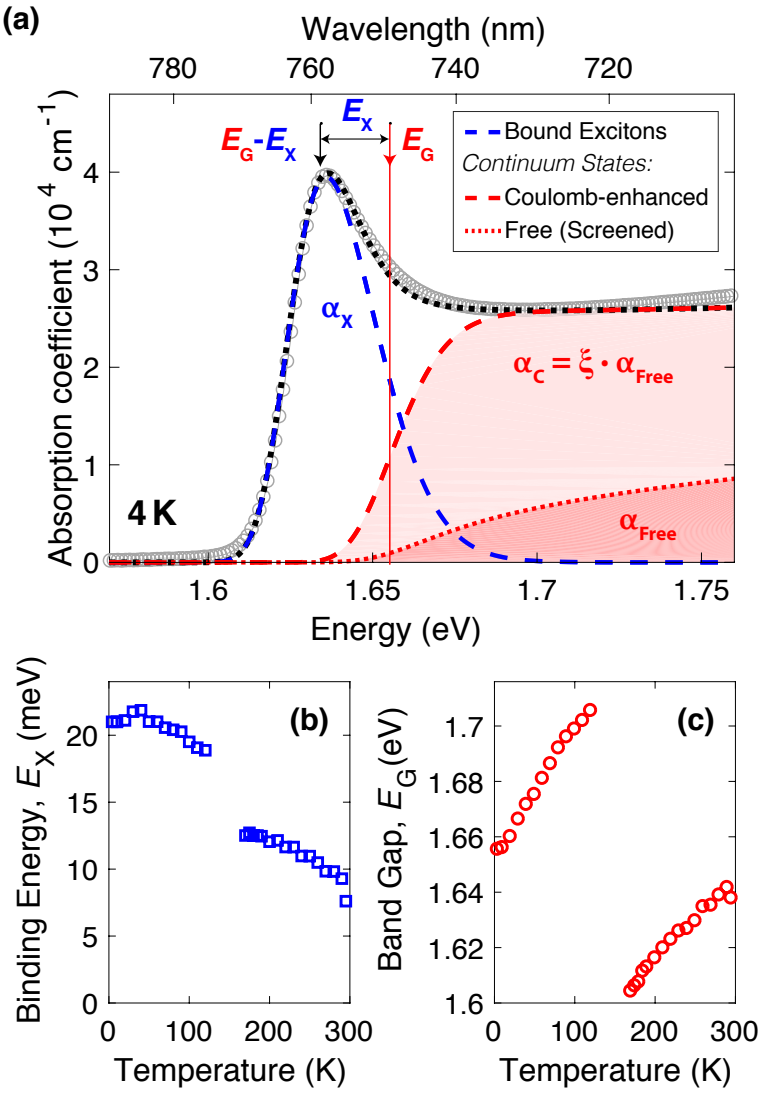


Figure 4.3: Absorption modelling of $CH_3NH_3PbI_3$. (a) Absorption spectrum of $CH_3NH_3PbI_3$ taken at 4 K. The black dotted line is a fit to the data based on Elliott's theory as described in the main text, which allows the separation of the contributions to the total absorption coefficient arising from bound excitonic states (α_X, blue dashed line) and Coulomb-enhanced electron-hole continuum states (α_C, red dashed line), which is increased beyond the absorption from free (screened) electrons and holes (α_{Free}, red dotted line) by the Coulomb-enhancement factor ξ. Arrows indicate the position of the band gap (E_G) and the value of the exciton binding energy (E_X). (b) Exciton binding energy and (c) band gap energy of $CH_3NH_3PbI_3$ as a function of temperature, obtained from fits based on Elliott's theory to the band edge absorption data shown in Figure 4.2b. The small gap in displayed points between 140 K to 170 K is owing to the coexistence of the orthorhombic (<140 K) and tetragonal (>170 K) phases [23] for this temperature range, which leads to unreliable fits to the absorption edge in this region.

A phase transition is evident in the absorption spectra (Figure 4.2a) and occurs in the range 140–170 K between the low-temperature orthorhombic and the tetragonal structures. At 155 K there is clear evidence of a coexistence of the two phases (Figure 4.2b) [23]. The excitonic absorption peak is most pronounced at low temperatures. At higher temperatures the peak becomes smeared out because of thermal broadening. The absorption coefficient (α) was obtained from the reflectance (R_s) and transmittance (T_s) by

$$\alpha = -\frac{1}{d} \ln \left(\frac{T_\mathrm{s}}{1 - R_\mathrm{s}} \right) \ , \tag{4.1}$$

where d is the thickness of the sample. Equation 4.1 is valid for samples on non-absorbing substrates such as the quartz substrates used in the study.

Elliott's theory accounts for the enhancement of light absorption through Coulombic attraction between electrons and holes in the conduction and valence bands of a semiconductor [52]. As Figure 4.3a illustrates, such interactions significantly increase the absorption coefficient near the band gap energy E_G beyond that expected for a free electron-hole picture. Here, Coulombic attraction leads to additional absorption into bound excitonic states ($\alpha_\mathrm{X}(E)$, blue dashed line) that manifest themselves as a series of hydrogenic peaks at energies below E_G. Importantly, even above E_G, Coulomb interactions substantially enhance the absorption coefficient for electron-hole continuum states ($\alpha_\mathrm{C}(E)$, red dashed line), by a factor $\xi(E)$ beyond that expected for free electrons and holes ($\alpha_\mathrm{Free}(E)$, dotted line). $\xi(E)$ is the Coulomb enhancement factor derived from the values of the band gap and binding energy (see Equation 2.15) and is therefore not a free (independent) parameter of the model. As a result, the continuum absorption spectrum differs from the classical square-root dependence expected for uncorrelated charges in a direct semiconductor (α_Free), resulting instead in a step-like onset at the band gap (α_C) [52, 113].

In addition, the model accounts for spectral broadening caused by electron-phonon interactions and energetic disorder [115] through convolution with a suitable function. An additional energetic disorder may lead to some element of inhomogeneous broadening. A log-normal distribution was found to be useful to parameterise this additional disorder brought into the system. Previous studies have found a distribution of band gap positions varying with crystallite size and even within a single crystal [116, 117]. The model can be described as the sum of the contributions of excitonic and continuum states convolved with a broadening function. The broadening function, $g(E)$, is a normalised function centred at the maximum and is the convolution of a normal distribution with temperature-dependent parameters, caused by electron-phonon coupling, and a log-normal distribution with two globally fitted parameters, caused by disorder and local fluctuations of the stoichiometry of the material. In mathematical notation,

$$g(E) = \mathcal{N}(0,\, \sigma_T^2) \otimes \ln\big(\mathcal{N}(u_\mathrm{s},\, \sigma_\mathrm{s}^2)\big)\ , \tag{4.2}$$

where $\otimes$ represents a convolution, u_s and σ_s are fitted globally and σ_T are temperature dependent parameters fitted for each temperature representing the electron-phonon coupling. $\mathcal{N}(0,\, \sigma_T^2)$ is a normal distribution with zero mean and variance of σ_T^2. $\ln(\mathcal{N}(u_\mathrm{s},\, \sigma_\mathrm{s}^2))$ is a log-normal distribution and has the form,

$$\ln\big(\mathcal{N}(u_\mathrm{s},\, \sigma_\mathrm{s}^2)\big) = \frac{1}{x}\frac{1}{\sqrt{2\pi\sigma_s^2}} \exp\left(-\frac{1}{2}\left(\frac{\log(x) - u_s}{\sigma_s}\right)^2\right) \tag{4.3}$$

The correct disentanglement of these excitonic and continuum states is key to unravelling the mechanisms of bimolecular recombination, which arises only from interactions between unbound electrons and holes. As discussed in more detail below, the possibility that the Coulomb interactions between charge-carriers are screened, which may occur at sufficiently high charge-carrier densities (above the Mott transi-

tion [118]) needs to be considered. Photon absorption also depends on the electric dipole matrix element, although is assumed to be independent of photon energy in Elliott's theory [52] and hence in the modelling of the experimental data as shown in Figure 4.3.

Figure 4.4 shows the contributions of bound excitonic states (α_{X}), Coulomb-correlated continuum states (α_{C}) and free (screened, α_{Free}) electrons and holes to the total absorption coefficient spectrum $\alpha(E)$ for a range of different temperatures, obtained from fits of Elliott Theory to the experimentally obtained absorption coefficient spectra. With decreasing temperature, excitonic effects are enhanced, leading to a larger discrepancy between α_{C} and α_{Free}.

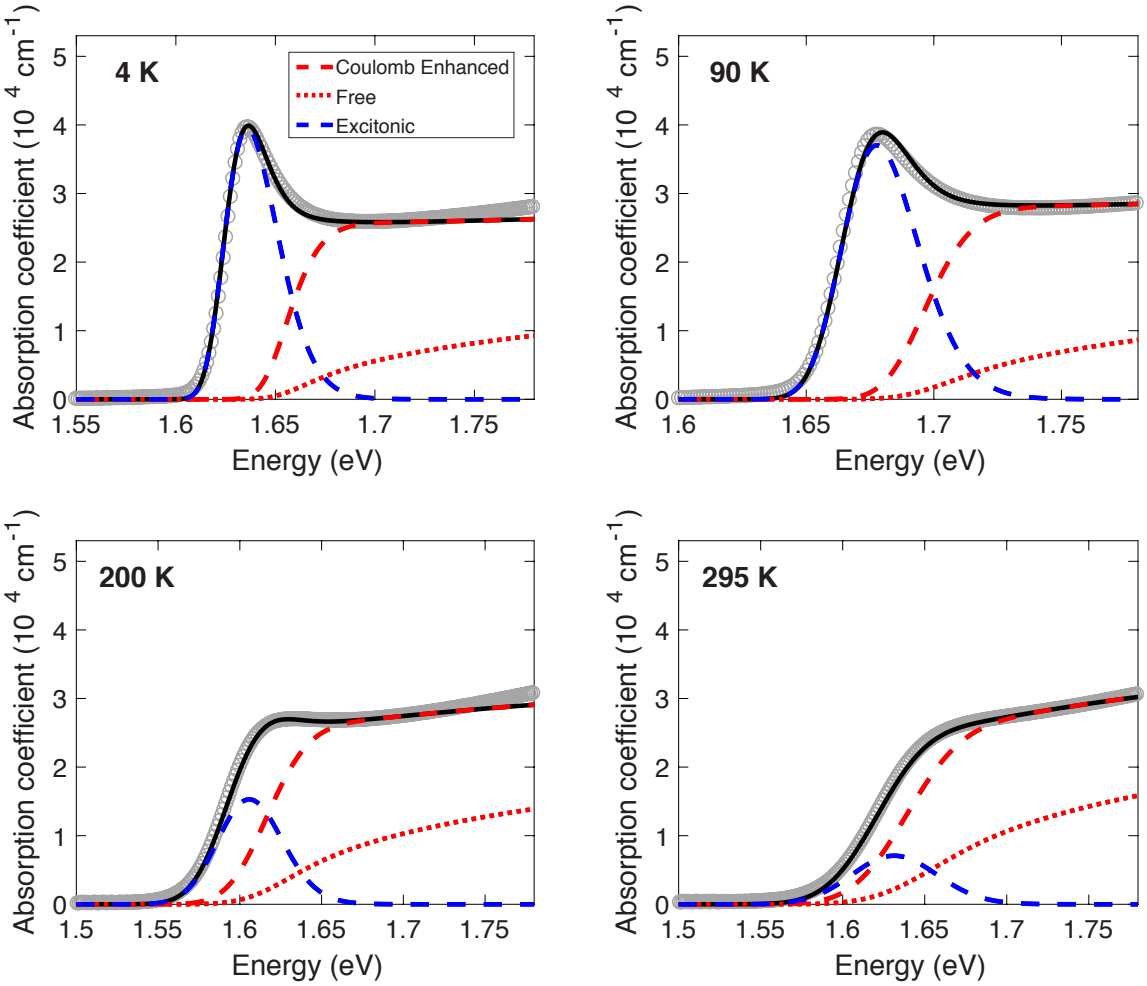


Figure 4.4: Contributions to the absorption onset. Contributions of bound excitonic states (α_{X}), Coulomb-correlated continuum states (α_{C}) and free (screened, α_{Free}) electrons and holes to the total absorption coefficient spectrum $\alpha(E)$ for a range of different temperatures, obtained from fits of Elliott Theory to the experimentally obtained absorption coefficient spectra.

A correct determination of the exciton binding energy E_X is a prerequisite for the accurate extraction of the continuum states. The value of E_X is determined to be 20 ± 2 meV for the low-temperature (0-160 K) orthorhombic phase from fits based on Elliott's theory, which is in good agreement with the low-temperature value of 16 ± 2 meV determined from magneto-absorption studies [85]. Figure 4.3b shows that the binding energy declines only slightly with temperature within each structural phase, apart from a rapid drop by $\sim$5 meV that occurs at the phase transition into the tetragonal structure. These changes can be understood in terms of temperature-dependent trends in the dielectric function at low frequencies; in particular, at the orthorhombic-tetragonal phase transition a step-change in permittivity [119] and hence exciton binding energy occurs. The trends with temperature of the binding energy are similar to those reported in previous studies [120, 121, 122] and the value of $E_X \sim 8$ meV at room temperature is commensurate with efficient exciton dissociation, as suggested in other studies [79, 120, 85, 123, 124, 121].

Careful modelling of the band-edge absorption also allows the extraction of values for the band gap energy that can be compared with those determined from *ab initio* calculations discussed below. Figure 4.3c illustrates that the extracted band gap energy E_G generally increases with temperature, in contrast with trends for typical inorganic semiconductors such as GaAs [125]. This phenomenon has previously been attributed to a reverse ordering of the band edge states [27, 126, 127, 128]. At the transition between the orthorhombic and tetragonal phases (160 K), E_G displays a noticeable discontinuity of 100 meV as previously observed [93] and deriving from changes in octahedral tilts [129].

4.3.2 Theoretical Calculations

As mentioned above, the use of Elliott's theory to model the absorption edge of $CH_3NH_3PbI_3$ has proven to be controversial, given that several studies (including

the present) found that satisfactory agreement could only be obtained for energies near the band edge [89, 112, 113]. It has been postulated that non-parabolicity of the conduction and valence bands could be to blame [130, 120, 103], however, this would have to be severe in order to account for the observed discrepancies. Here this controversy is resolved by showing that the divergence mostly arises from a break down of several assumptions that Elliott's theory is based on, which are that (i) only one valence and one conduction band are involved in the transitions; (ii) the bands are spherical (i.e. parabolic and isotropic); and (iii) the electric dipole transition matrix element is independent of photon energy. The validity of these assumptions is examined in the context of $CH_3NH_3PbI_3$ by conducting highly accurate first-principles calculations that can take into account potential non-parabolicity and higher-lying electronic transitions.

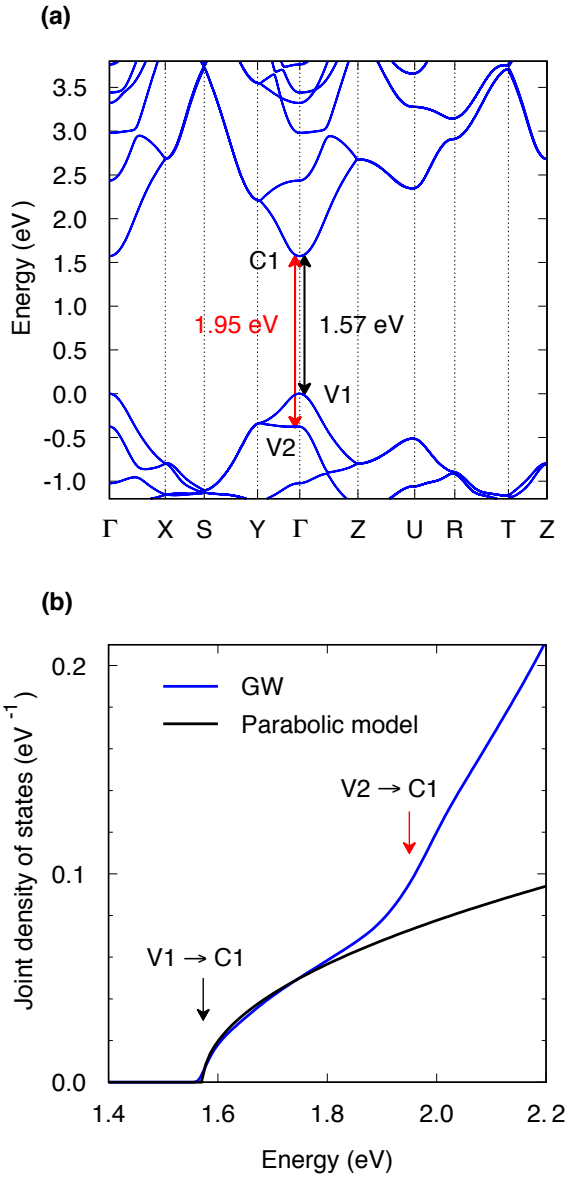


Figure 4.5: First principles calculations of $CH_3NH_3PbI_3$ carried out by Marina R Filip and Carla Verdi. (a) Quasiparticle band structure of $CH_3NH_3PbI_3$ calculated using the GW approximation (see [26] for details). The black arrowed line shows the direct band transition from the first valence band (V1) to the first conduction band (C1) at an energy of 1.57 eV. The red arrowed line shows the transition from the second valence band (V2) to C1, at an energy of 1.95 eV. (b) The joint density of states derived from GW calculations (blue line), compared with the function expected from a simple parabolic band model (black line). The two arrows mark the two lowest energy transitions corresponding to those marked in (a).

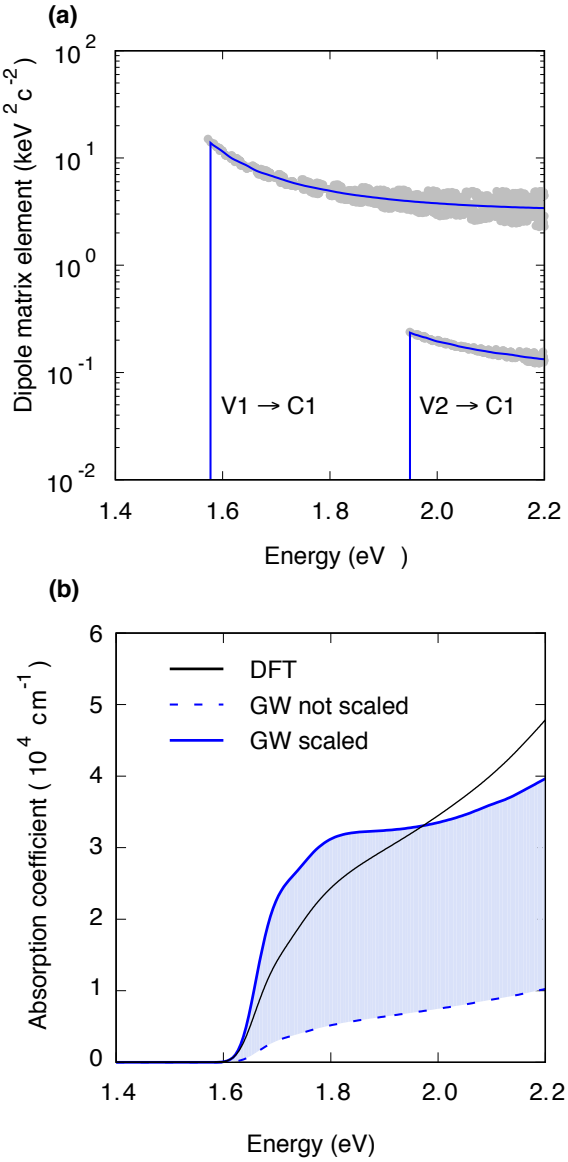


Figure 4.6: First principles calculations of $CH_3NH_3PbI_3$ carried out by Marina R Filip and Carla Verdi. (a) The electric dipole transition matrix element for the V1↔C1 and V2↔C2 transitions. Grey filled circles represent the matrix element as calculated at different k-points in the Brillouin zone. The blue lines show the value averaged over all directions in the Brillouin zone. (b) Absorption coefficient spectrum calculated from density functional theory (DFT) calculations (black), and GW calculations (blue) within the independent-particle approximation (i.e. without considering electron-hole Coulomb interactions). Results using scaled (solid) and unscaled (dashed) dipole matrix elements are reported. The light blue region represents the uncertainty in the magnitude of the optical absorption spectrum owing to the approximate calculation of the dipole matrix elements. The functions have been shifted along the energy axis to make the onset coincide with the experimental value of E_G.

Figure 4.5a shows the electronic band structure of $CH_3NH_3PbI_3$ calculated from first principles using the GW approximation. Details for all calculations can be found in previous articles [26, 131, 132]. A quasiparticle band gap (V1↔C1) of 1.57 eV is calculated, which is in good agreement with the band gap energy determined at 4 K (1.66 eV, see Figure 4.3c). The small difference between the calculated and measured band gaps derives from the absence of electron-phonon interactions in the calculations. Interestingly, the calculations also reveal the presence of another electronic transition (V2↔C1) with an onset energy of 1.95 eV, which is relatively close to the band edge and therefore has the potential to influence the shape of the absorption onset.

From the calculated GW electronic band structure, the quasiparticle electron and hole effective masses are able to be extracted, as shown in Table 4.1. Effective masses are calculated as the inverse of the second derivatives of the energy with respect to the wave vector at the Γ-point, with derivatives evaluated numerically from finite differences. The reduced effective mass of $0.11m_e$ is in excellent agreement with experimental values [85]. The accuracy of these calculations in terms of reproducing closely the experimental values of both band gap energy and effective masses highlights the power of the GW method, in comparison with traditional density-functional theory (DFT) which tends to underestimate effective masses and band gap energies [26].

With a conclusive computational framework in place, the possibility of non-parabolicity contributing to deviations from Elliott's theory is probed. The joint density of states using the quasi-particle eigenvalues is computed and contrasted with the trend expected for a simple parabolic onset based on the calculated reduced effective mass. As Figure 4.5b shows, the density of states associated with the V1↔C1 transition (onset 1.57 eV) is remarkably parabolic for photon energies of up to ∼250 meV above the gap. However, the second transition (1.95 eV; V2↔C1) makes a significant contribution to the joint density of states and will give rise to

	Theory (GW)	Experiment
E_G (eV)	1.57	1.66
m_h^*	0.23	-
m_e^*	0.22	-
μ	0.11	0.104 ± 0.003[85]

Table 4.1: Comparison between calculated and experimental band gap energies and effective masses. E_G, band gap at 4 K; m_e^* electron (C1) effective mass; m_h^* hole (V1) effective mass; μ=$((m_e^*)^{-1}+(m_h^*)^{-1})^{-1}$ reduced effective mass. Effective masses are given in units of the electron rest mass. The values of the electron and hole effective masses were obtained as isotropic averages of the diagonalized effective mass tensor at the Γ-point. *ab initio* calculations were carried out by Marina R Filip and Carla Verdi.

additional absorption, if it has significant oscillator strength. Hence the parabolic approximation assumed in Elliott's model will hold for photon energies within ∼250 meV of the band edge, but additional electronic transitions will lead to deviations already within the first ∼200 meV.

In addition, the validity of the assumption that the electric dipole transition matrix element is constant with photon energy in $CH_3NH_3PbI_3$ is examined. It has long been known for inorganic semiconductors such as silicon or germanium that significant deviations may occur from this simplifying approximation [133]. Therefore the matrix element at a number of different k-points in the Brillouin zone relating to different energy transitions (Figure 4.6a) is calculated. Grey circles are the calculated values at different k-points with the average value shown as a blue line. The results clearly demonstrate that the matrix element decreases significantly with increasing energy for both the V1↔C1 and V2↔C1 transitions; therefore Elliott's approximation of constant matrix element will only hold close to the band edge. In addition, the magnitude of the V2↔C1 transition is found to be approximately one order of magnitude lower than that of the V1↔C1 transition, which means that its contribution to absorption above 1.95 eV is not as significant as in the un-weighted joint

density of states.

This rigorous evaluation of all factors contributing to the absorption allows the absorption coefficient to be derived entirely from *ab initio* calculations, as shown in Figure 4.6b for both DFT and GW approximations. An accurate calculation of the absorption coefficient within the GW approximation requires the inclusion of the off-diagonal terms of the GW self-energy, which is computationally prohibitive for the case of $CH_3NH_3PbI_3$. Instead, in Figure 4.6b two limits of the GW absorption spectra obtained using the dipole matrix elements calculated from DFT, both before and after scaling with respect to the quasiparticle transition energies are shown. Figure 4.6b shows that the absorption coefficient is sensitive to scaling, and can vary by up to a factor of 4, while the shape of the spectrum does not vary significantly. Moreover, it can be shown that the f-sum rule in these two cases is either overestimated, if the matrix elements are scaled, or underestimated in the unscaled case, consistent with the respective magnitudes of the absorption coefficient shown in Figure 4.6b. For this reason, the true absorption coefficient is proposed to be bracketed by the scaled and unscaled GW spectra, which give good agreement with the experimental data (α_{Free}, Figure 4.3a). This result indicates that the inclusion of band non-parabolicity, higher-lying transition and the functional dependence of the matrix element are fundamental for the accurate evaluation of the absorption coefficient in $CH_3NH_3PbI_3$. Hence these *ab initio* calculations have enabled each assumption that Elliott's theory is built on to be individually explored, allowing its validity for hybrid perovskite semiconductors to be probed. Overall, this analysis conclusively reveals that deviations from Elliott's theory for $CH_3NH_3PbI_3$ are a reflection of a breakdown in the assumptions the model is based on, for energies somewhat higher than the band edge. The evaluation of these factors however suggest that within $\sim$100 meV the simplified assumptions of Elliott's theory holds, allowing an analysis of band-edge charge-carrier recombination based on the continuum states extracted from this model to be performed.

4.3.3 Recombination

4.3.3.1 van-Roosbroeck Shockley Relation

With a comprehensive picture of the contributions to the absorption onset in place, the link between bimolecular recombination of electrons and holes, and the reverse process of light absorption by continuum states is discussed. Figure 4.7 shows a schematic diagram linking the Fermi-Dirac distributions of electrons and holes with absorption and emission processes as mediated by the Bose-Einstein functions of the photon radiation field. To validate such links, the temperature-dependent bimolecular recombination rate constants that would be expected according to the van Roosbroeck-Shockley (Section 2.2 and [54]) relation for absorption by electrons and holes in the presence and absence of Coulomb correlations is first evaluated. The calculated rate constants is then compared with those obtained from transient spectroscopy, showing excellent agreement for both absolute values and temperature trends.

The theory of photon-radiative recombination of electrons and holes was first developed by van Roosbroeck and Shockley [54] and applies the principle of detailed balance to the thermal equilibrium rate of photon absorption, i.e. it assumes the rate of radiative recombination at thermal equilibrium at a certain frequency to be equal to the rate of generation of electron-hole pairs by thermal radiation at the same frequency (see Figure 4.7) [134]. The van Roosbroeck-Shockley relation hence allows deduction of the radiative recombination rate and bimolecular recombination rate constant from steady-state absorption spectra. The theory is based on the assumption of unit quantum efficiency and is applicable to a material in which there is no k-selection rule, or to a non-degenerate material in which there is a selection rule [107, 55], and has extensively been applied to group IV, VI, and III-V direct and indirect semiconductors in the past [55].

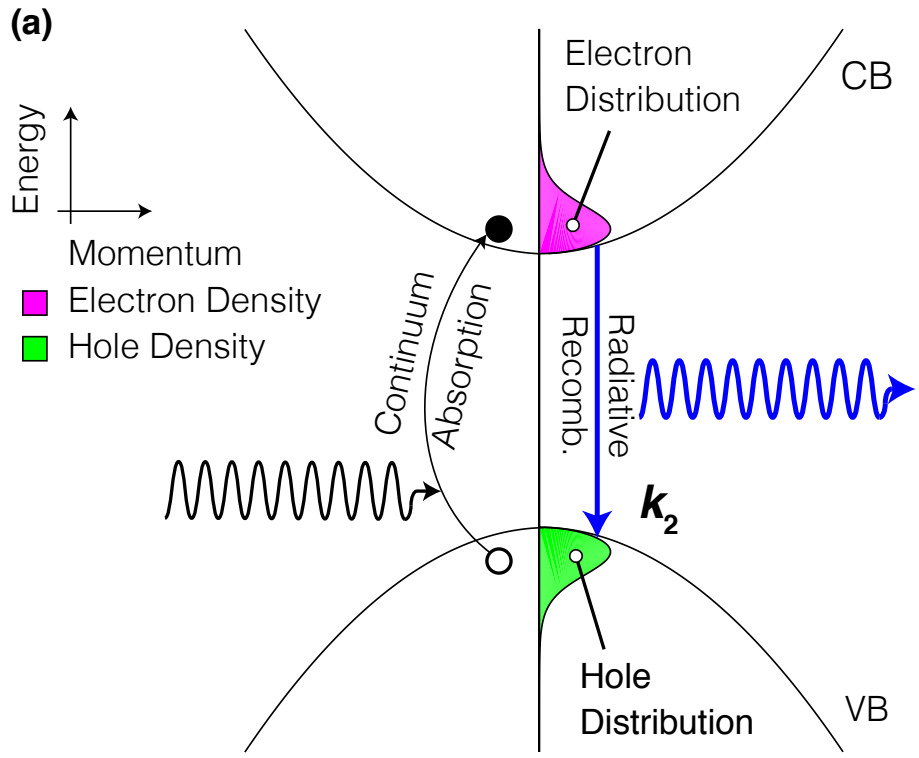


Figure 4.7: Schematic of the energy dispersion relation and charge-carrier distributions, which have a determining role in the bimolecular charge-carrier recombination process. The purple and green filled areas show the Fermi-Dirac distributions of the excited electrons and holes in the conduction and valence bands, respectively.

The van Roosbroeck-Shockley relation describes the temperature-dependent radiative recombination rate $R_{\mathrm{rad}}(T)$ by the following function [54],

$$R_{\mathrm{rad}}(T) = \int_0^\infty \rho(E,T)\, P(E,T) dE, \tag{4.4}$$

where $\rho(E,T)dE$ is the density of photons in the material in the interval dE, and $P(E,T)$ is the probability per unit time that a photon of energy E is absorbed and hence is proportional to the absorption coefficient. Dividing the radiative recombination rate by the square of the intrinsic carrier concentration, n_{i}, the bimolecular recombination rate constant, $k_2(T) = R_{\mathrm{rad}}(T)/n_{\mathrm{i}}^2(T)$, is able to obtained which is also often referred to as the "B-coefficient" in literature on inorganic semiconductors. All associated equations are detailed in full in Section 2.2. The intrinsic carrier concentration and the photon distribution are dependent on the Fermi-Dirac and Bose-Einstein distributions respectively, which vary strongly with temperature.

4.3.3.2 Considerations of Coulomb Correlation and Mott Densities

The van Roosbroeck and Shockley relation requires accurate knowledge of the absorption coefficient spectrum for the calculation of the radiative recombination rate, as indicated by Equation 2.24. However, as the previous section on Elliott's Theory has highlighted, careful consideration must be given to the extent to which excitonic effects are taken into account.

The principle of detailed balance demands that transitions between any two states occur with equal frequency and in either direction at equilibrium and also prevents the maintenance of equilibrium by means of cyclic processes [135]. Figure 4.8 shows a schematic of the energy levels for a semiconductor taking into account Coulomb correlation. For this coupled system of free carriers in the continuum states and bound electron-hole pairs in the excitonic states the rate equations are as follows

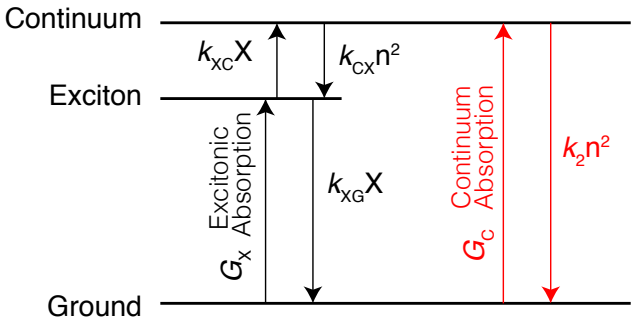


Figure 4.8: Two-particle picture schematic of the energy-levels of the ground state and excited states (exciton and continuum) of a semiconductor and the respective transitions between these states.

[136, 137],

$$\frac{dn}{dt} = G_{\mathrm{C}} + k_{\mathrm{XC}}X - (k_{\mathrm{CX}} + k_2)n^2 \tag{4.5}$$

$$\frac{dX}{dt} = G_{\mathrm{X}} - (k_{\mathrm{XC}} + k_{\mathrm{XG}})X + k_{\mathrm{CX}}n^2, \tag{4.6}$$

where X and n are the exciton and free charge carrier densities with generation rates G_{C} and G_{X} respectively. k_{XC}, k_{CX}, and k_{XG} are rate constants for transitions between the ground, exciton and continuum states as detailed in Figure 4.8, and k_2 is the desired rate constant of bimolecular recombination. At thermal equilibrium and with black body radiation being the only source for generation, each process must be equally balanced by the reverse process. Hence, the rate at which photons are absorbed and excite electrons and holes into the continuum states must be equally matched by the rate of emission resulting from recombination of electrons and holes in the continuum states. Similarly, the rate at which photons are absorbed and excite electrons and holes into bound excitonic states is also equally matched by exciton recombination. Likewise, excitons dissociate to free electrons and holes in the continuum states at the same rate as formation of excitons from free electrons and holes in the continuum states. Therefore the rates can be written

$$G_{\mathrm{C}} = k_2 n_{\mathrm{i}}^2 = R_{\mathrm{rad}}^C \tag{4.7}$$

$$G_{\mathrm{X}} = k_{\mathrm{XG}} X_0 = R_{\mathrm{rad}}^X \tag{4.8}$$

$$k_{\mathrm{XC}} X_0 = k_{\mathrm{CX}} n_{\mathrm{i}}^2, \tag{4.9}$$

where X_0 and n_{i} are the equilibrium densities of excitons and free electrons and holes respectively, with n_{i} given by Equation 2.32. The total radiative recombination will be the sum of the excitonic recombination and free electron-hole recombination to the ground state, however, only the latter is a second order process under equilibrium conditions. Hence, the absorption coefficient that should be used in the van Roosbroeck and Shockley relation in order to determine the bimolecular rate constant (k_2) is the absorption coefficient of the continuum states, with or without Coulombic enhancement, and here these two possibilities are discussed.

Past studies for the case of silicon [110, 111] discussed the role of Coulomb interactions for the radiative recombination between electrons and holes in the conduction and valence band. In the presence of Coulomb correlations, absorption is strengthened by the energy-dependent factor ξ and the Coulomb-enhanced spectrum $\alpha_{\mathrm{C}}(E)$ may be used, while in the absence of such interactions, $\alpha_{\mathrm{Free}}(E)$ may be used in Equation 4.4. In general, Coulomb correlations increase the probability of an electron and a hole to exist in the same space, and therefore such interactions should *a priori* be included in a calculation of k_2. However, at charge-carrier densities n, exceeding the Mott density n_{M}, Coulomb interactions will be effectively screened by the presence of the high background charge-carrier density, therefore the free electron-hole absorption α_{Free} is the relevant quantity.

4.3.3.3 Mott Density

The Mott density n_{M} places a quantitative value on the transition from an insulating gas of excitons at lower densities to a metal-like state of an electron-hole plasma at high charge-carrier densities [118]. The electrostatic force between charged particles is a continuous function of their relative distances to each other, therefore it is intrinsically challenging to define a distinct density at which a Mott transition occurs. Hence a wide range of expressions for the Mott density have been proposed, which depend on different model assumptions and complexities, and whose validity is also temperature dependent. Since there is not a strong consensus in the literature on which expression best describes the transition, a range of values for the Mott densities n_{M} are discussed as they emerge from different equations given in the literature as follows [138, 139, 118, 140],

$$n_{\mathrm{M}}^{\mathrm{Mott}} = \left(\frac{0.2}{a_{\mathrm{B}}}\right)^3 \tag{4.10}$$

$$n_{\mathrm{M}}^{\mathrm{Edwards}} = \left(\frac{0.26}{a_{\mathrm{B}}}\right)^3 \tag{4.11}$$

$$n_{\mathrm{M}}^{\text{Klingshirn-1}} = 1.19^2 \frac{\epsilon_{\mathrm{r}}^{\mathrm{X}} \epsilon_0 k_{\mathrm{B}} T}{e^2 a_{\mathrm{B}}^2} \tag{4.12}$$

$$n_{\mathrm{M}}^{\text{Klingshirn-2}} = r^{-3} \left(\frac{4}{3}\pi a_{\mathrm{B}}^3\right)^{-1} \text{ and typically } 1 < r < 5 \tag{4.13}$$

$$n_{\mathrm{M}}^{\mathrm{HaugSchmittRink}} = 0.028 \frac{k_{\mathrm{B}} T}{E_{\mathrm{X}} a_{\mathrm{B}}^3}, \tag{4.14}$$

where a_{B} is the Bohr radius of the exciton, given by

$$a_{\mathrm{B}} = a_{\mathrm{H}}\ \epsilon_{\mathrm{r}}^{\mathrm{X}}\ \frac{m_{\mathrm{e}}}{\mu}, \tag{4.15}$$

with a_{H} the Bohr radius for hydrogen ($5.29 \times 10^{-11}\,\mathrm{m}$) and μ the reduced mass of the electron-hole system (here assumed to be 0.11 as determined from GW and shown in Table 4.1). In the article by Haug and Schmitt-Rink [140], the Mott density determined by the temperature-dependent Equation 4.14 was found to be close to the experimentally determined Mott transition for germanium at 30 K. The results presented here are between 50K and 300K and the expressions given by Equations 4.10-4.14 are expected to be valid over these ranges.

Evaluation of Equations 4.10-4.14 and 4.15 also requires knowledge of the value of the dielectric function at the frequency corresponding to the exciton binding energy. This value of $\epsilon_{\mathrm{r}}^{\mathrm{X}}$ is able to be determined as a function of temperature from the exciton binding energy E_{X} (as extracted from fits based on Elliott's Theory to the absorption spectra) using

$$\epsilon_{\mathrm{r}}^{\mathrm{X}} = \sqrt{\frac{13.6\,\mathrm{eV}}{E_{\mathrm{X}}}\frac{\mu}{m_{\mathrm{e}}}}. \tag{4.16}$$

Figure 4.9 shows the resulting values of the exciton binding energy, Bohr radius, relevant dielectric function and Mott density as a function of temperature. Over the temperature range for which k_2 has been evaluated in this work, the Mott densities n_{M} from the above expressions are found to lie in the range of a few $10^{18}\,\mathrm{cm}^{-3}$ to $10^{16}\,\mathrm{cm}^{-3}$, with a surprisingly wide spread of possible values resulting from these different expressions. This wide range mostly results from slightly different assumptions on the exact value the product $n_{\mathrm{M}}^{1/3} a_{\mathrm{B}}$ assumes in order for the Mott criterion to hold (i.e. the assessment of the distance to which excitons can approach one another before screening effects start to dominate). Since the assumed critical distance enters the

various equations as a power of three, any slight changes in these assumptions can lead to very large differences in the resulting Mott density, as evident in Figure 4.9d.

To assess if screening affects the values of k_2 measured in typical transient spectroscopic measurements, comparison of values stipulated for the Mott density with those at which bimolecular processes begin to feature under pulsed photoexcitation are needed. Accurate extraction of k_2 from transient charge-carrier density decays requires the generation of charge-carrier densities for which this process begins to dominate over trap-related recombination. The charge-carrier-density dependent recombination rate is given by [25] $K(n) = k_1 + nk_2 + n^2k_3$, where k_1, k_2 and k_3 are the rate constants for monomolecular, bimolecular and Auger processes. Hence, the onset of significant bimolecular recombination is expected to occur when nk_2 exceeds k_1, i.e. at charge-carrier densities $\tilde{n}>(\tau k_2)^{-1}$, where $\tau=k_1^{-1}$ is the trap-related (monomolecular) recombination lifetime. For typical values τ between 10 ns and 1 μs for $MAPbI_3$ [25] one obtains values for $\tilde{n}$ that range between $10^{15}\,cm^{-3}$ and $10^{17}\,cm^{-3}$. These values fall mostly below those shown in Figure 4.9d although they clearly come close enough that some element of Coulomb screening may be present. In addition, a typical transient spectroscopic experiment will be based on laser excitation pulses that have a spatially varying intensity profile and which generate an exponentially decaying absorption profile through the film depth, as expected from Beer's law. Therefore, a distribution of charge-carrier densities will be present, some of which may fall above, and some below the Mott density. The considerations above therefore only serve as a rough guide, but they suggest that transient experiments sensitive to k_2 may fall into the limit below the Mott transition, for which electron-hole recombination is enhanced though Coulomb correlations, making comparison with calculations based on the van Roosbroeck and Shockley relation using the absorption coefficient of continuum states, α_C, the most viable. However, for charge-carrier denisties mostly in excess of n_M, the use of α_{Free} clearly becomes more appropriate, although changes

to the absorption onset arising from band-filling effects may then also have to be included in such calculations for a fully accurate evaluation.

In summary, with values of n_{M} found to be distributed around $10^{17}\,\mathrm{cm}^{-3}$ for temperatures between 50 K and 295 K, calculations of k_2 to compare with experimental measurements obtained from transient spectroscopy should be based on the full (Coulomb-enhanced) continuum absorption $\alpha_{\mathrm{C}}(E)$ for charge-carrier densities n below the Mott density n_{M}, and on the the screened absorption spectrum $\alpha_{\mathrm{Free}}(E)$ for $n > n_{\mathrm{M}}$.

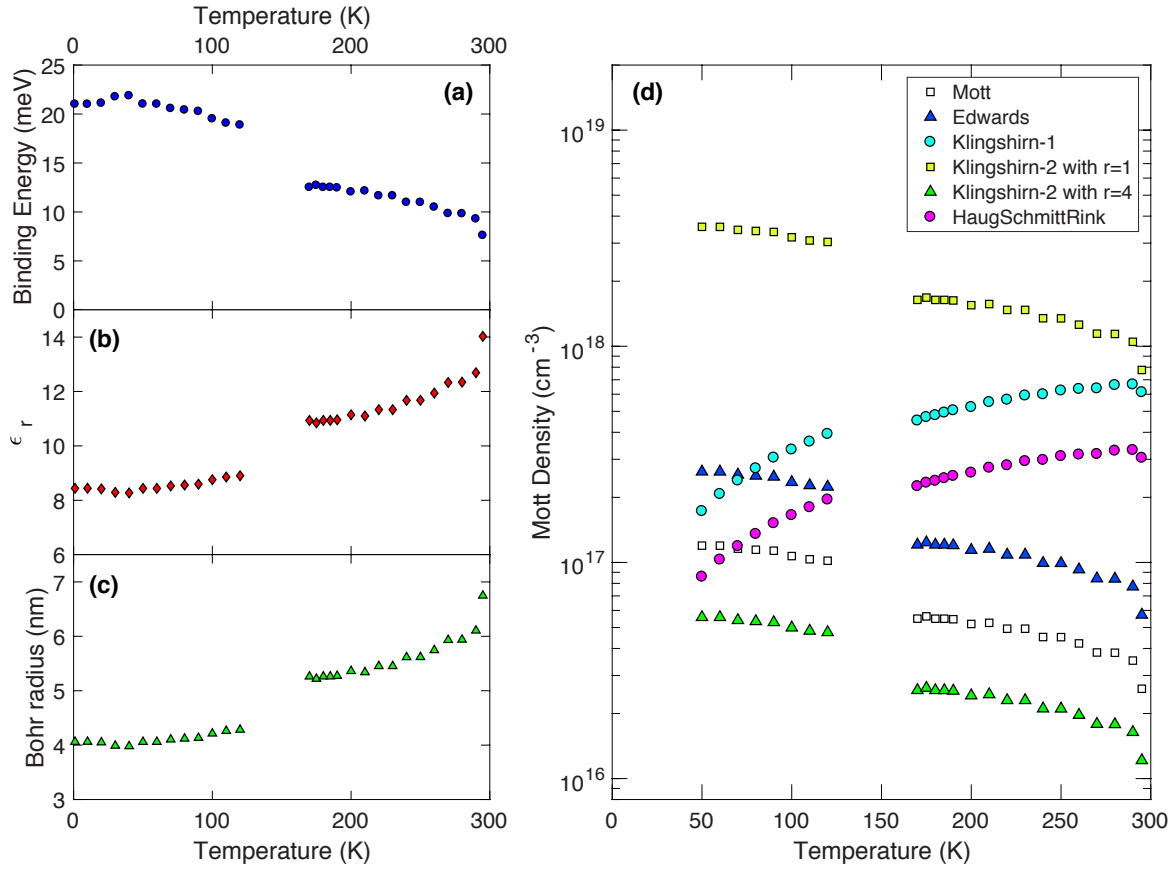


Figure 4.9: Mott density derived using the extracted exciton binding energy. (a) Exciton binding energy extracted from fits of Elliott Theory to absorption spectra, which was then used for the calculation of (b) the value of the dielectric function at a frequency relevant to exciton formation (c) the exciton Bohr radius and (d) the Mott density, as described by Equations 4.16, 4.15 and 4.10-4.14 respectively.

4.3.3.4 Bimolecular Recombination

Figure 4.10 displays the temperature-dependence of the bimolecular recombination rate constant k_2 derived from the unbound electron-hole absorption coefficient spectra through the van Roosbroeck-Shockley relation, for the case of Coulomb-enhanced absorption ($\alpha_{\mathrm{C}}(E)$, white triangles) and screened Coulomb interactions ($\alpha_{\mathrm{Free}}(E)$, red triangles), i.e. above and below the Mott transition. Points obtained from the absorption spectra measured at different temperatures were well represented by the following phenomenological functions (shown as black lines on the graph):

Temperature-dependent value of k_2 for Coulomb-enhanced electron-hole recombination:

$$k_2(T;\alpha_{\mathrm{C}}) = 1.36 \times 10^{-10}\,\mathrm{cm^3 s^{-1}} \times \exp\left(\frac{702\,\mathrm{K}}{T + 49.6\,\mathrm{K}}\right) \tag{4.17}$$

Temperature-dependent value of k_2 for the case of screened interactions:

$$k_2(T;\alpha_{\mathrm{Free}}) = 0.81 \times 10^{-10}\,\mathrm{cm^3 s^{-1}} \times \exp\left(\frac{340\,\mathrm{K}}{T + 19.2\,\mathrm{K}}\right) \tag{4.18}$$

At room temperature, Coulomb enhancement of the continuum absorption increases the bimolecular recombination constant by about a factor 4 with respect to the case of screened interactions. This discrepancy increases with decreasing temperature as Coulomb enhancement effects become more prominent. For both cases, the value of k_2 increases by roughly one order of magnitude between room temperature (295 K) and 50 K. The analysis reveals that this increase is directly linked with the sharpening of the Fermi-Dirac and Bose-Einstein distribution functions with decreasing temperature, with changes in absorption (and hence refractive index) making only a very minor contribution by comparison. As the photon distribution function and the thermal spread of electrons and holes across the conduction and valence bands

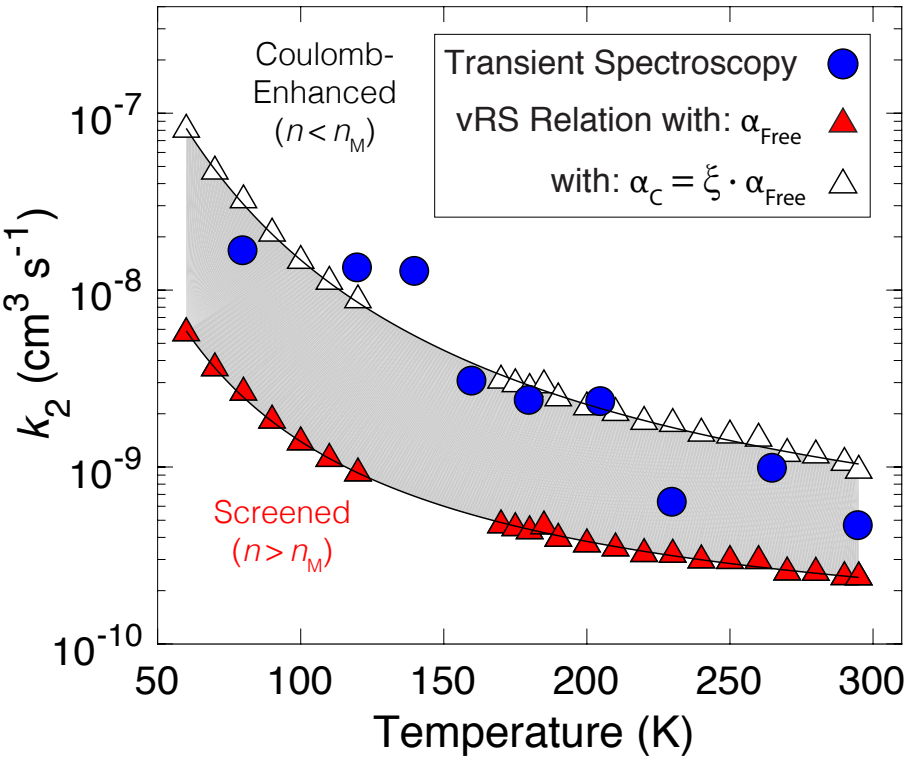


Figure 4.10: Temperature dependence of bimolecular recombination rate constant (k_2) in $CH_3NH_3PbI_3$, displayed on a semi logarithmic scale. Triangles show k_2 as deterimined through the van Roosbroeck and Shockley relation from fits to the experimentally obtained absorption spectra, based on either the electron-hole continuum absorption coefficient including Coulomb interactions (α_C, white triangles), or the free (screened) electron-hole coefficient (α_C, red triangles), with the former applicable at low charge-carrier densities ($n<n_M$) and the latter for charge-carrier densities exceeding the Mott density n_M. Points were fitted with phenomenological expressions (solid line) given by Equations 4.17 and 4.18. Blue circles show values of k_2 obtained previously[93] from transient terahertz photoconductivity spectroscopy that monitors free-charge carrier recombination dynamics, as corrected for internal self-absorption effects[141] to yield intrinsic values of k_2.

narrow, bimolecular recombination is substantially enhanced.

To validate this overall approach, these trends are compared with values obtained from terahertz photoconductivity transients, as reported in a previous study [93] and corrected for self-absorption effects [141, 142, 143, 144, 145] to yield the intrinsic values of k_2 (see [26] for details). Figure 4.10 reveals that temperature-trends observed in transient spectroscopy agree very well with those derived from the van Roosbroeck-Shockley relation. A comparison in terms of absolute values shows that these transient spectroscopic data are closest to the case of Coulomb-enhanced (unscreened) bimolecular recombination, although most points fall within the intermediate regime (shaded region). This result is not surprising, given that a clear observation of bimolecular processes in transient spectroscopy requires excitation with laser pulse fluences for which these recombination events begin to dominate over trap-related recombination that is prominent at lower charge-carrier densities. As suggested previously [25] and discussed above, this case applies at charge-carrier densities above $\sim 10^{15}$–$10^{17}\,\mathrm{cm}^{-3}$ for typical $CH_3NH_3PbI_3$, which may potentially come near the Mott density (Figure 4.9). However, a recent study [82] reported the direct observation of excitonic Rydberg states following excitation with fluences one order of magnitude higher than the highest fluence utilized for the transients against which the calculated values of k_2 are referenced here. Therefore it is concluded that the most adequate scenario for comparison is with values obtained from the Coulomb-enhanced (unscreened) absorption coefficient, for which Figure 3b also indicates best agreement. Hence the analysis clearly supports the notion of an inverse absorption process leading to bimolecular recombination in $CH_3NH_3PbI_3$.

These findings have direct impact on the use of hybrid perovskites in photovoltaic applications because they inherently connect the requirement for strong light absorption near the band edge with the presence of significant electron-hole recombination. However, this fundamental link in no way inhibits the efficient operation of

photovoltaic devices based on $CH_3NH_3PbI_3$. While faster bimolecular charge-carrier recombination will shorten charge-carrier diffusion lengths, it also mandates higher absorption coefficients, and hence absorber layers can be made thinner to compensate. Charge-carrier diffusion lengths for thin hybrid perovskite films are already in the micron regime [90], which exceeds their typical thickness in solar cells of a few hundred nanometers, thus allowing excellent charge-carrier extraction to electrodes. Therefore, while the mechanism identified here poses a fundamental hurdle to a reduction of bimolecular recombination, it does not preclude the development of high-efficiency photovoltaic cells based on lead halide perovskites. In addition, these findings demonstrate that bimolecular (radiative) recombination rate constants will depend to some extent on light intensity levels. Under solar illumination [25], charge-carrier densities in $CH_3NH_3PbI_3$ are near $10^{15}\,cm^{-3}$ to $10^{16}\,cm^{-3}$ and therefore below the Mott density, leading to Coulomb-enhanced electron-hole recombination. However, implementation in solar concentrators could lead to charge-carrier densities nearer $10^{18}\,cm^{-3}$, for which bimolecular recombination rate constants are likely to be reduced as a result of screening.

4.4 Summary

With the efficiency of perovskite photovoltaic cells rapidly increasing, the Shockley-Queisser limit is not too far from reach. The physical processes behind bimolecular electron-hole recombination in $CH_3NH_3PbI_3$, which will dominate over trap-assisted monomolecular recombination once this limit is approached have been examined . The direct comparison between bimolecular recombination rate constants derived from the van Roosbroeck-Shockley relation, with those extracted from transient spectroscopic measurements, demonstrates that these processes can be seen as the inverse to absorption. The established validity of the van Roosbroeck-Shockley relation further

demonstrates that photon emission derives from fully radiative [103, 25, 142, 141] band-to-band transitions, which in this case involve the recombination of thermalized electrons and holes across a direct bandgap. The sharpening of photon, electron and hole distribution functions is shown to enhances the bimolecular radiative rate by roughly an order of magnitude as the temperature is lowered from room temperature to $\sim$50 K. In addition, the highly accurate GW *ab initio* calculations have clearly identified the salient factors defining the shape of the absorption onset, such as non-parabolicity, higher-lying transitions and the correct functional dependence of the matrix element. Furthermore, screening of the Coulomb interactions between electrons and holes above the Mott transition is shown to reduce bimolecular recombination constants, meaning that such values have to be considered in the context of the charge-carrier densities present. These findings thus provide a fundamental understanding of the electronic processes in these hybrid perovskites, which will allow for guided exploration of alternative stoichiometries with desirable photovoltaic properties.

Chapter 5

Impact of the Organic Cation on the Optoelectronic Properties of Formamidinium Lead Triiodide

5.1 Introduction

Metal-halide perovskites have received an immense amount of interest owing to their potential use as light-absorbing materials in photovoltaic devices. Over recent years, such perovskite solar cells have seen an exciting rise in performance, with current formamidinium lead triiodide based devices achieving efficiencies of over 20 % [146]. High charge-carrier mobilities [20, 147, 21, 148, 141] combined with long carrier lifetimes [149, 79, 22, 24, 25] have been shown to underpin the excellent performance of metal-halide perovskites. In addition, the diversity of deposition techniques, including spin coating [14, 15], vapour deposition [16, 17, 18], and ink-jet printing [19], along with a relatively low cost of fabrication, makes metal-halide perovskites both economically and also physically favourable for rapid commercialization.

While the wealth of research into metal-halide perovskites is rapidly growing, most

investigations into the fundamental optoelectronic properties have been focused on the prototypical methylammonium lead triiodide perovskite ($MAPbI_3 = CH_3NH_3PbI_3$). Formamidinium lead triiodide ($FAPbI_3 = CH(NH_2)_2PbI_3$) on the other hand has received far less attention, perhaps because the choice of the A-cation in the ABX_3 perovskite structure was thought to have a relatively subtle influence on the electronic properties [150, 151, 115]. Here $FAPbI_3$ is investigated to highlight clear differences with $MAPbI_3$ in terms of optoelectronic and structural properties, and their dependence on temperature.

The variation in dielectric environment resulting from differences in the choice of A-cation has the potential to influence the Coulomb interactions in hybrid perovskites. As a consequence of such Coulomb interactions, discrete excitonic states may be formed from bound electron and hole pairs at energies below the band gap [52, 26]. Stronger Coulomb interactions in a material lead to a larger exciton binding energy, and also enhance the optical absorption coefficient of the above-gap unbound continuum states for charge carriers [52, 26]. The value of the exciton binding energy E_X in $MAPbI_3$ has been repeatedly investigated by numerous methods, including absorption onset modelling, photoluminescence quenching, and magneto-absorption, as summarized in Ref. 24. However, reported values vary widely [24] owing to the challenges of directly observing excitonic transitions in these materials. Accurate knowledge of E_X for a range of hybrid perovskites would be highly useful to the development of perovskite solar cells, given that excitons can only contribute to a photocurrent if efficient exciton dissociation is able to occur at the operating temperature of the device [123, 152].

Intra-excitonic transitions take place upon absorption of low energy photons, typically on the order of a few milli-electron volts. Direct observation of such transitions can therefore be made with light in the terahertz frequency regime ($1\,\mathrm{THz} = 4.1\,\mathrm{meV}$) at low temperature, for which excitonic states persist against thermally induced dis-

sociation. In the absence of an electron-hole population in the conduction and valence band of the hybrid perovskite, terahertz absorption may also result from excitation of lead-halide lattice vibrations [99, 153, 154]. Crucially, the presence of an additional optical pulse in optical-pump terahertz-probe spectroscopy (OPTPS) will photoexcite electrons and holes, allowing a distinction to be made between such vibrational signatures and transitions between excitonic states. OPTPS has therefore been successfully used for the determination of the exciton binding energy in classical inorganic semiconductors such as GaAs-AlGaAs quantum wells [155, 156, 80, 75]. Here, photoexcitation of the semiconductor initially generates a highly non-equilibrium distribution of electrons and holes in the conduction and valence bands, respectively, whose thermalisation occurs on a sub-picosecond timescale, populating exciton states [157]. In OPTPS, a subsequently arriving broadband terahertz pulse (0-15 meV) then probes the presence of excitons through intra-excitonic transitions that predominantly occur between the 1s to np states, from whose energy the exciton binding energy can be directly inferred.

Aside from a focus on excitonic effects, the mechanisms determining the charge-carrier mobility in hybrid perovskites have also recently received much scrutiny [115, 20, 158]. An understanding of the interactions and scattering processes that limit the mobility of charge-carriers is highly useful, because it can aid the design of novel hybrid perovskites optimized for photovoltaic applications [20, 53, 158]. It had recently been shown that the charge-carrier mobility in hybrid lead halide perovskites is mostly governed by Fröhlich [159] interactions between longitudinal optical phonons and charge-carriers [115]. However, such assertions could potentially be at odds with the $T^{-1.5}$ temperature dependence of the charge-carrier mobility μ repeatedly observed [93, 148, 124, 160] for $MAPbI_3$. Recent theoretical calculations [158] have suggested that in the limit of Fröhlich coupling, the temperature dependence should instead be closer to $\mu \sim T^{-0.5}$. For $FAPbI_3$, on the other hand, knowledge of the de-

pendence of the charge-carrier mobility on temperature is still outstanding. Here, OPTPS offers a non-contact method to probe the charge-carrier mobility, minimising extrinsic effects and allowing an exploration of such effects.

In this study, OPTPS is utilised to explore the photoconductivity and magneto-photoconductivity of $FAPbI_3$. At low temperature (10 K), direct transitions are observed between the 1s to np excitonic levels, from which a remarkably small exciton binding energy of 5.3 meV is determined. Magneto-OPTPS further reveals that the value of the exciton binding energy increases with magnetic field. Terahertz time domain spectroscopy (TDS) of $FAPbI_3$ is used to investigate changes in the phonon modes of Pb-I bond vibrations as a function of temperature. The phonon modes of $FAPbI_3$ show no splitting in the lower temperature phase which is in direct contrast with behaviour observed for $MAPbI_3$, highlighting differences in crystal structure. Further the temperature-dependence of the exciton binding energy and band-gap energy for $FAPbI_3$ is examined through modelling of the absorption coefficient near the band edge. Smooth changes are observed in values with temperature, which contrasts greatly with the discontinuities in the band gap and exciton binding energy typically observed at the orthorhombic-to-tetragonal phase transition in $MAPbI_3$. In addition, the charge-carrier mobility in $FAPbI_3$ is found to exhibit a temperature dependence of $T^{-0.5}$, again in contrast with previous observations for $MAPbI_3$, but in excellent agreement with theoretical expectations for electron-phonon coupling dominated by Fröhlich interactions.

5.2 Experimental Details

5.2.1 $FAPbI_3$ thin film fabrication by vapour-deposition

Formamidinium lead triiodide thin films were fabricated using thermal co-evaporation in a vacuum chamber. A dual-source evaporation system (Kurt J. Lesker) was used, with PbI_2 and FAI as precursors. Formamidinium iodide powder was obtained from Dyesol and PbI_2 beads from Alfa Aesar. The PbI_2 and FAI precursors were heated in separate crucibles until each of the precursors evaporated. During evaporation the pressure in the chamber stayed at approximately 10^{-6} mbar. For FAI the evaporation temperature was 150 °C, and PbI_2 was evaporated at 300 °C. The quartz substrates were mounted above the sources so that the vapours condensed on to the substrates and an $FAPbI_3$ film formed. The deposited films were annealed on a hotplate at 170 °C for 1 min to ensure that they were in the desired perovskite phase of $FAPbI_3$. This deposition method was previously confirmed and reported to result in smooth, uniform $FAPbI_3$ thin-films [18].

5.2.2 Terahertz time-domain spectroscopy (TDS)

Terahertz time domain spectroscopy (TDS - Section 3.3.1) was used to measure the absorption of phonon modes in $FAPbI_3$ and $MAPbI_3$. With TDS, the output of an amplified laser system with 30 fs pulses at a repetition rate of 5 kHz with a central wavelength of 800 nm and an average power of 4 W is split into two beam paths: a probe beam; and a gate beam. Terahertz pulses are generated by the inverse-spin Hall effect [61, 161, 62]. Terahertz pulses are detected by electro-optic sampling using a 0.2 mm thick GaP(110) crystal, Wollaston prism and a pair of balanced photodiodes. Temperature-dependent TDS measurements were performed using a cold-finger cryostat (Oxford Instruments). By measuring $FAPbI_3$ on a quartz substrate and taking reference measurement of a quartz substrate, the terahertz transmission in the time

domain can be obtained.

5.2.3 Optical pump terahertz probe spectroscopy (OPTPS)

Optical pump terahertz probe spectroscopy (OPTPS - Section 3.3.4) was used to measure the photoconductivity of $FAPbI_3$. OPTPS extends the TDS technique to allow measurement of a sample in the photoexcited state. In OPTPS, the sample is photoexcited by an optical pump, and after a short time delay is probed with a terahertz pulse. The generation and detection of the terahertz pulse is the same as in the TDS method detailed above. Transformation from the change in transmission with photoexcitation to photoconductivity is detailed in Chapter 3. Magneto-photoconductivity measurements were measured by magneto-OPTPS, which is the same as OPTPS but conducted in the presence of a magnetic field (Oxford Instruments Spectromagnet). For magneto-OPTPS, terahertz pulse were generated using optical rectification using a ZnTe crystal and were detected using a ZnTe crystal.

5.2.4 Fourier transform infrared spectroscopy

Fourier transform infrared (FTIR - Section 3.2) spectroscopy was used to determine the absorption coefficient spectra of $FAPbI_3$. Temperature-dependent reflectance transmission measurements of $FAPbI_3$ were performed using a FTIR spectrometer (Bruker Vertex 80v) with the sample mounted in a gas exchange cryostat (Oxford Instruments OptistatCF2). A tungsten halogen lamp was used as the illumination source, with a CaF_2 beamsplitter and a silicon detector.

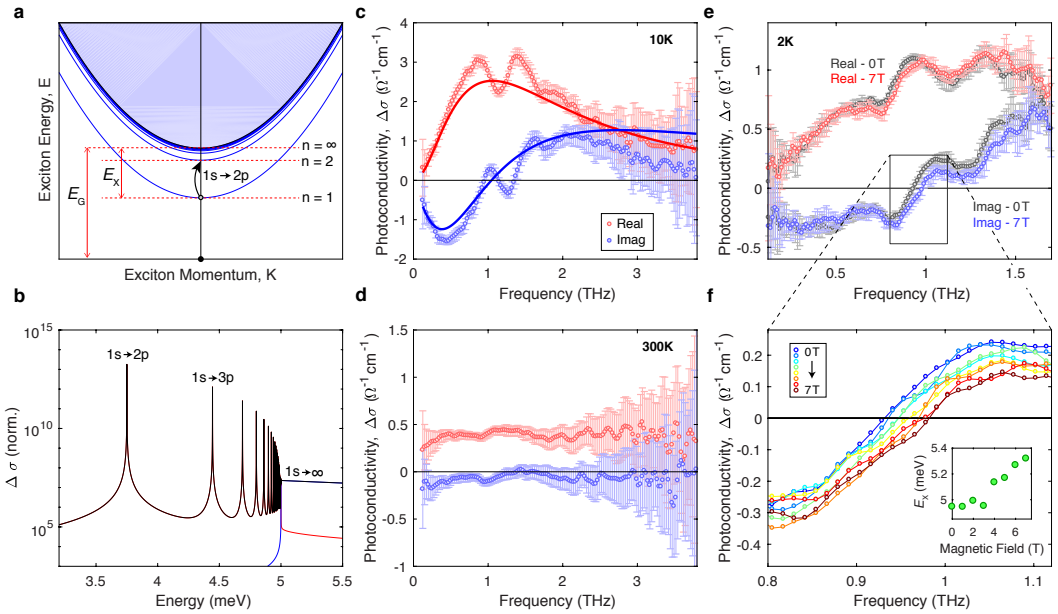


Figure 5.1: Intra-excitonic transitions in $FAPbI_3$ measured by photoconductivity spectra. **a** Exciton dispersion relation showing the discrete energy levels of the exciton at energies below the band gap. **b** Modelled photoconductivity spectra shown on a logarithmic scale, calculated from an intra-excitonic model of a 3-dimensional material with minimal broadening ($\Gamma = 1\ \mu$eV; see Section 3.4.4 for details). The bound states are shown as a red line and the continuum states are shown as a blue line, with the total shown in black. **c** and **d** Photoconductivity spectra of $FAPbI_3$ at 10 K and 300 K respectively. Oscillations in the spectra at 10 K between 0.8 and 1.7 THz are attributed to a modulation of the photoconductivity by phonon modes. Increasing error bars at higher frequencies demonstrate the bandwidth of the measurement. **e** Photoconductivity spectra at a magnetic field of 0 T (grey) and 7 T shown as red and blue for the real and imaginary parts, respectively. The spectrum at 7 T is found to be blue shifted with respect to the spectrum at 0 T. **f** Imaginary part of the photoconductivity spectra, taken at magnetic fields between 0 T (blue) and 7 T (red) in steps of 1 T. The inset in **f** shows the extracted exciton binding energy as a function of magnetic field. Photoconductivity spectra were measured by optical pump terahertz probe spectroscopy (OPTPS) using a 400 nm pump with a fluence of $\sim$10 μJcm^{-2} and a probe delay of 30 ps (**c** and **d**) and 500 ps (**e** and **f**).

5.3 Results and discussion

5.3.1 Excitonic Transitions

The study commenced by investigating intra-excitonic transitions between discrete excitonic levels in order to obtain an accurate value of the exciton binding energy in $FAPbI_3$. Such discrete energy levels are described by the expression $E_n = E_G - E_X/n^2$, where E_G is the energy of the band gap, E_X is the exciton binding energy, and n is a positive integer. Figure 5.1a illustrates schematically how such excitonic effects modify the dispersion diagram, leading to an exciton-momentum dispersion relation in the two-particle picture as a function of the centre-of-mass momentum, K, of the exciton. Since THz photoconductivity spectroscopy is used in this study to explore the inter-excitonic resonances, Figure 5.1b illustrates the expected photoconductivity spectrum of intra-excitonic transitions, calculated for a material with minimal broadening ($\Gamma = 1\,\mu$eV - see Section 3.4.4 for details). The photoconductivity, $\Delta\sigma$, is related to the change in dielectric function, $\Delta\epsilon$, upon photoexcitation by $\Delta\sigma = -i\epsilon_0\omega\Delta\epsilon$. Therefore, the measurement of $\Delta\sigma$ for the exciton is equivalent to the polarization response caused by the inter-excitonic transitions. Figure 5.1b reveals sharp lines associated with intra-excitonic transitions (1s$\rightarrow n$p), with the lowest energy peak being associated with the 1s to 2p transition. The oscillator strength of transitions between the 1s and np levels decreases rapidly for increasing n, which results in weaker absorption into higher levels from the ground state (see Section 3.4.4) [81]. As n tends to infinity, the photoconductivity transforms into a pseudo-continuum, and for transition energies above the binding energy, the exciton dissociates into unbound continuum states.

To explore such effects experimentally, the THz photoconductivity spectra of $FAPbI_3$ was measured at 10 K, where stable excitons are able to persist. Figure 5.1c shows these data together with a fit for the exciton resonance, given by a sum of

Lorentz oscillators with resonant energies $E_{1s\text{-}np} = E_X(1 - 1/n^2)$ for transitions between the 1s to np states, and assuming a magnitude proportional to the oscillator strength (see Section 3.4.4 for full details). The use of a recently developed terahertz emitter based on the inverse spin Hall effect [61, 161, 62] here allows for a large spectral bandwidth and therefore clear observation of a resonance near 1 THz, given by the peak in the real part, and a matching zero-crossing in the imaginary part of the photoconductivity. This photoconductivity spectrum of the excitonic resonance in $FAPbI_3$ is broadened, most likely by a combination of lifetime effects, defects in the crystal and interactions with phonons, such that individual transition lines cannot be resolved. From the full fit based on the modelled 1s–np transitions an exciton binding energy of 5.3 meV for $FAPbI_3$ at 10 K is extracted. This value is towards the lower end of the range of values that have been reported for the related $MAPbI_3$ [24], but it is not atypical for a semiconductor of this bandgap energy [162]. The additional modulations in the spectrum at approximately 1 THz and 1.6 THz are attributed to phonon modes that couple to the photoexcited species, as observed previously for $MAPbI_3$ [99], and in agreement with the strong electron-phonon coupling reported for these materials [115].

An unambiguous assignment of the observed resonance to excitons requires us to rule out alternative origins. In principle, there is a reasonable possibility that bulk plasmons could produce a resonance in the photoconductivity spectra when these collective free-charge oscillations interact with the boundaries of their containing medium. The resonant frequency of plasmons is proportional to the square-root of the charge carrier density [163], therefore, the photoconductivity spectra were measured for different excitation fluences corresponding to different initially generated charge-carrier densities (Figure 5.2). No significant shift in the resonant frequency could be discerned as a function of fluence, which verifies that the observed photoconductivity does not originate from a plasmon resonance.

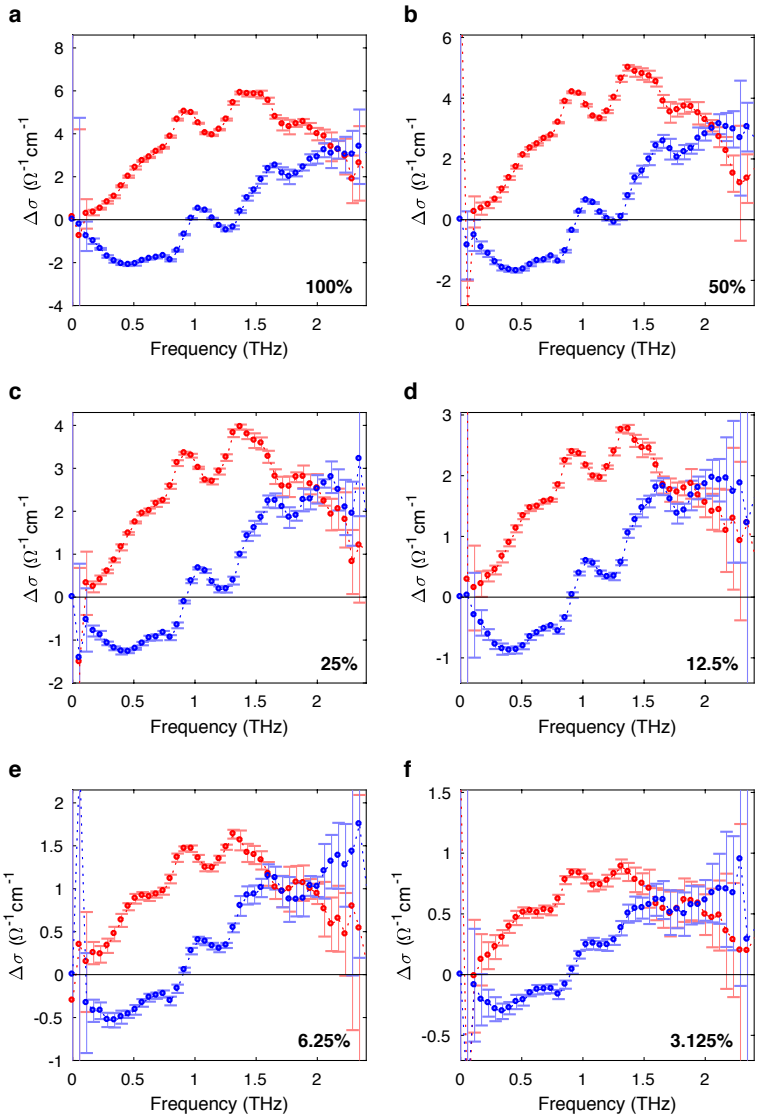


Figure 5.2: Fluence-dependent Photoconductivity of $FAPbI_3$ at 1.7 K. **a-f** Photoconductivity of $FAPbI_3$ measured at a pump power corresponding to 100, 50, 25, 12.5, 6.25, 3.125 percent of the maximum pump power (3 mW), respectively. The photoconductivity was measured using the magneto-OPTPS system as described in the main text with zero magnetic field.

Furthermore, as the temperature is raised to 300 K, the photoconductivity no longer exhibits a resonance within the observation window (Figure 5.1d). The disappearance of the resonance is further proof of an excitonic effect, since excitons are expected to dissociate at thermal energies (300 K≡26 meV) significantly higher than the exciton binding energy. In contrast, a bulk plasmon response would be expected to persist to higher temperatures. Instead, the photoconductivity at 300 K (Figure 5.1d) is found to reflect the Drude response of charge carriers, as observed previously for metal-halide perovskites at room temperature [79, 99]. The Drude model of conductivity applies the principles of kinetic theory to the charge carriers in a material [164, 165]. In contrast with the photoconductivity spectra of excitons, a Drude response is characterised by: (i) a non-zero real component and a zero imaginary component at zero frequency; and (ii) a positive imaginary component maximum at an angular frequency equal to the scattering rate. Therefore, the observed zero imaginary part and constant positive real part across the photoconductivity spectrum derive from a free charge-carrier conductivity response with a scattering rate that lies beyond the measurement bandwidth.

The value of 5.3 meV determined for the low-temperature phase of $FAPbI_3$ is somewhat smaller than that proposed previously from magneto-absorption measurements [166]. However, since such techniques rely on an accurate extrapolation of binding energies to zero magnetic field [166, 167, 168], the low-temperature photoconductivity resonance changes with magnetic field are also explored here. Numerical variational calculations on hydrogenic systems in arbitrary magnetic fields performed by Aldrich and Greene [168] predict a rise in the exciton binding energy with increasing B-field, which has indeed been observed in inorganic semiconductors such as GaAs [75]. Accurate modelling of the magneto-absorption of the exciton is therefore required for the deduction of the exciton binding energy from this method [166, 167, 168], with differences between the theoretical and actual dependence of exciton binding energy

on magnetic field resulting in errors in the estimation of the zero-field exciton binding energy. As a direct measure of how the exciton binding energy of $FAPbI_3$ changes in a moderate magnetic field between 0 T and 7 T, OPTPS is exploited to observe the excitonic resonance energy as a function of magnetic field. Figure 5.1e shows the photoconductivity spectra of $FAPbI_3$ in the presence of a magnetic field of 0 T shown in grey, and 7 T shown in red for the real and blue for the imaginary parts. The spectrum at 7 T is blue shifted with respect to the spectrum at 0 T. Zooming in on the imaginary component at the zero conductivity crossover point near 1 THz, Figure 5.1f demonstrates clearly the increasing resonant frequency for magnetic fields increased in 1 T steps from 0 T to 7 T. The exciton transition energies can be described as a function of the dimensionless parameter $\gamma = \hbar\omega_C/2E_X$ where $\hbar\omega_C$ is the cyclotron energy given by $\omega_C = eB/\mu$ [166]. At 7 T the cyclotron energy is 8 meV and $\gamma = 0.8$, using a value of $0.1m_e$ for the reduced mass. The magnetic field strengths across the range of 0T to 7T therefore fall into a low-to-moderate magnetic field regime, hence the impact of Landau levels has not been considered although could start to have an effect at the upper range of the magnetic fields used. The magnetic field dependent exciton binding energy values presented here are interpreted from using the same model that was used for zero magnetic field and does not include the effects of Landau levels. The inset shows the increase in exciton binding energy deduced from fits based on the modelled 1s–np transitions to the data. While an increase in exciton binding energy with magnetic field is found, the magnitude of the increase is of a significantly smaller extent than calculations would predict [167, 168]. It is therefore suggested that the discrepancy between the theoretically expected and the experimentally observed dependence of the exciton binding energy on the magnetic field is the reason for the elevated exciton binding energy suggested for $FAPbI_3$ from magneto-absorption experiments.

Structural Transitions and Optoelectronic Properties of $FAPbI_3$

One way by which hybrid perovskites differ from classical inorganic semiconductors is by exhibiting a plethora of structural phase transitions at different temperatures. However, while the structural phases of $MAPbI_3$ and their transition temperatures are well established, the picture for $FAPbI_3$ is far less clear [169, 170, 171, 172, 173, 174]. An important starting point for structural calculations is an accurate knowledge of the energy of phonon modes of a material's lattice structure. Therefore the absorption spectra at terahertz frequencies is used to investigate the phonon modes in $FAPbI_3$ as a function of temperature, and contrast the findings with what is observed in $MAPbI_3$.

Table 5.1: Reported crystal phases of $FAPbI_3$ and $MAPbI_3$. While a consensus of the crystal phases of $MAPbI_3$ has been reached, a unified picture of the crystal phases of $FAPbI_3$ is still outstanding. Note† that Chen *et al.* [172] reported different phase transition temperatures for heating and cooling.

	α-phase		β-phase		γ-phase	Ref.
$FAPbI_3$	$P3m1$ Trigonal	$\leftarrow$150 K$\rightarrow$	$P3$ Trigonal	$\leftarrow$100 K$\rightarrow$	-	169
	$Pm\bar{3}m$ Cubic	-	-	-	-	170
	$Pm\bar{3}m$ Cubic	$\leftarrow$285 K$\rightarrow$	$P4/mbm$ Tetragonal	$\leftarrow$140 K$\rightarrow$	$P4/mbm$ Tetragonal	171
	$Pm\bar{3}m$ Cubic	$\leftarrow$290 - 350 K†$\rightarrow$	$P6_3/mmc$ Hexagonal	$\leftarrow$100 - 175 K$\rightarrow$	$P6_3/m$ Hexagonal	172
	$Pm\bar{3}m$ Cubic	$\leftarrow$280 K$\rightarrow$	$P4/mbm$ Tetragonal	$\leftarrow$140 K$\rightarrow$	$P4bm$ Tetragonal	173
$MAPbI_3$	$Pm\bar{3}m$ Cubic	$\leftarrow$327.4 K$\rightarrow$	$I4/mcm$ Tetragonal	$\leftarrow$162.2 K$\rightarrow$	$Pnma$ Orthorhombic	174

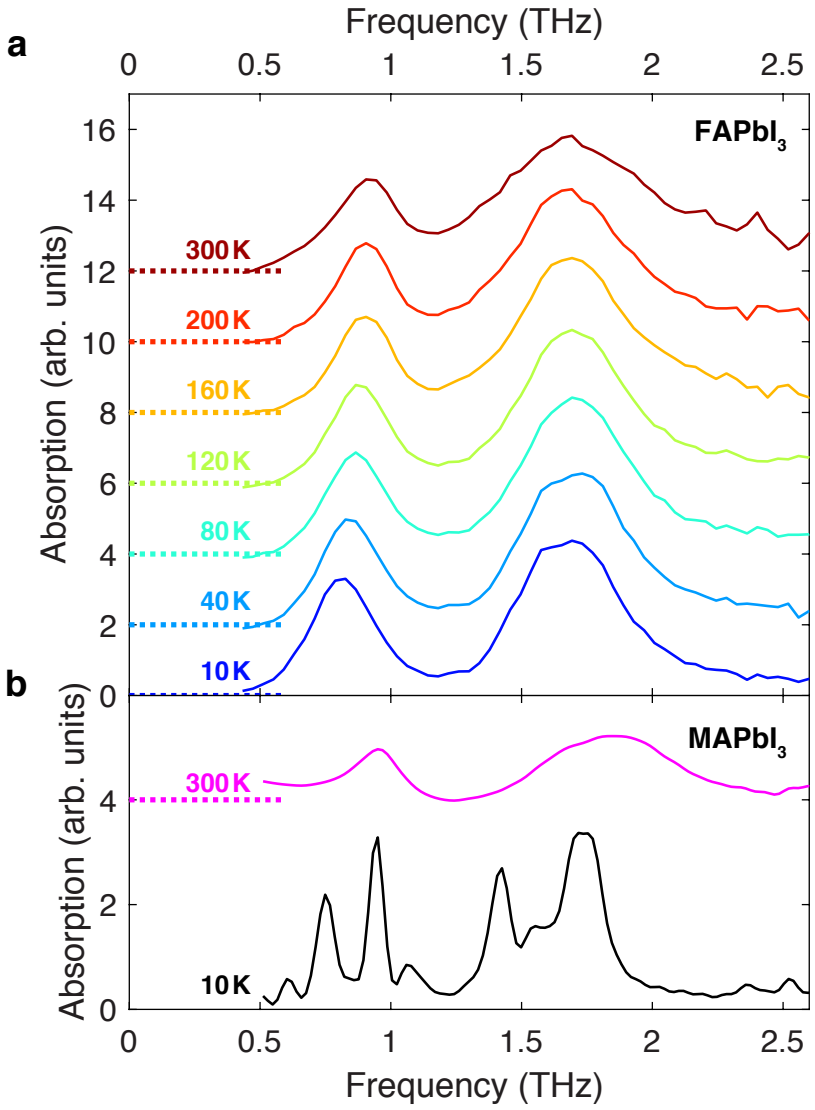


Figure 5.3: Lead-iodide phonon absorption spectra. **a** Absorption spectra of $FAPbI_3$ at terahertz frequencies for different temperatures. The two peaks at approximately 0.8–0.9 and 1.65 THz are attributed to Pb-I vibrations. The dashed lines show the offsets by which each spectrum has been shifted for clarity. **b** Absorption spectra of $MAPbI_3$ at 10 K and 300 K at terahertz frequencies. In contrast to $FAPbI_3$, the lead-halide phonon modes of $MAPbI_3$ split into 4 modes at low temperature [154, 153]. The absorption, α_{Abs} was calculated from the measured transmission, T using the expression $\alpha_{\mathrm{Abs}} = -\ln(|T|)$.

To illustrate the inconsistencies in the literature on the phase transitions between the α, β and γ (high to low-temperature) phases of $FAPbI_3$ Table 5.1 presents details of previously reported structures. The structural phases of $MAPbI_3$ and the transition temperatures are well established, and there is generally good agreement with the parameters shown in the last line of Table 5.1. However, the table highlights a large spread in reported structures for $FAPbI_3$, with some sort of consensus only existing for the cubic high-temperature α-phase. For $FAPbI_3$, the phase transitions between both the α-β and β-γ phases appear to occur over a large temperature region ($> 50\,\mathrm{K}$), which has been attributed to the non-trivial reorganisation of atoms owing to the lack of a group-subgroup relation between space groups of the phases, and also the different temperature-dependent rotational dynamics of the FA cation, compared to the MA cation [172, 171, 175]. Upon the transition from the high-temperature, high-symmetry α-phase to the β-phase, the symmetry is lowered by the introduction of Pb-I octahedra tilting. The transition from the β-phase to the low-temperature γ-phase is accompanied by a freezing of the cations in random orientations [169]. Interchanging the cation between MA and FA therefore has a significant impact on the structural properties of the material. As shown below, such changes may also affect the optical properties, as evident from differences in the phonon modes and optical absorption.

The dark terahertz transmission, T, of a $FAPbI_3$ thin film was measured by terahertz time-domain spectroscopy (see Experimental Details below). Absorption, α_{Abs}, was calculated from the measured transmission using the expression $\alpha_{\mathrm{Abs}} = -\ln(|T|)$. Figure 5.3a reveals two phonon modes at approximately 0.85 THz and 1.65 THz for $FAPbI_3$, which are attributed to vibrations of the Pb-I bonds, in analogy with $MAPbI_3$ [99, 153, 154]. In $FAPbI_3$, these modes are found to be largely unchanged over the temperature range from 10 K to 300 K, despite the up to two phase transitions occurring over that range, i.e. from the low-temperature γ-phase to the β-phase between 100 K and 175 K and potentially on to the α-phase near 290 K [172, 171]. There is

only a small shift in the lowest frequency mode, from 0.8 THz at low temperature, to 0.9 THz at room temperature. In contrast, Figure 5.3b shows the absorption of phonon modes in $MAPbI_3$, which change significantly between 10 K and 300 K, that is, the two high-temperature phonon modes observed in the β-phase split into four phonon modes in the γ-phase [153, 154]. Such differing behaviour can be attributed to the link between the dynamics of the Pb-I octahedra and the orientation of the organic cation [176]. In the two high-temperature phases of $MAPbI_3$ (α and β) both tumbling (rapid reorientation of the C-N axis) and twisting (rotation about the C-N axis) of the MA cation are possible, however only twisting is possible in the γ phase [177, 178]. The low-temperature rotational dynamics of the FA cation have been explored to a much lesser extent. Carignano *et al.* have performed molecular dynamic simulations of $FAPbI_3$, and found that at high temperatures (450 K) FA rotations about the N-N axis and orthogonal to the N-N axis are possible. On lowering the temperature from 450 K to 300 K, the FA cation mobility reduces and rotations are nearly all about the N-N axis [176]. While at lower temperatures the rotational freedom of MA in $MAPbI_3$ is significantly reduced, the FA cation in $FAPbI_3$ appears to be less affected [179]. In addition, FA cations have a larger effective ionic radius than MA cations, which results in $FAPbI_3$ having a larger unit cell than $MAPbI_3$ [170]. In summary, the differences between $FAPbI_3$ and $MAPbI_3$ in terms of the temperature-dependent phonon mode spectra most likely derives from the different dynamics of the FA and MA cations in the lead-iodide cage.

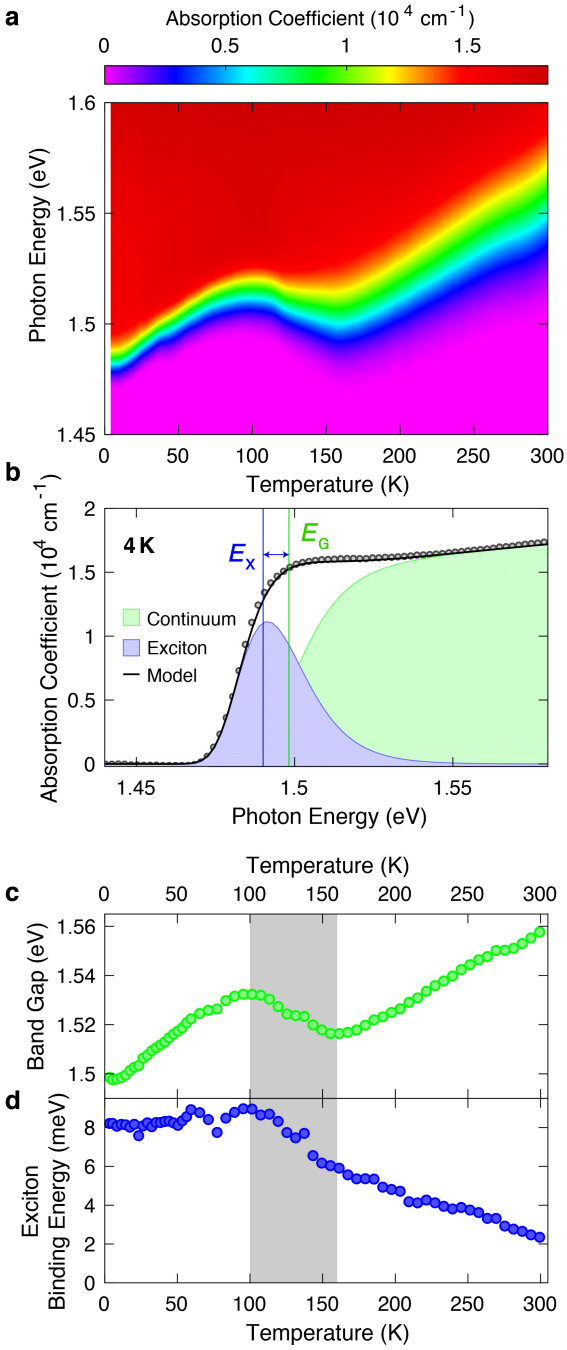


Figure 5.4: Absorption coefficient of $FAPbI_3$ at optical frequencies. **a** Temperature-dependent absorption spectra of $FAPbI_3$ displayed as a two dimensional colour map. **b** Absorption spectrum at 4 K, measured by Fourier transform infrared (FTIR) spectroscopy. Experimental data are shown as grey circles and a fit based on Elliott's theory is shown as a solid black line. Contributions to the absorption coefficient from bound excitonic and continuum states are displayed by shaded blue and green areas, respectively. The vertical green line shows the band gap ebergy, E_G and the difference between blue and green vertical lines is the exciton binding energy, E_X. **c** and **d** show the band gap and exciton binding energy extracted from such fits to the absorption spectra. The grey area displays the region of the observed β–γ phase transition of $FAPbI_3$ between 100 K and 160 K.

5.3.2 Temperature-dependent Absorption Coefficient

The magnitude of the dipole moments carried by the chosen A-cation could potentially influence the polarizability of the perosvkite [180]. Any changes in the dielectric function will have an effect on charge-carrier screening and therefore the exciton binding energy. To observe the effect of structural changes with temperature on the exciton binding and band gap energy, the reflection (R) and transmission (T) spectra of $FAPbI_3$ was measured between 4 K and 300 K, using a Fourier transform infrared spectrometer with the sample mounted in a gas exchange cryostat (see Experimental Details below). Reflection-transmission spectra were converted to absorption coefficient spectra ($\alpha(E)$) using $\alpha = -(1/d)\ \ln(T/(1-R))$, where d is the thickness of the $FAPbI_3$ film.

Figure 5.4a presents the resulting absorption coefficient spectra of $FAPbI_3$ as a two dimensional colour map versus temperature and energy. Outside of the phase transition region between ∼100 K and 160 K, the absorption onset generally blue shifts with increasing temperature in both the high- and low-temperature phases. This general trend in band gap energy with temperature is similar to what has been observed for $MAPbI_3$ [93, 115] but is in contrast with the typical behaviour for III-V inorganic semiconductors, such as GaAs [125].

To extract values for the band gap energy and exciton binding energy, the absorption spectrum has to be modelled to include both electronic transitions between electron-hole continuum and bound excitonic states, as illustrated earlier in Figure 5.1a. Elliott developed a theory on the intensity of optical absorption by excitons [52], which has previously been applied to model the absorption onset for $MAPbI_3$ [26, 120, 112]. Here this theory is applied for $FAPbI_3$ to determine the band gap (Figure 5.4c) and the exciton binding energy (Figure 5.4d) as a function of temperature (see Section 2.1 and Chapter 4 for a full description of the fitting function used). An example fit of Elliott's expression to the absorption onset at one temperature (4 K) is

shown in Figure 5.4b. Unlike for $MAPbI_3$, which at low temperature has been found to exhibit a sharp peak below the gap as a result of absorption into bound excitonic states [26, 120], $FAPbI_3$ only exhibits a much weaker enhancement. The fits of Elliott's expression to the absorption onset show that the lack of a pronounced excitonic peak for $FAPbI_3$ at 4 K is not the result of increased broadening, but rather derives from a low value of the exciton binding energy, in agreement with the low-energy excitonic resonance observed in the OPTP measurements discussed above.

From the dependence of the band gap energy on temperature (Figure 5.4c) one can clearly discern a region between 100 K and 160 K (shaded grey) over which a change from the γ-phase to the β-phase occurs. This transition temperature range agrees well with that deduced from previous XRD measurements [172, 171]. The change in band gap energy at the phase transition observed here for $FAPbI_3$ is markedly different from that previously reported for $MAPbI_3$ [93, 26] which typically displays a sharp discontinuity in band gap of the order of 100 meV. In contrast, the change in bandgap energy between the β and γ phases in $FAPbI_3$ is remarkably smooth, occurring over a wide temperature range (60 K) and only leading to a downshift of $\sim$20 meV with increasing temperature. This contrasting behaviour in terms of bandgap changes at the phase transition of $FAPbI_3$ and $MAPbI_3$ is likely to arise from the difference in molecular dynamics of the organic cations already mentioned above. It has been suggested that for $MAPbI_3$, reorientation of the dipole (tumbling of C-N axis) completely freezes out once the low-temperature γ-phase is entered. However, some degree of dipole reorientation (about the N-N axis) is preserved in $FAPbI_3$ both in the β and γ phases near the transition temperature [175], which will lead to the much more gradual change in optical properties detailed here.

The other parameter obtained from fits of Elliott's theory to the band edge is the exciton binding energy, shown in Figure 5.4d as a function of temperature. In the low temperature γ-phase, the exciton binding energy is approximately constant with a

value near 8 meV. Over the phase transition from the γ to β-phase (beginning at 100 K through to 160 K), a steady decline in the exciton binding energy occurs. The exciton binding energy continues to decrease with increasing temperature throughout the β-phase, reaching a value of 2.4 meV at room temperature. Recently, the exciton binding energy was extracted for $MAPbI_3$ [26] (Chapter 4) through an identical method of Elliott fitting of the absorption onset, and note two main differences with the data reported here for $FAPbI_3$. The first is, that the overall value of the binding energy for $FAPbI_3$ is generally lower by a factor of 2–3 than for $MAPbI_3$ across the temperature range. The second is that while both $FAPbI_3$ and $MAPbI_3$ exhibit a near constant value of the exciton binding energy in the γ-phase, the behaviour around the phase transition is markedly different. For $MAPbI_3$, a sharp decrease in binding energy by approximately 5 meV has been found to occur over a very narrow temperature range [26]. However, here it is observed that there is no sudden discontinuity in the exciton binding energy for $FAPbI_3$ (Figure 5.4d) but rather a gradual decrease over a broad temperature range. The absence of discontinuities in the band gap and exciton in $FAPbI_3$ and the presence of discontinuities in $MAPbI_3$ suggests a different nature of the phase transition, and is attributed to differences in the dynamics and structural influence of the FA and MA cations on $FAPbI_3$ and $MAPbI_3$, respectively. These observations for the exciton binding energy are in agreement with temperature-dependent measurements of the dielectric permittivity of $FAPbI_3$, which was found to change smoothly across the phase transition [171]. The inherent dependence of the exciton binding energy on the inverse of the square of the dielectric permittivity [24] is therefore reflected in the differences in the nature of the phase transition, and the associated changes in polarizability of the material.

The value extracted for the exciton binding energy at low temperature is slightly higher for the Elliott approach compared with that determined from terahertz spectroscopy (OPTP). These slight discrepancies may arise from the difficulties in ob-

taining a satisfactory fit of Elliott's theory to the absorption onset over a sufficiently wide energy range [26, 112]. As shown recently (Chapter 4), Elliott's theory does not account for the possible presence of multiple electronic transitions, non-parabolic bands and an energy dependence of the associated matrix elements [26]. As a result, the shape of the free (uncorrelated) continuum-state absorption may deviate from the square-root dependence on energy above the gap. As discussed in more detail below, for $FAPbI_3$, these deviations seem to cause a slight up-shift in the value of the exciton binding energy extracted from the Elliott approach.

Here, the disparity between the exciton binding energy measured from OPTPS (5.3 meV at 10 K) and the exciton binding energy extracted from absorption spectra modelling ($\sim$ 8 meV at 10 K) is addressed. Figure 5.5 shows the absorption data and absorption model using the fitted exciton binding energy, E_X, and also $E_X \pm 3$ meV. The band gap was shifted by the same energy as the exciton binding energy, such that the energy of the 1s state was unchanged, and hence all models had the same absorption onset energy. The model was normalised to the data at an energy above the band gap shown by the intersection of the three lines in each plot. Larger exciton binding energies give a more pronounced exciton peak and a flatter absorption spectrum above the band gap. The model gives a concave function above the band gap for all values of exciton binding energies. However, the opposite is true for the measured absorption spectra, which produces a convex function above the band gap. The contrasting curvature of Elliott theory and absorption spectra at energies greater than 100 meV above the band gap for $FAPbI_3$ could be the cause of the difference in measurement of the exciton binding energy between OPTPS and absorption spectra.

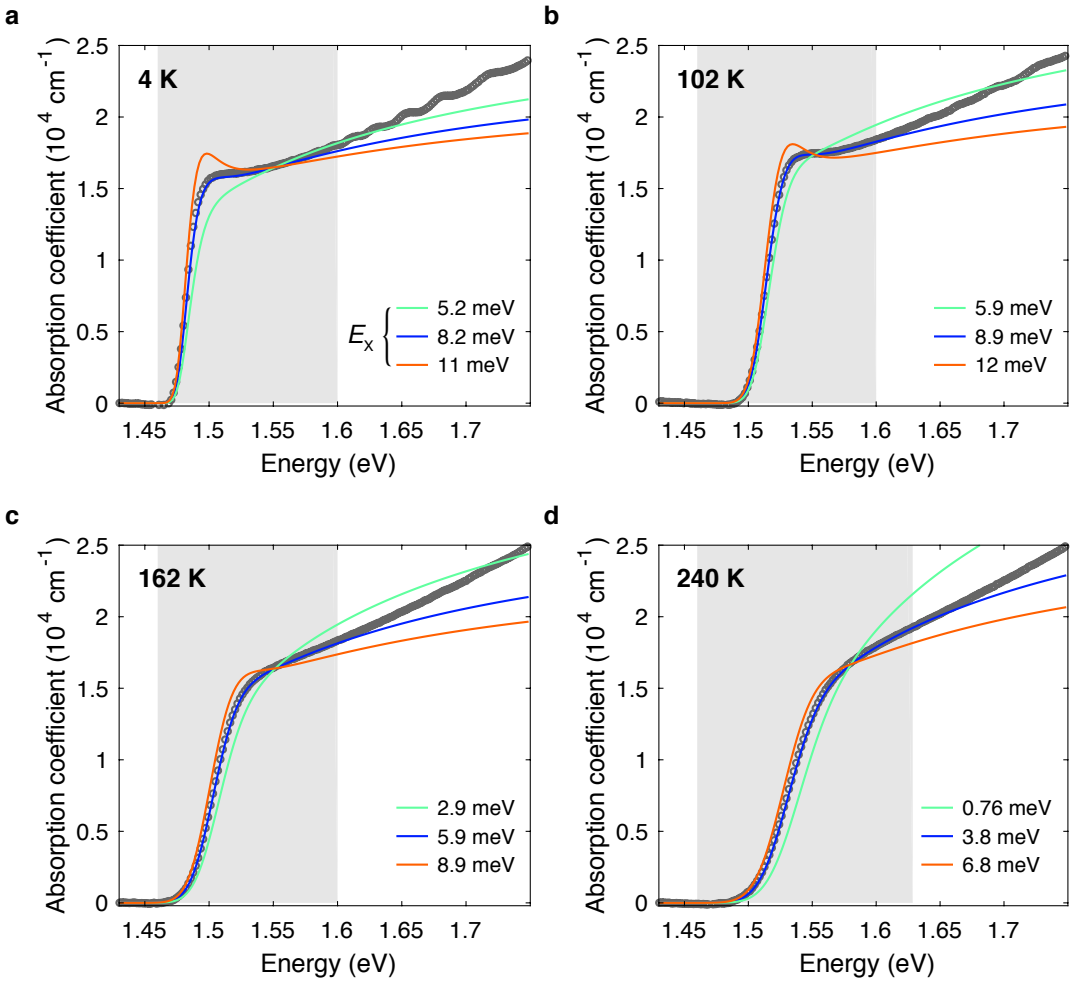


Figure 5.5: Absorption modelling of $FAPbI_3$. **a-d** Absorption coefficient at 4 K, 102 K, 162 K and 240 K. The grey area shows the data used to model the absorption. The blue line shows the fit to the data. The green and orange lines show fits with the exciton binding energy adjusted by ±3 meV. The band gap was adjusted by the same amount such that the 1s state of the exciton is at the same energy for all three fits (blue, green orange).

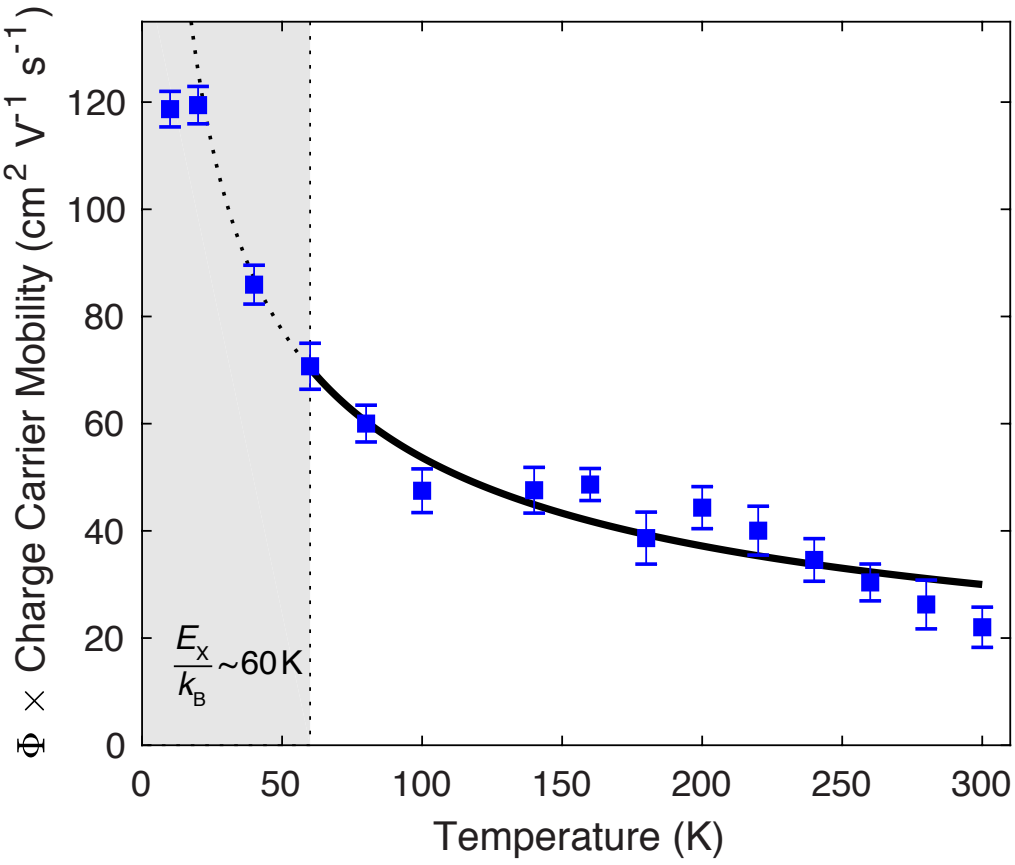


Figure 5.6: Effective charge carrier mobility $\Psi\mu$ as a function of temperature for a thin film of $FAPbI_3$. Here, μ is the charge-carrier mobility, and Ψ the photon-to-free-charge branching ratio, which is expected to decrease from a high-temperature value of 1 when the temperature is lowered below the value of $E_X/k_b \sim 60\,K$ and excitons become thermally stable. The solid line shows a fit of $\mu \propto T^w$ to the data for temperatures 60 K and above. A power-law behaviour with an exponent of $w = -0.53$ is found, in agreement with predictions [158] based on charge-carrier interactions with polar optical-phonons [115].

5.3.3 Charge Carrier Mobility in $FAPbI_3$

Another electronic parameter that underpins the operation of solar cells is the charge-carrier mobility. For charge carriers to be extracted in a photovoltaic device, charge mobilities need to be sufficiently high such that within the carrier lifetime the charges are able to reach the electron and hole transport layers [25]. Terahertz photoconductivity measurements are an excellent choice for studying the charge carrier mobility of a material as the method does not rely on electrical contacts that would otherwise complicate the measurement.

The mechanisms limiting the mobility of charge-carriers in metal halide perovskites are a subject of much current debate. While some hybrid perovskites can still show dependences on extrinsic factors, such as electron scattering off grain bourdaries and defects, it has recently been argued that high-performing materials such as $MAPbI_3$ and $FAPbI_3$ are nearing the limit of what is intrinsically achievable [20]. An analysis of the temperature-dependent emission line broadening in $MAPbI_3$ and $FAPbI_3$ [115] further revealed that Fröhlich interactions between charge-carriers and longitudinal optical (LO) phonons are the dominant intrinsic mechanism limiting charge-carrier motion. Such a mechanism qualitatively agrees with the strong increase observed in the charge-carrier mobility of $MAPbI_3$ as the temperature is lowered [93, 148, 124, 160]. However, such measurements have consistently yielded [93, 148, 124, 160] a dependence of the charge-carrier mobility μ on temperature T according to $\mu \propto T^w$ with $w = -1.5$. This experimentally determined value of the exponent w for $MAPbI_3$ does not agree with the value of ~ -0.5 proposed recently [158] as a suitable high-temperature approximation to the charge-carrier mobility expected according to Hellwarth and Biaggio [181] when Fröhlich interactions dominate.

To assess whether such discrepancies also manifest themselves in $FAPbI_3$, OPTP was used to measure the effective charge carrier mobility as a function of temperature for $FAPbI_3$ (see Chapter 3 and Section 5.2 for experimental details). Figure 5.6 shows

the resulting data together with a best fit to $\mu \propto T^w$ over the temperature-range 60–300 K, which yields a value of $w = -0.53$, very close to what would theoretically be expected for $MAPbI_3$ when subject to Fröhlich interactions [158]. This fit excluded data points below 60 K, as excitonic effects may become more dominant here ($k_b \times 60\,\mathrm{K} \leq 5.3\,\mathrm{meV}$) and hence measurements of the effective charge-carrier mobility no longer fully reflect the values of the charge carrier mobility in the material. To reflect this, the dashed line is extrapolated from the fit, at temperatures below 60 K.

A review by Herz [20] discusses the physical origin of the power law with exponent of -1.5 for $MAPbI_3$. An over simplified model derived for non-interacting phonon modes follows a $T^{-1.5}$ temperature dependence for acoustic-phonon deformation potential scattering, however this is not an applicable model for the case of metal halide perovskites. An article by Wright et al. which examines the line width broadening of the photoluminescence determines that Fröhlich interactions are the dominant scattering mechanism at room temperature. Along with the article by Davies et al. [182], the following paragraph discusses the possible origin of the discrepencies of the temperature dependent power laws.

Our results thus reveal that the discrepancy between the theoretically expected and experimentally determined temperature-dependence of the charge-carrier mobility for $MAPbI_3$ is not a universal feature of lead-iodide perovskites. For $FAPbI_3$, excellent agreement with the dependence expected for halide perovskites is obtained, suggesting that a Fröhlich picture of charge-carrier interactions with phonons is fully appropriate. While the reasons for the discrepancy between theory and experiments observed in $MAPbI_3$ cannot be conclusively determined here, they may lie in issues with phase retention observed in $MAPbI_3$. Experiments have repeatedly shown that thin films of $MAPbI_3$ may have remnant domains that contain regions of different crystallographic structure [23]. For example, additional photoluminescence features in the low-temperature orthorhombic phase below 160 K have been attributed to the

presence of remnant tetragonal domains over a relatively large temperature range [23]. Such regions could represent barriers to charge-carrier motion, whose prevalence depends on the material temperature, leading to a deviation from the intrinsic behaviour expected from Fröhlich interactions alone. For $FAPbI_3$, on the other hand, such minority-phase inclusions have been shown to be absent [115], and hence the expected [181, 158] temperature-dependence of $\mu \propto T^{-0.5}$ is indeed observed.

5.4 Summary

In conclusion, the temperature dependent studies of $FAPbI_3$ have revealed significant differences in the optoelectronic properties in comparison with $MAPbI_3$. Intra-excitonic transitions were directly observed in $FAPbI_3$ from which the exciton binding energy was determined to be 5.3 meV at 10 K, which is at the low end of the spectrum of reported values for $MAPbI_3$. Further, this chapter examined how parameters critical to the operation of photovoltaic cells, such as the exciton binding energy, band gap, vibrational properties and charge-carrier mobilities vary with temperature and across phase transitions. In contrast to $MAPbI_3$, the band gap and exciton binding energy varies smoothly over a range of 100–160 K at the β to γ phase transition in $FAPbI_3$. Such absence of clear discontinuities for $FAPbI_3$ most likely results from the rotational freedom of the FA dipole moment being reduced only gradually upon entry into the γ phase, whereas in $MAPbI_3$, MA dipole rotation is frozen out abruptly over a narrow temperature range. This chapter also demonstrated that such structural changes manifest themselves in the IR phonon signatures associated with the lead-halide sublattice vibrations. The two phonon modes observed in the β phase are largely unchanged for $FAPbI_3$ upon entry into the γ phase, while for $MAPbI_3$, a splitting into four phonon modes is observed. Finally, the charge-carrier mobility in $FAPbI_3$ was revealed to exhibit a clear $T^{-0.5}$ trend with temperature, in excellent

agreement with theoretical predictions for halide perovskites whose electron-phonon interactions are governed by the Fröhlich mechanism, but in contrast to the $T^{-1.5}$ dependence previously observed for $MAPbI_3$. The contrasting temperature-dependent behaviour of excitons, phonons, electronic transitions and charge-carrier mobilities in $MAPbI_3$ and $FAPbI_3$ highlight the impact of cation substitution not only on the structure of the perovskite but also on its optoelectronic properties.

Chapter 6

Low Disorder GaAs-AlGaAs Quantum Well Tube Nanowires Investigated by Single Nanowire Photoluminescence

Semiconductor nanowires have received much attention over the past decade owing to their potential use in electronic and optoelectronic devices. Already many nanowire based devices have been demonstrated, including solar cells [34, 35], terahertz detectors [36, 37, 38], field effect transistors [39, 40], electrical detection of cancer markers [183], and LED-based devices [41, 42]. Customisation of the band gap is essential for such nanowire applications. While adjusting the alloy fraction of *ternary* materials such as $Al_xGa_{1-x}As$ is traditionally used to tailor the band gap of semiconductors, tuning the nanowire band gaps across the full visible region has proved challenging [184]. An alternative method for tailoring the band gap energy is to take advantage of quantum effects: by growing a thin layer of lwower band gap material within the higher band gap shell layer, a "quantum well tube" (QWT), or "radial quantum well",

along the nanowire axis can be produced.

Core-multishell nanowires have previously been fabricated in a range of material systems from nitride [185], phosphide [186], and arsenide [187] based III-Vs, to silicon [188, 189, 190]. Furthermore, they have already been implemented in a range of opto-electronic devices [191, 192, 193, 194, 195]. Small changes in the width of the QWT shell layers result in large changes in the confinement energy with an associated significant impact on the emitted spectrum. Control of the size of the core and shell layers, as well as the intra-wire energetic disorder in each layer, is therefore crucial to the development of nanowire-based devices. In order to achieve good repeatability needed for large-scale device manufacturing, it is important to understand the underlying mechanisms causing inter-nanowire variations. For commercial applications, characterisation of nanowires at room temperature is highly desirable. Previous studies have been carried out at low temperature to characterise single QWTs [196, 49, 197], unfortunately room temperature measurements have, until now, remained challenging owing to quenching and broadening effects in the photoluminescence (PL) emission spectrum.

In this chapter, PL spectra on 150 single GaAs/$Al_{0.4}Ga_{0.6}As$ core-multishell nanowires are analysed to investigate the statistical distributions of the structural and optical properties that result from growing a thin GaAs shell layer (QWT) between two thicker $Al_{0.4}Ga_{0.6}As$ shell layers. Charge carriers in the QWT are observed to be confined in one dimension, resulting in a blue shift of the allowed transitions associated with PL emission ($\Delta E = 0.1$ - $0.3\,\mathrm{eV}$). A simple one-dimensional (1D) finite well model for the QWT is implemented to obtain an estimate of the well width. Furthermore, statistics have been collected on 150 nanowires from 3 different samples and used to examine the intra-sample and inter-sample variations in nanowire thicknesses and defects. Low disorders for both the core and QWT are reported and correlations between the two disorders and their structure are

discussed. Two-dimensional (2D) numerical simulations have also been performed to investigate the effect of introducing geometric distortions and disorder on the optical and electronic properties of nanowires.

6.1 Method

6.1.1 Growth Method

Core-multishell GaAs/$Al_{0.4}Ga_{0.6}As$ QWT nanowires have been grown by metalorganic chemical vapor deposition with various QWT widths in order to investigate energetic disorder. Trimethylgallium (TMGa), trimethylaluminium (TMAl), and arsine (AsH_3) were used for the source of Ga, Al, and As, respectively. First, GaAs nanowires were grown on GaAs (111)B substrates by a two-temperature procedure [44] using Au nanoparticles with a diameter of, 50 nm, 100 nm and 100 nm, as the catalysts of samples that are labelled, B50, B100 and C100, respectively. After the 50 nm (100 nm) core growth, the growth temperature was increased to 750°C and then a 23 nm (46 nm) AlGaAs layer was deposited surrounding the core, followed by the GaAs QWT growth by switching off TMAl. The thicknesses of GaAs QWTs were controlled by the growth time, which was 30 and 15 seconds for samples B and C respectively. This resulted in QWT thicknesses of approximately, 1.5 nm, 3 nm and 2 nm, for the three samples respectively. The GaAs QWT was then enclosed in another AlGaAs layer with thickness 16 nm (32 nm). As a result, a GaAs QWT sandwiched between two AlGaAs layers was obtained in the nanowire. Finally, a thin layer of GaAs was deposited as a capping layer to prevent the oxidation of Al in the AlGaAs shell. The aluminium concentration has been determined previously to be 0.40±0.06 in the AlGaAs barriers [196]. This was measured by aberration-corrected high-angle annular dark field scanning transmission electron microscopy images taken on nanowires grown by the same method. The error bars represent

the variation of aluminium concentration in individual nanowires (i.e. the intrawire aluminium concentration variation). After growth, the nanowires were transferred from their growth wafers to quartz substrates by rubbing.

6.1.2 Experimental Details

Time-integrated PL measurements were performed at room temperature using a custom-built microscope and is detailed in Section 3.1.1. The PL was observed to be strongest at the ends of the nanowires as a result of waveguiding [198, 199, 200]. PL from the QWT is sensitive to the position of the incident light on the nanowire [201] and measurements are taken at a position where the emissions from the core and QWT are approximately of the same order of intensity.

6.2 Results and Discussion

A schematic diagram of the band structure of one of the QWT nanowires is displayed in Figure 6.1a, with the transition energies from the core and the quantum well tube indicated. A typical spectrum is shown in Figure 6.1b, with the peak of the QWT shifted higher in energy owing to confinement. This confinement in nanowire heterostructures has been documented previously at low temperature [196, 49, 197] with some studies of axial heterostructures reporting this effect at room temperatures [202]. Here this effect is demonstrated at room temperature for radial heterostructures; and more importantly, using measurements taken on single nanowires.

6.2.1 Model

The carrier lifetime for GaAs/$Al_{0.4}Ga_{0.6}As$ core-shell nanowires grown using the two-temperature technique [44] is of the order of nanoseconds [203]. Following pulsed excitation, photo-injected electrons and holes rapidly establish a thermal distribution

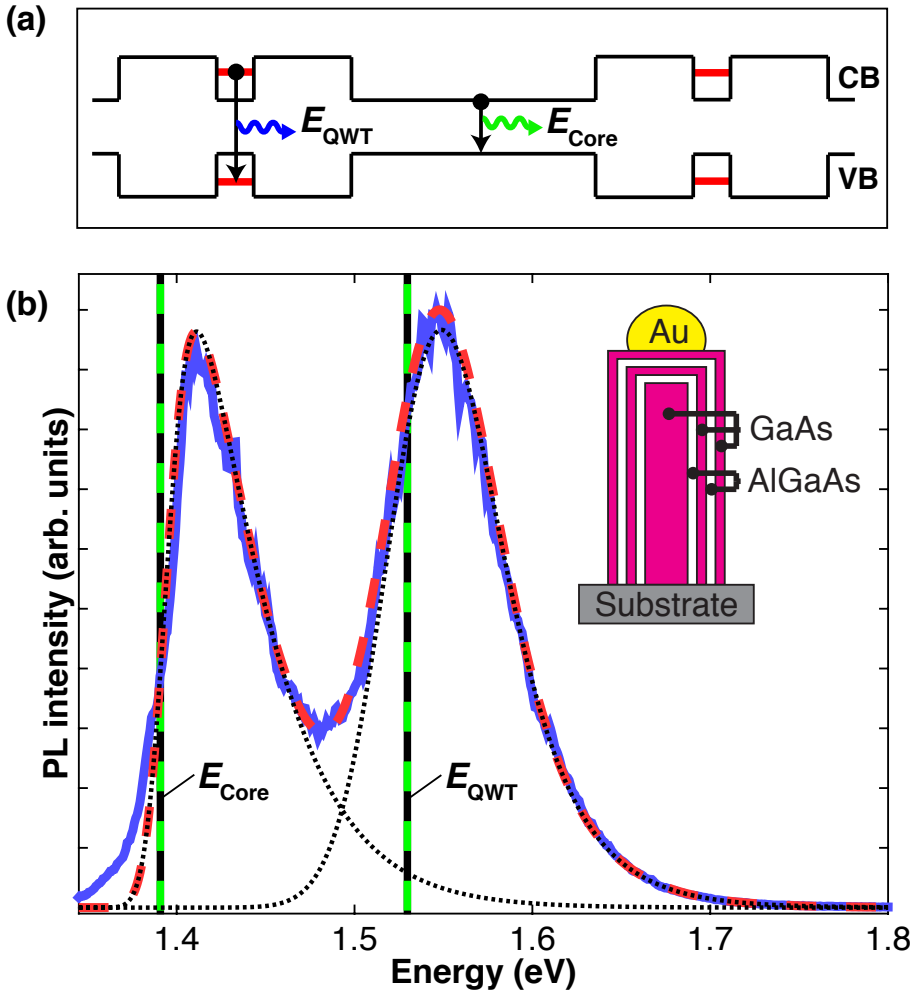


Figure 6.1: **a** Schematic of the band structure of a nanowire taken along a line perpendicular to and intersecting the nanowire axis. The black lines show the conduction band (CB) and the valence band (VB), with black arrows depicting the electronic transitions from the core and the QWT with emission energies E_{Core} and E_{QWT} respectively. The horizontal red lines show the ground state energies, which are shifted with respect to the bulk values owing to quantum confinement. The nanowire is composed of: a GaAs core; two $Al_{0.4}Ga_{0.6}As$ shell barrier layers with a GaAs QWT in-between; and a GaAs capping layer. **b** A PL spectrum from a typical nanowire from sample B100 (shown on a linear scale). Experimental data is shown as a blue solid line, the model as a red dashed line, and the core and QWT components of the model as black dashed lines. The two green dashed lines show the energy gap of the core and the QWT. The inset shows a schematic of the nanowire showing the GaAs core, QWT and cap, and the $Al_{0.4}Ga_{0.6}As$ shell barrier layers.

near the conduction and valence band edges [204]. As excitonic effects are weak at room temperature in GaAs [205, 206], the PL spectrum of each nanowire is assumed to be dominated by band-to-band recombination in both the core and QWT. To a first approximation, the emission energy spectrum in a 3D semiconductor is proportional to a Fermi-Dirac distribution multiplied by the density of states. At room temperature, thermal energies are large enough that this Fermi-Dirac distribution can be approximated using the classical limit to a Boltzmann distribution, with an energy-offset equal to the band gap energy, multiplied by the joint density of states for the electrons and holes. This approximated distribution can then be used to model the expected emission peak from the core and the QWT respectively. The core has a three-dimensional (3D) density of states (DoS), as the width is large enough such that quantum confinement effects are insignificant [207]. Hence, for the core with band gap, E_{Core}, a Maxwell-Boltzmann distribution is fitted

$$B_{\mathrm{Core}}(E) \propto \sqrt{E - E_{\mathrm{Core}}} \exp\left(-\frac{E - E_{\mathrm{Core}}}{k_{\mathrm{B}}T}\right) , \tag{6.1}$$

where E is the energy of the photons measured from the PL, T is the electron temperature and k_{B} is the Boltzmann constant. In contrast, since the QWT is confined in one-direction and hence possesses a two-dimensional DoS, a 2D modified version of the Maxwell-Boltzmann distribution is used [208, 209],

$$B_{\mathrm{QWT}}(E) \propto \exp\left(-\frac{E - E_{\mathrm{QWT}}^{\mathrm{e_1 \rightarrow hh_1}}}{k_{\mathrm{B}}T}\right) , \tag{6.2}$$

where the energy gap between the lowest electron ($\mathrm{e_1}$) and hole ($\mathrm{hh_1}$) states in the quantum well is $E_{\mathrm{QWT}}^{\mathrm{e_1 \rightarrow hh_1}}$. The nanowires, however, do not have a perfect structure and so the spectral peaks are broadened by defects and disorder. In order to parameterise

disorder, a Gaussian distribution is introduced

$$G_j(E) = \exp\left(-\frac{E^2}{2\sigma_j^2}\right) , \tag{6.3}$$

to model *non-thermal* broadening. Here the subscript j denotes either the distribution for the QWT or the core. The disorder parameter σ_j is related to the full-width-at-half-maximum (FWHM$_j$=$2\sigma_j\sqrt{2\ln 2}$) of the PL spectrum in the absence of thermal broadening (i.e. in the limit $T \to 0$). The intensity of each peak is therefore proportional to the convolution of $G(E)$ and $B(E)$. Hence, the intensity of measured PL, $I(E)$, is modelled as a linear combination of the core and QWT intensities,

$$I(E) \propto G_{\mathrm{Core}} \otimes B_{\mathrm{Core}} + G_{\mathrm{QWT}} \otimes B_{\mathrm{QWT}} . \tag{6.4}$$

From this model, the following parameters could then be determined: the emission energy of the core (E_{Core}) and QWT ($E_{\mathrm{QWT}}^{\mathrm{e_1 \to hh_1}}$); the disorder parameter of the core (σ_{Core}) and QWT (σ_{QWT}); and the electron temperature (T). The electron temperature extracted from fits to the data (average: $360 \pm 60\,\mathrm{K}$) is significantly above the lattice temperature (290 K) as expected [210, 211]. Finally, a finite well model is used to extract the well width for the QWT. While excited charge carriers do relax to lower energy states, a significant number of charge carriers is observed to have larger energies than the energetic disorder parameter. These carriers can occupy states in thinner sections of the QWT and therefore all parts of the QWT are able to be probed and not just the thicker sections.

6.2.2 Single Nanowire Photoluminescence and Statistical Correlations

The PL spectrum of a typical single nanowire from sample B100 is shown in Figure 6.1b. The spectrum is composed of two broad peaks; the peak at 1.42 eV is the emission from the GaAs core and the peak at 1.55 eV is attributed to a blue shift in the $e_1 \rightarrow hh_1$ transition in the GaAs QWT layer owing to quantum confinement. The red dashed line in Figure 6.1b is a fit of Equation 6.4 to the measured PL spectrum. The fit accurately reproduces both the core and QWT emission peaks, with only a minor discrepancy in the low energy tails (¡1.4 eV). These low energy tails probably arise from defect level recombination, aluminium-induced red shifts [212], or residual strain [213], and have been reported previously for bulk samples [214].

The fitted values for the band gap energy and QWT transition energy are E_{Core} = 1.39 eV and $E_{\mathrm{QWT}}^{\mathrm{e_1 \rightarrow hh_1}}$ = 1.53 eV respectively, and are indicated by the two green dashed lines in Figure 6.1b. The fact that these values differ from the peak energies in the PL spectrum by ∼30 meV highlights the importance of properly modelling PL spectra from nanowires. In this case the value of the experimentally observed peaks are shifted from the true transition energies as a result of two factors: (i) asymmetric thermal broadening [215, 206] and (ii) the fact the PL emission from the QWT and core overlap spectrally. Both these effects are accounted for in Equation 6.4. For example by changing photo-excitation conditions the relative intensities of the two spectrally overlapping PL peaks change. Despite changes in the PL peak positions, the model reveals the same transition energies E_{Core} and $E_{\mathrm{QWT}}^{\mathrm{e_1 \rightarrow hh_1}}$, irrespective of such changes in relative PL intensity.

Measurements of the well width are calculated using the finite well model and are presented in a histogram plot in Figure 6.2. The average widths are 2.1, 4.0 and 2.0 nm, for samples B50, B100 and C100, respectively. The main source of error in the calculated quantum well widths is from the uncertainty in the fitting of the energy

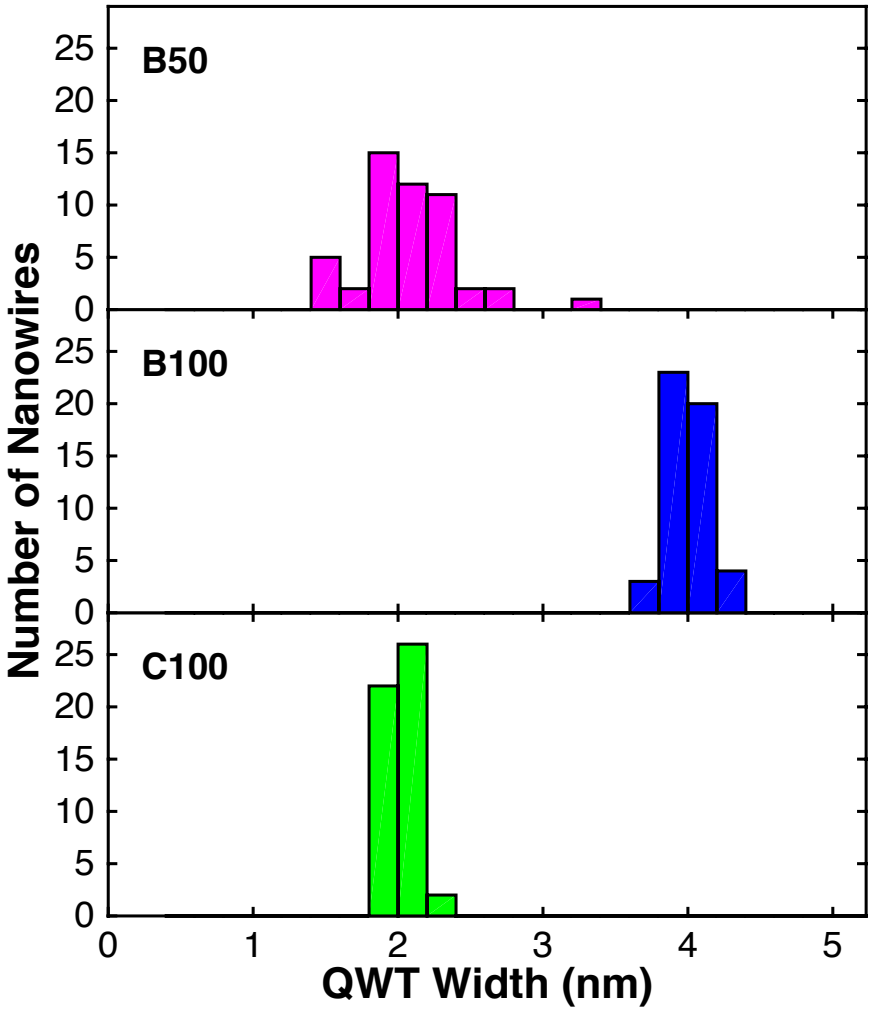


Figure 6.2: A histogram of all nanowires measured showing the occurrence of the QWT widths in each sample, as measured using the modelled PL spectra. The average widths are 2.1, 4.0 and 2.0 nm, for samples B50, B100 and C100, respectively.

of the core and QWT emission peaks. The lattice spacing of the {220} atomic planes has previously been measured to be 0.2 nm [203]. The standard deviation of the QWT width of each sample is measured to be 0.32, 0.14 and 0.10 nm. Hence, these results provide evidence of the inter-wire uniformity and consistency of the QWT layer growth, which is promising for scaling the production of nanowires.

The disorder parameter extracted encompasses all possible energetic sources of disorders in the system. Here, these contributing factors are discussed. The nanowires are determined to be twin free [203, 216, 217], so structural defects are considered to

be negligible. The main factors contributing to the disorder are width fluctuations and variations in Al alloy fraction. Both of these factors affect the degree of confinement felt by charge carriers in the QWT and therefore the energy of emission on relaxation of these charge carriers. The width of the GaAs layer between the AlGaAs barrier layers defines the width of the well and the Al concentration defines the barrier height. The contribution of Al concentration fluctuations to the disorder is estimated to be 68, 34 and 74 percent of the total value for samples B50, B100 and C100, respectively with further detail given in Figure 6.4 and Table 6.1. Figure 6.4 demonstrates the effect of aluminium concentration variations on the energetic disorder of each nanowire and shows the range of energy shifts expect for the QWT for an aluminium concentration of 0.40 ± 0.06.

Sample	Width (nm)	σ (meV)	ΔQ (meV)	$\Delta Q/\sigma$
B50	2.1	39	26.7	0.68
B100	4.0	26	8.8	0.34
C100	2.0	39	28.7	0.74

Table 6.1: Contribution of aluminium variations to the disorder parameter, σ. The difference in quantum well energy level ΔQ for aluminium concentrations 0.34 and 0.46 are calculated for the determined well widths of each sample. The energy difference ΔQ is divided by the extracted disorder parameter, σ to determine an estimate for the possible contribution of aluminium fluctuations to the disorder.

Using the calculated well widths, a relationship between both the energy peak and QWT width with the disorder parameter is observed, as shown in Figure 6.3a. The larger well widths are correlated with smaller disorder parameters. Notably, sample B100 has both a significantly larger well width than the other two samples as well as a much smaller disorder parameter. This correlation is expected since variations in the width of a larger well will have less of an effect on the energy shift owing to confinement, than variations in width for a smaller well, as discussed later. As observed, averaging this effect over the whole nanowire will give broader emission lines for smaller quantum wells; samples B50 and C100 have larger QWT disorders than B100. Based on the optical measurements, the average width of the QWT of

sample B100 is 2.0 times that of sample C100, which is consistent with the growth durations for the QWT in these samples.

Figure 6.3 also highlights the importance of taking single nanowire measurements, as for sample B50, the inter-wire standard deviation of the QWT energy gap is approximately 60 meV, which is greater than the disorder of a single nanowire (∼40 meV). This spread in QWT energy gap would have presented itself as a larger disorder had ensemble PL measurements been taken, emphasising the value of single nanowire measurements. It is important to note that both the core and the QWT have low disorder on the order of $k_{\mathrm{B}}T$, showing great promise for use in optoelectronic devices. However, efforts to reduce the disorder are often restricted by the FWHM of the emission spectrum being dominated by thermal broadening [218]. Figure 6.3b shows a correlation between the core disorder parameter and the QWT disorder parameter. It is possible that if the core has poor morphology this could be propagated through to the QWT having poor morphology. This gives incentive to produce nanowires with the best core quality possible, even if only the shell layers of the nanowire are the functional elements. Figure 6.3b also shows that the disorder of the quantum well, σ_{QWT}, is consistently larger than the disorder of the core, σ_{Core}, with a ratio of σ_{QWT} to σ_{Core} of 3.9, 6 and 4.1, for samples B50, B100 and C100, respectively. The larger disorder in the quantum well can be attributed to a few factors. Firstly, the much larger surface area to volume ratio of the QWT has an effect. The QWT layer has two boundaries with the $Al_{0.4}Ga_{0.6}As$ barrier layers and is much thinner than the core and is therefore likely to have a higher number of surface states and defects in a given volume. The ratio of the surface area to volume ratio of the quantum well tube to that of the core is 36, 29 and 70, for samples B50, B100 and C100, respectively (see Section 2.3.4). Secondly, the spectra is also broadened by different shifts in the QWT energy gap due to varying thicknesses of the QWT in the nanowire. This is confirmed by transmission electron microscope (TEM) images shown in Figure 6.5 and previ-

ous measurements, which show fluctuations of the QWT width around the nanowire [216, 219]. Figure 6.5a corresponds to a low magnification bright field TEM image of a representative cross-section of sample B50. The thickness of the GaAs quantum well is measured in different regions with variations in thickness being found with a thickness of 4 nm in the edges and 2 nm in the facets. Figure 6.5b is a high resolution TEM image taken taken along the nanowire cross section near the corner of the quantum well. The quantum well is highlighted by white dashed lines and the variation in quantum well thickness between the edge and the facets is clearly visible. Figure 6.5c and d are additional TEM images of sample B50 taken from the top and bottom of a nanowire. These images further demonstrate the inhomogeneity of well width around a nanowire.

6.2.3 Simulations

To further investigate the microscopic origin of the disorder, simulations were performed using a Schrödinger-Poisson solver for semiconductors [220]. From these simulations, the band structure and PL are modelled and then compared with experiment. Simulation results for a defect-free nanowire, with a 50 nm core and a QWT width of 4 nm, are presented in Figure 6.6. Charge carriers are generated uniformly in the nanowire, with the lattice temperature set to room temperature, and simulations are calculated for a stationary state. Figure 6.6a shows the band structure and charge carrier density taken along a line perpendicular to the nanowire axis. The distribution of electrons and holes in the nanowire heterostructure are influenced by band bending, as a result of Fermi level pinning at the surface; fewer holes than electrons are present in the core, which are accounted for by an excess of electrons in the QWT. The calculated electron (hole) density over a nanowire cross-section is displayed in the left (right) of Figure 6.6b. From the numerical calculations, values for eigenenergies E_{e} and E_{h}, and the occupancy of electrons and holes, n_{e} and n_{h}, in these states are

obtained. Using Fermi's golden rule [221, 222], an approximate emission spectrum, $I(E)$, can be calculated given by

$$I(E) \propto \sum_{E_\mathrm{e}} \sum_{E_\mathrm{h}} n_\mathrm{e}(E_\mathrm{e})\, n_\mathrm{h}(E_\mathrm{h})\, \delta(E - (E_\mathrm{e} - E_\mathrm{h}))\, |\langle \phi_\mathrm{e} | \phi_\mathrm{h} \rangle|^2 \ , \tag{6.5}$$

where $\left|\phi_{\mathrm{e(h)}}\right\rangle$ is the envelope eigenstate of electrons (holes) of energy eigenvalue E_e (E_h). The simulated PL for nanowires with QWT widths ranging from 1.5 nm to 4 nm is presented in Figure 6.7a, showing the expected blue shift with reducing QWT width. This blue shift in simulated PL is compared with a simple 1-D model of a quantum well in the inset of Figure 6.7a. Excellent agreement is observed between the full 2D simulation results (black crosses) and the 1D analytical model (red line), indicating the validity of the simpler approach used to generate the results shown in Figure 6.2. According to the 2D simulation, only one confined subband in the conduction band of the QWT is possible, leading to a dominant $\mathrm{e}_1 \rightarrow \mathrm{hh}_1$ QWT transition, which is in good agreement with experimental results (e.g. Figure 6.1). The very small peak at 1.9 eV for the 1.5 nm QWT is due to a $\mathrm{e}_1 \rightarrow \mathrm{lh}_1$ transition; this is not observed in the experimental results, possibly due to broadening affects.

The effect of variation of the QWT width on nanowire facet is now considered and related to the broadening of single nanowire PL spectra. QWT growth can be enhanced on some facets of a nanowire, leading to a reduction in symmetry of the QWT about the long axis of the nanowire [216, 219]. Indeed, these effects are observed in TEM micrographs of the nanowires used in this study. In order to investigate the effect of such inhomogeneous well widths on nanowire PL, two different geometries are simulated: an "ideal" nanowire with uniform QWT thickness of 3.5 nm; and a "disordered" nanowire with facet thicknesses varying from 3 to 4 nm. The simulation results are presented in Figure 6.7b. It can be seen that PL emission from the core (lower energy peak) is largely unaffected by geometric distortions; however, PL from

the QWT is significantly broadened by disorder. This sensitivity to geometric distortions is confirmed by the experimental results (presented in Figure 6.3), and indicates why the disorder parameter for the QWT is much larger than that of the core.

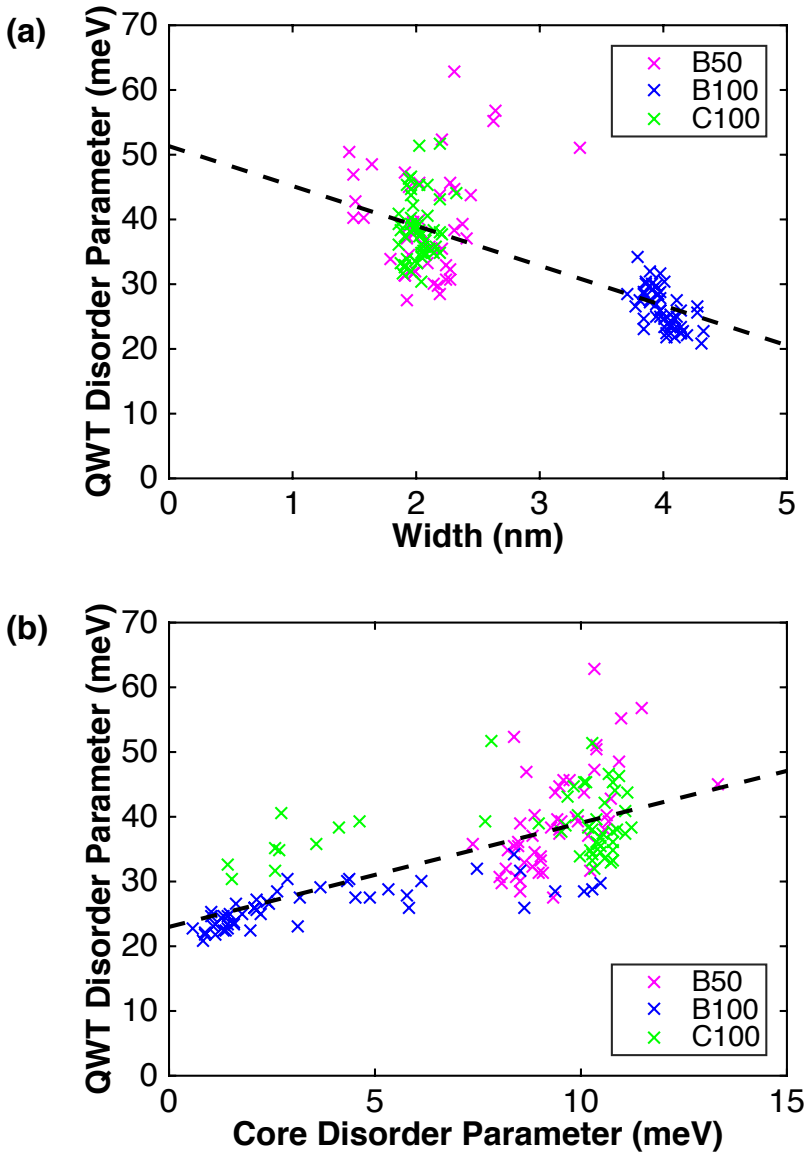


Figure 6.3: **a** Correlation of the disorder parameter in the QWT with the width of the well. **b** Correlation of the disorder parameter in the QWT with the disorder in the core. The dashed lines in both graphs show a linear least-squares fit of the data.

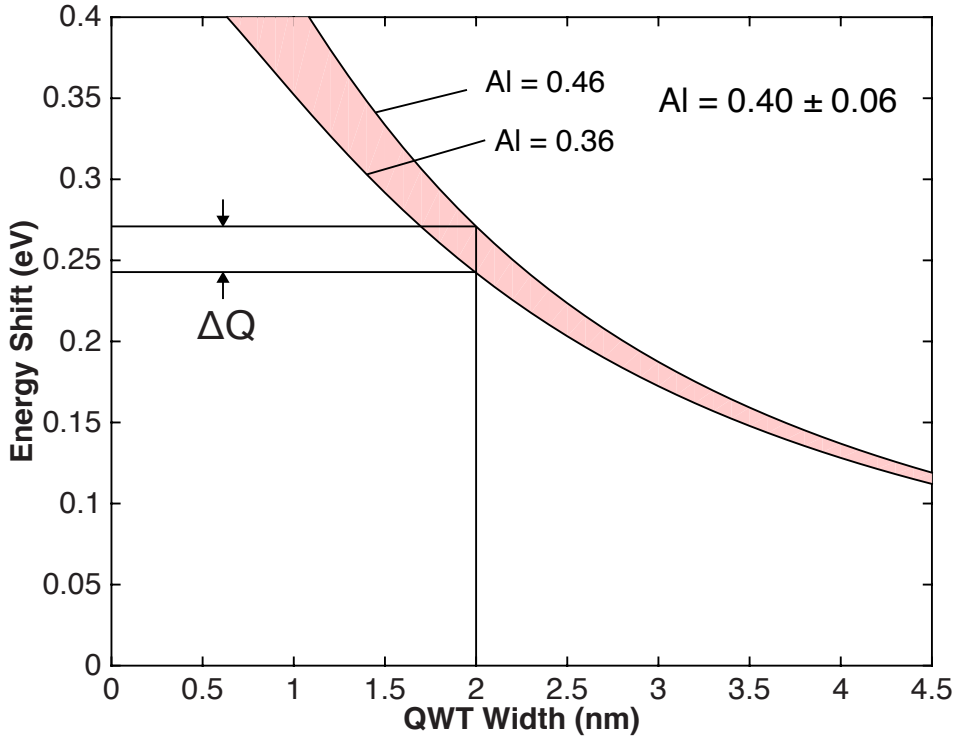


Figure 6.4: Energy shift of the quantum well energy level with quantum well width. ΔQ shows the energetic distribution of shifts for different aluminium concentrations

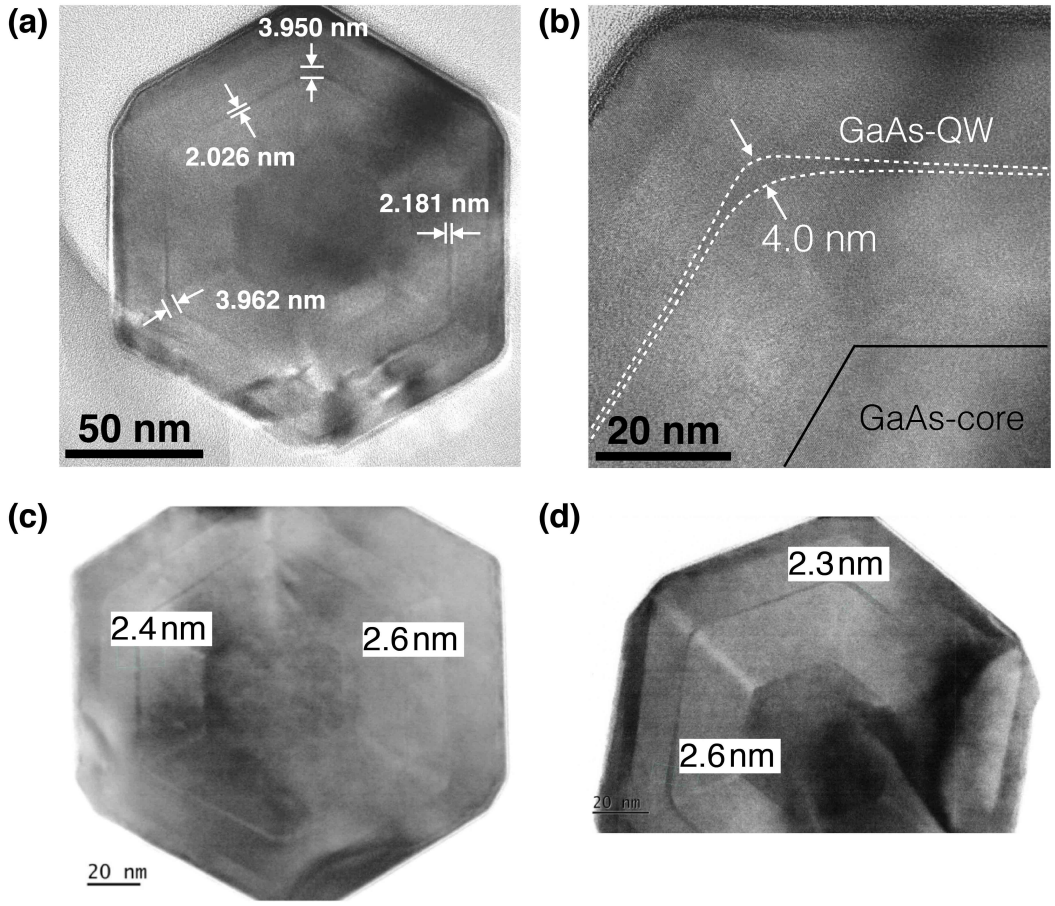


Figure 6.5: **a** and **b** Transmission electron microscope (TEM) image of the top of sample B50. **a** The quantum well width is measured at various positions around the nanowire. **b** The quantum well is highlighted by white dashed lines and the width at the corner is measured to be 4.0 nm. TEM image of the bottom **c** and top **d** of sample B50.

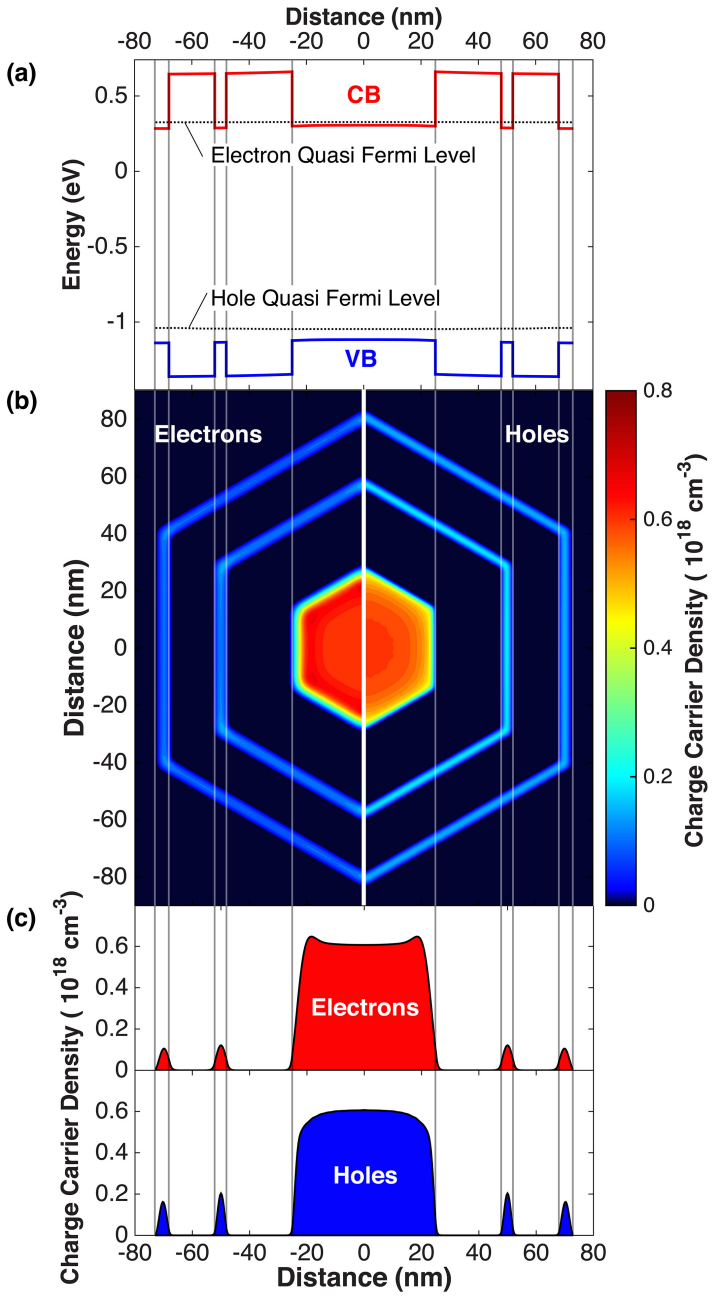


Figure 6.6: Simulation of the band structure and charge carrier distribution in a quantum well tube nanowire. Vertical grey lines act as a guide for the eye signifying different shell layers. **a** Red and blue lines show the band structure for the conduction band (CB) and valence band (VB) respectively. The two dotted lines show the electron and hole quasi Fermi levels for an excited state. **b** 2D colour plot of the density of electrons (left) and the density of holes (right) for a cross section of the nanowire in an excited state. **c** Charge carrier densities of the electrons and holes in an excited state. There is a slight band bending present giving rise to a difference in distributions for the electrons in the conduction band and holes in the valence band.

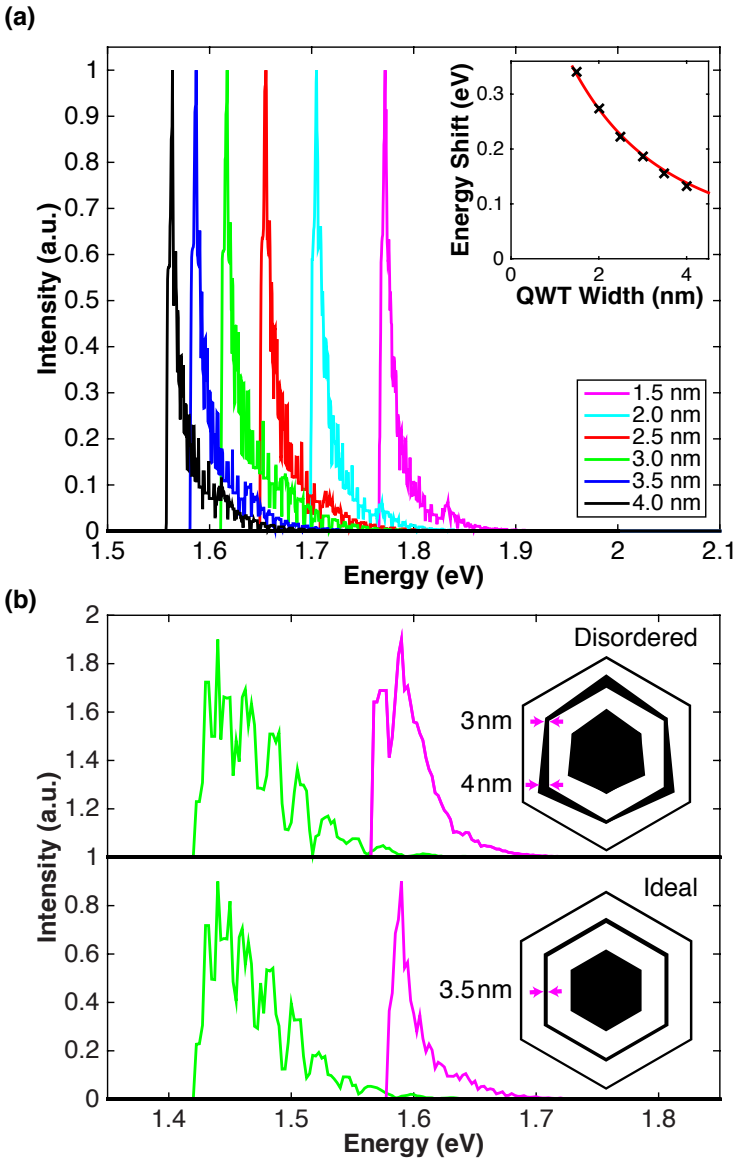


Figure 6.7: Simulation of quantum well tube nanowire photoluminescence. **a** Simulated PL of a selection of nanowires with different well widths ranging from 1.5 nm to 4 nm in increments of 0.5 nm. The inset shows the energy shift of the ground state due to confinement as a function of well width. The black crosses are from the simulation results and the red line is from the 1D analytical model. **b** The green lines show simulated PL from a nanowire core (Ideal: 50 nm; Disordered: 50 ± 2 nm) and the magenta lines show simulated PL from a QWT (Ideal: 3.5 nm; Disordered: 3.5 ± 0.5 nm). The lower plot is for a nanowire with an ideal hexagon geometry. The upper plot is for a nanowire, whose geometry is distorted from a regular hexagon. The insets in (b) show the geometry of the nanowire (not to scale). GaAs and AlGaAs materials are shown in black and white respectively.

6.3 Summary

In summary, photoluminescence spectra from 150 individual core-multishell GaAs/$Al_{0.4}Ga_{0.6}$As nanowires were measured and a statistical analysis performed. This allowed inter-sample and intra-sample variations in QWT width and disorder to be examined. Quantum confinement effects were observed for all nanowire spectra with two clearly defined peaks being attributed to luminescence from the nanowire core and QWT. The QWT widths were calculated from the PL spectra using a finite well model, and confirmed using a full 2D simulation. The disorder for the QWT was quantified by modelling the shape of PL spectra. Disorder was found to be consistently larger in the QWT (40 ± 10 meV) than in the core (8 ± 2 meV) owing to the sensitivity of PL emission energy on variations of QWT width. Correlations between the disorder in the core and QWT are consistent with defects from the core propagating to the QWT and highlights the importance of high quality core growth in the quest for more uniform QWTs. Measurements of well widths and disorder using room temperature PL spectra were demonstrated to be a useful method to characterise nanowires containing quantum wells. This shows the suitability of the single nanowire PL technique for assessing the quality and uniformity of nanowires prior to their implementation in devices.

Chapter 7

Conclusion

Over recent years there has been a significant research interest into metal-halide perovskites and nanowires. Both fields are maturing with the hope to realise their potential to be used in next generation optoelectronic devices and specifically towards the goal of increasing our light harvesting capabilities.

In Chapter 4, the temperature dependent absorption spectra of $MAPbI_3$ was investigated to further our understanding of the recombination mechanism in hybrid perovskite systems. With efficiencies of perovskite based solar cells rapidly increasing, the Shockley-Queisser limit is being approached. Towards this limit bimolecular recombination between electrons and holes will become the dominant mechanism of recombination – trap-assisted monomolecular recombination will be negligible at this limit. Using the van Roosbroeck-Shockley relation with the measured absorption coefficients, and comparing the obtained bimolecular recombination rate constants with those previously measured by transient terahertz spectroscopy, demonstrated that bimolecular recombination in $MAPbI_3$ can be seen as the inverse to absorption. The sharpening of photon (Bose-Einstein), electron and hole (Fermi-Dirac) distribution functions is shown to enhance the bimolecular radiative rate by roughly an order of magnitude as the temperature is lowered from room temperature to $\sim$50 K. Addi-

tionally, screening of the Coulomb interactions between electrons and holes above the Mott transition is shown to reduce bimolecular recombination constants, meaning that such values have to be considered in the context of the charge-carrier densities present. These results provide crucial fundamental understanding of the optoelectronic processes in these metal-halide perovskites.

In Chapter 5, the temperature dependent studies of $FAPbI_3$ have revealed significant differences in the optoelectronic properties in comparison with $MAPbI_3$. Intra-excitonic transitions were directly observed in $FAPbI_3$ from which the exciton binding energy was determined to be 5.3 meV at 10 K, which is at the low end of the spectrum of reported values for $MAPbI_3$. Further, this chapter examined how parameters critical to the operation of photovoltaic cells, such as the exciton binding energy, band gap, vibrational properties and charge-carrier mobilities vary with temperature and across phase transitions. In contrast to $MAPbI_3$, the band gap and exciton binding energy varies smoothly over a range of 100–160 K at the β to γ phase transition in $FAPbI_3$. Such absence of clear discontinuities for $FAPbI_3$ most likely results from the rotational freedom of the FA dipole moment being reduced only gradually upon entry into the γ phase, whereas in $MAPbI_3$, MA dipole rotation is frozen out abruptly over a narrow temperature range. This chapter also demonstrated that such structural changes manifest themselves in the IR phonon signatures associated with the lead-halide sublattice vibrations. The two phonon modes observed in the β phase are largely unchanged for $FAPbI_3$ upon entry into the γ phase, while for $MAPbI_3$, a splitting into four phonon modes is observed. Finally, the charge-carrier mobility in $FAPbI_3$ was revealed to exhibit a clear $T^{-0.5}$ trend with temperature, in excellent agreement with theoretical predictions for halide perovskites whose electron-phonon interactions are governed by the Fröhlich mechanism, but in contrast to the $T^{-1.5}$ dependence previously observed for $MAPbI_3$. The contrasting temperature-dependent behaviour of excitons, phonons, electronic transitions and charge-carrier mobilities

in $MAPbI_3$ and $FAPbI_3$ highlight the impact of cation substitution not only on the structure of the perovskite but also on its optoelectronic properties.

In Chapter 6, photoluminescence spectra from 150 individual core-multishell $GaAs/Al_{0.4}Ga_{0.6}As$ nanowires were measured and a statistical analysis performed. This allowed inter-sample and intra-sample variations in QWT width and disorder to be examined. Quantum confinement effects were observed for all nanowire spectra with two clearly defined peaks being attributed to luminescence from the nanowire core and QWT. The QWT widths were calculated from the PL spectra using a finite well model, and confirmed using a full 2D simulation. The disorder for the QWT was quantified by modelling the shape of PL spectra. Disorder was found to be consistently larger in the QWT (40 ± 10 meV) than in the core (8 ± 2 meV) owing to the sensitivity of PL emission energy on variations of QWT width. Correlations between the disorder in the core and QWT are consistent with defects from the core propagating to the QWT and highlights the importance of high quality core growth in the quest for more uniform QWTs. Measurements of well widths and disorder using room temperature PL spectra were demonstrated to be a useful method to characterise nanowires containing quantum wells. This shows the suitability of the single nanowire PL technique for assessing the quality and uniformity of nanowires prior to their implementation in devices.

7.1 Outlook

The fundamental optoelectronic properties of metal-halide perovskites has been explored for the prototypical perovskite, $MAPbI_3$, and the closely related material $FAPbI_3$ - both single-cation, single-halide perovskites. Significant improvements in photovoltaic device efficiencies and stabilities have been at least in part owing to the use of mixed-cation, mixed-halide perovskite systems, such as $FA_{1-y}Cs_yPbI_{1-x}Br_x$

[223]. Looking to the future, it will be important to continue to build on our knowledge of non-mixed perovskite systems, such that we can better understand the optoelectronic properties of the mixed perovskite materials.

Examining the statistical distributions of the optoelectronic properties of nanowires (Chapter 6) has proven to be an important endeavour. Based on this initial study, further work has been carried out by Dr. Patrick Parkinson's group at Manchester University [224], where automation of the experimental technique has allowed them to explore the properties of many thousands of nanowires from a single growth. Continuing our understanding of the statistical distribution of the optoelectronic properties of nanowires will be important for their future implementation into devices.

Finally, there is the possibility to combine nanowires and perovskites in a single photovoltaic device. By utilising vertically grown nanowires as an electron transport layer that penetrates into the metal halide perovskite absorbing layer, the distance that electrons need to travel to escape the absorbing layer will be reduced. This reduction in distance would speed up the spatial separation of electrons and holes, thus reducing the chance of electrons and holes recombining. This novel device architecture has the potential to increase device efficiencies beyond the current limits.

Bibliography

[1] Richard Wrangham. *Catching fire: How cooking made us human*. Basic Books, 2009.

[2] Robert J Braidwood. The Agricultural Revolution. *Scientific American*, 203(3):130–152, 1960.

[3] S B Snider and J N Brimlow. An introduction to population growth. *Nature Education Knowledge*, 4(4):3, 2013.

[4] Achala Abeysinghe and Subhi Barakat. The Paris Agreement. *International Institute for Environment and Development*, 2016.

[5] T Jayaraman and Tejal Kanitkar. The Paris Agreement. *Economic and Political Weekly*, 51(3), 2016.

[6] Inagaki K Raval A. Saudi Arabia signs SoftBank deal to invest up to 200bn USD in solar. *Financial Times*, March 28, 2018.

[7] R S Wagner and W C Ellis. Vapor-Liquid-Solid Mechanism of Single Crystal Growth. *Applied Physics Letters*, 4(5):89–90, 1964.

[8] Christopher L Davies, Patrick Parkinson, Nian Jiang, Jessica L Boland, Sonia Conesa-Boj, Hark Hoe Tan, C Jagadish, Laura M Herz, and Michael B Johnston. Low Ensemble Disorder in Quantum Well Tube Nanowires. *Nanoscale*, 7:20531–20538, 2015.

[9] Martin A Green and Anita Ho-Baillie. Perovskite Solar Cells: The Birth of a New Era in Photovoltaics. *ACS Energy Letters*, 2(4):822–830, 2017.

[10] D B Mitzi, C A Feild, W T A Harrison, and A M Guloy. Conducting tin halides with a layered organic-based perovskite structure. *Nature*, 369:467, jun 1994.

[11] D B Mitzi, S Wang, C A Feild, C A Chess, and A M Guloy. Conducting Layered Organic-inorganic Halides Containing -Oriented Perovskite Sheets. *Science*, 267(5203):1473–1476, 1995.

[12] C R Kagan, D B Mitzi, and C D Dimitrakopoulos. Organic-Inorganic Hybrid Materials as Semiconducting Channels in Thin-Film Field-Effect Transistors. *Science*, 286(5441):945–947, 1999.

[13] NREL Research Cell Record Efficiency Chart. https://www.nrel.gov/pv/assets/images/efficiency-chart.png.

[14] Julian Burschka, Norman Pellet, Soo-Jin Moon, Robin Humphry-Baker, Peng Gao, Mohammad K Nazeeruddin, and Michael Grätzel. Sequential deposition as a route to high-performance perovskite-sensitized solar cells. *Nature*, 499:316, jul 2013.

[15] Giles E Eperon, Samuel D Stranks, Christopher Menelaou, Michael B Johnston, Laura M Herz, and Henry J Snaith. Formamidinium lead trihalide: a broadly tunable perovskite for efficient planar heterojunction solar cells. *Energy Environ. Sci.*, 7(3):982–988, 2014.

[16] Mingzhen Liu, Michael B Johnston, and Henry J Snaith. Efficient planar heterojunction perovskite solar cells by vapour deposition. *Nature*, 501:395, sep 2013.

[17] Jay B Patel, Jennifer Wong-Leung, Stephan Van Reenen, Nobuya Sakai, Jacob Tse Wei Wang, Elizabeth S Parrott, Mingzhen Liu, Henry J Snaith, Laura M Herz, and Michael B Johnston. Influence of interface morphology on hysteresis in vapor-deposited perovskite solar cells. *Adv. Electron. Mater.*, page 1600470, 2016.

[18] Juliane Borchert, Rebecca L Milot, Jay B Patel, Christopher L Davies, Adam D Wright, Laura Martínez Maestro, Henry J Snaith, Laura M Herz, and Michael B Johnston. Large-Area, Highly Uniform Evaporated Formamidinium Lead Triiodide Thin Films for Solar Cells. *ACS Energy Letters*, 2(12):2799–2804, 2017.

[19] Zhanhua Wei, Haining Chen, Keyou Yan, and Shihe Yang. Inkjet Printing and Instant Chemical Transformation of a $CH_3NH_3PbI_3$ / Nanocarbon Electrode and Interface for Planar Perovskite Solar Cells. *Angew. Chem.*, 126(48):13455–13459, 2014.

[20] Laura M Herz. Charge-carrier mobilities in metal halide perovskites: fundamental mechanisms and limits. *ACS Energy Lett.*, 2(7):1539–1548, 2017.

[21] Silver-Hamill Turren-Cruz, Michael Saliba, Matthew T Mayer, Hector Juarez-Santiesteban, Xavier Mathew, Lea Nienhaus, Wolfgang Tress, Matthew P Erodici, Meng-Ju Sher, Moungi G Bawendi, Michael Gratzel, Antonio Abate, Anders Hagfeldt, and Juan-Pablo Correa-Baena. Enhanced charge carrier mobility and lifetime suppress hysteresis and improve efficiency in planar perovskite solar cells. *Energy Environ. Sci.*, 11(1):78–86, 2018.

[22] Waqaas Rehman, Rebecca L Milot, Giles E Eperon, Christian Wehrenfennig, Jessica L Boland, Henry J Snaith, Michael B Johnston, and Laura M Herz. Charge-carrier dynamics and mobilities in formamidinium lead mixed-halide perovskites. *Adv. Mater.*, 27(48):7938–7944, 2015.

[23] Christian Wehrenfennig, Mingzhen Liu, Henry J Snaith, Michael B Johnston, and Laura M Herz. Charge carrier recombination channels in the low-temperature phase of organic-inorganic lead halide perovskite thin films. *APL Mater.*, 2(8):81513, 2014.

[24] Laura M Herz. Charge-carrier dynamics in organic-inorganic metal halide perovskites. *Annu. Rev. Phys. Chem.*, 67(1):65–89, 2016.

[25] Michael B Johnston and Laura M Herz. Hybrid perovskites for photovoltaics: charge-carrier recombination, diffusion, and radiative efficiencies. *Acc. Chem. Res.*, 49(1):146–154, 2016.

[26] Christopher L Davies, Marina R Filip, Jay B Patel, Timothy W Crothers, Carla Verdi, Adam D Wright, Rebecca L Milot, Feliciano Giustino, Michael B Johnston, and Laura M Herz. Bimolecular recombination in methylammonium lead triiodide perovskite is an inverse absorption process. *Nat. Commun.*, 9(1):293, 2018.

[27] Martin A Green, Anita Ho-Baillie, and Henry J Snaith. The emergence of perovskite solar cells. *Nat. Photon.*, 8(7):506–514, jul 2014.

[28] Jin Hyuck Heo and Sang Hyuk Im. CH3NH3PbBr3CH3NH3PbI3 Perovskite-Perovskite Tandem Solar Cells with Exceeding 2.2 V Open Circuit Voltage. *Advanced Materials*, 28(25):5121–5125, 2016.

[29] Dewei Zhao, Changlei Wang, Zhaoning Song, Yue Yu, Cong Chen, Xingzhong Zhao, Kai Zhu, and Yanfa Yan. Four-Terminal All-Perovskite Tandem Solar Cells Achieving Power Conversion Efficiencies Exceeding 23%. *ACS Energy Letters*, 3(2):305–306, 2018.

[30] David P McMeekin, Golnaz Sadoughi, Waqaas Rehman, Giles E Eperon, Michael Saliba, Maximilian T Hörantner, Amir Haghighirad, Nobuya Sakai,

Lars Korte, Bernd Rech, Michael B Johnston, Laura M Herz, and Henry J Snaith. A mixed-cation lead mixed-halide perovskite absorber for tandem solar cells. *Science*, 351(6269):151–155, 2016.

[31] Bo Chen, Mengjin Yang, Xiaojia Zheng, Congcong Wu, Wenle Li, Yongke Yan, Juan Bisquert, Germà Garcia-Belmonte, Kai Zhu, and Shashank Priya. Impact of capacitive effect and ion migration on the hysteretic behavior of perovskite solar cells. *The journal of physical chemistry letters*, 6(23):4693–4700, 2015.

[32] E Tenuta, C Zheng, and O Rubel. Thermodynamic origin of instability in hybrid halide perovskites. *Scientific Reports*, 6:37654, nov 2016.

[33] Hannah J Joyce, Jennifer Wong-Leung, Qiang Gao, H Hoe Tan, and Chennupati Jagadish. Phase Perfection in Zinc Blende and Wurtzite IIIV Nanowires Using Basic Growth Parameters. *Nano Letters*, 10(3):908–915, 2010.

[34] Maoqing Yao, Ningfeng Huang, Sen Cong, Chun Yung Chi, M. Ashkan Seyedi, Yen Ting Lin, Yu Cao, Michelle L. Povinelli, P. Daniel Dapkus, and Chongwu Zhou. GaAs nanowire array solar cells with axial p-i-n junctions. *Nano Lett.*, 14(6):3293–3303, 2014.

[35] Yongquan Qu and Xiangfeng Duan. One-dimensional homogeneous and heterogeneous nanowires for solar energy conversion. *J. Mater. Chem.*, 22(32):16171, 2012.

[36] Kun Peng, Patrick Parkinson, Lan Fu, Qiang Gao, Nian Jiang, Ya-nan Guo, Fan Wang, Hannah J Joyce, Jessica L Boland, Hark Hoe Tan, Chennupati Jagadish, and Michael B Johnston. Single Nanowire Photoconductive Terahertz Detectors. *Nano Lett.*, 15(1):206–210, dec 2014.

[37] Miriam S Vitiello, Leonardo Viti, Lorenzo Romeo, Daniele Ercolani, G Scalari, J Faist, F Beltram, L Sorba, and A Tredicucci. Semiconductor nanowires for

highly sensitive, room-temperature detection of terahertz quantum cascade laser emission. *Appl. Phys. Lett.*, 100(24):241101, 2012.

[38] L Romeo, D Coquillat, M Pea, D Ercolani, F Beltram, L Sorba, W Knap, A Tredicucci, and M S Vitiello. Nanowire-based field effect transistors for terahertz detection and imaging systems. *Nanotechnology*, 24(21):214005, 2013.

[39] Yi Cui, Zhaohui Zhong, Deli Wang, Wayne U Wang, and Charles M Lieber. High Performance Silicon Nanowire Field Effect Transistors. *Nano Lett.*, 3(2):149–152, jan 2003.

[40] Gengchiau Liang, Jie Xiang, Neerav Kharche, Gerhard Klimeck, Charles M Lieber, and Mark Lundstrom. Performance Analysis of a Ge/Si Core/Shell Nanowire Field-Effect Transistor. *Nano Lett.*, 7(3):642–646, mar 2007.

[41] Yong-Ho Ra, Rangaswamy Navamathavan, Hee-Il Yoo, and Cheul-Ro Lee. Single Nanowire Light-Emitting Diodes Using Uniaxial and Coaxial InGaN/GaN Multiple Quantum Wells Synthesized by Metalorganic Chemical Vapor Deposition. *Nano Lett.*, 14(3):1537–1545, mar 2014.

[42] Caofeng Pan, Lin Dong, Guang Zhu, Simiao Niu, Ruomeng Yu, Qing Yang, Ying Liu, and Zhong Lin Wang. High-resolution electroluminescent imaging of pressure distribution using a piezoelectric nanowire LED array. *Nat. Photon.*, 7(9):752–758, sep 2013.

[43] Hannah J Joyce, Qiang Gao, H Hoe Tan, C Jagadish, Yong Kim, Jin Zou, Leigh M Smith, Howard E Jackson, Jan M Yarrison-Rice, Patrick Parkinson, and Michael B Johnston. IIIV semiconductor nanowires for optoelectronic device applications. *Progress in Quantum Electronics*, 35(2):23–75, 2011.

[44] Hannah J Joyce, Qiang Gao, H Hoe Tan, Chennupati Jagadish, Yong Kim, Xin

Zhang, Yanan Guo, and Jin Zou. Twin-free uniform epitaxial GaAs nanowires grown by a two-temperature process. *Nano Lett.*, 7(4):921–926, 2007.

[45] Patrick Parkinson, James Lloyd-Hughes, Qiang Gao, H Hoe Tan, Chennupati Jagadish, Michael B Johnston, and Laura M Herz. Transient Terahertz Conductivity of GaAs Nanowires. *Nano Lett.*, 7(7):2162–2165, jul 2007.

[46] L V Titova, Thang B Hoang, H E Jackson, L M Smith, J M Yarrison-Rice, Y Kim, H J Joyce, H H Tan, and C Jagadish. Temperature dependence of photoluminescence from single core-shell GaAsAlGaAs nanowires. *Appl. Phys. Lett.*, 89(17):173126, 2006.

[47] Hannah J Joyce, Jennifer Wong-Leung, Chaw-Keong Yong, Callum J Docherty, Suriati Paiman, Qiang Gao, H Hoe Tan, Chennupati Jagadish, James Lloyd-Hughes, Laura M Herz, and Michael B Johnston. Ultralow Surface Recombination Velocity in InP Nanowires Probed by Terahertz Spectroscopy. *Nano Lett.*, 12(10):5325–5330, oct 2012.

[48] Hannah J Joyce, Patrick Parkinson, Nian Jiang, Callum J Docherty, Qiang Gao, H Hoe Tan, Chennupati Jagadish, Laura M Herz, and Michael B Johnston. Electron Mobilities Approaching Bulk Limits in Surface-Free GaAs Nanowires. *Nano Letters*, 14(10):5989–5994, 2014.

[49] Melodie Fickenscher, Teng Shi, Howard E Jackson, Leigh M Smith, Jan M Yarrison-Rice, Changlin Zheng, Peter Miller, Joanne Etheridge, Bryan M Wong, Qiang Gao, Shriniwas Deshpande, Hark Hoe Tan, and Chennupati Jagadish. Optical, Structural, and Numerical Investigations of GaAs/AlGaAs CoreMultishell Nanowire Quantum Well Tubes. *Nano Lett.*, 13(3):1016–1022, feb 2013.

[50] Dhruv Saxena, Nian Jiang, Xiaoming Yuan, Sudha Mokkapati, Yanan Guo, Hark Hoe Tan, and Chennupati Jagadish. Design and Room-Temperature Op-

eration of GaAs/AlGaAs Multiple Quantum Well Nanowire Lasers. *Nano Letters*, 16(8):5080–5086, 2016.

[51] Fang Qian, Yat Li, Silvija Gradečak, Deli Wang, Carl J Barrelet, and Charles M Lieber. Gallium Nitride-Based Nanowire Radial Heterostructures for Nanophotonics. *Nano Letters*, 4(10):1975–1979, 2004.

[52] R J Elliott. Intensity of optical absorption by excitons. *Phys. Rev.*, 108(6):1384, 1957.

[53] Peter Y. Yu and Manuel Cardona. *Fundamentals of semiconductors: physics and materials properties*. Springer Science and Business Media, 2010.

[54] W van Roosbroeck and W Shockley. Photon-radiative recombination of electrons and holes in germanium. *Phys. Rev.*, 94(6):1558–1560, jun 1954.

[55] Y P Varshni. Band-to-band radiative recombination in groups IV, VI, and III-V semiconductors (I). *Phys. Status Solidi B*, 19(2):459–514, 1967.

[56] M A Peréz-Osorio, R Millot, M R Filip, J B Patel, L M Herz, M B Johnston, and F Giustino. Vibrational properties of the organic–inorganic halide perovskite $CH_3NH_3PbI_3$ from theory and experiment: factor group analysis, first-principles calculations, and low-temperature infrared spectra. *J. Phys. Chem. C*, 119:25703–25718, 2015.

[57] A Rice, Y Jin, X F Ma, X.C. Zhang, D Bliss, J Larkin, and M Alexander. Terahertz optical rectification from 110 zincblende crystals. *Applied Physics Letters*, 64(11):1324–1326, 1994.

[58] Ajay Nahata, David H Auston, Tony F Heinz, and Chengjiu Wu. Coherent detection of freely propagating terahertz radiation by electrooptic sampling. *Applied Physics Letters*, 68(2):150–152, 1996.

[59] F Blanchard, L Razzari, H.-C. Bandulet, G Sharma, R Morandotti, J.-C. Kieffer, T Ozaki, M Reid, H F Tiedje, H K Haugen, and F A Hegmann. Generation of 1.5 μJ single-cycle terahertz pulses by optical rectification from a large aperture ZnTe crystal. *Opt. Express*, 15(20):13212–13220, oct 2007.

[60] Q Wu and X.-C. Zhang. 7 terahertz broadband GaP electro-optic sensor. *Applied Physics Letters*, 70(14):1784–1786, 1997.

[61] T Kampfrath, M Battiato, P Maldonado, G Eilers, J Nötzold, S Mährlein, V Zbarsky, F Freimuth, Y Mokrousov, S Blügel, M Wolf, I Radu, P M Oppeneer, and M Münzenberg. Terahertz spin current pulses controlled by magnetic heterostructures. *Nat. Nanotechnol.*, 8:256, mar 2013.

[62] T Seifert, S Jaiswal, U Martens, J Hannegan, L Braun, P Maldonado, F Freimuth, A Kronenberg, J Henrizi, I Radu, E Beaurepaire, Y Mokrousov, P M Oppeneer, M Jourdan, G Jakob, D Turchinovich, L M Hayden, M Wolf, M Münzenberg, M Kläui, and T Kampfrath. Efficient metallic spintronic emitters of ultrabroadband terahertz radiation. *Nature Photonics*, 10:483, may 2016.

[63] D H Auston, K P Cheung, and P R Smith. Picosecond photoconducting Hertzian dipoles. *Applied Physics Letters*, 45(3):284–286, 1984.

[64] P R Smith, D H Auston, and M C Nuss. Subpicosecond photoconducting dipole antennas. *IEEE Journal of Quantum Electronics*, 24(2):255–260, feb 1988.

[65] D J Cook and R M Hochstrasser. Intense terahertz pulses by four-wave rectification in air. *Opt. Lett.*, 25(16):1210–1212, aug 2000.

[66] Hua Zhong, Nick Karpowicz, and X.-C. Zhang. Terahertz emission profile from laser-induced air plasma. *Applied Physics Letters*, 88(26):261103, 2006.

[67] L Xu, X.C. Zhang, and D H Auston. Terahertz beam generation by femtosecond optical pulses in electrooptic materials. *Applied Physics Letters*, 61(15):1784–1786, 1992.

[68] X.C. Zhang, X F Ma, Y Jin, T.M. Lu, E P Boden, P D Phelps, K R Stewart, and C P Yakymyshyn. Terahertz optical rectification from a nonlinear organic crystal. *Applied Physics Letters*, 61(26):3080–3082, 1992.

[69] Timothy J Carrig, G Rodriguez, Tracy Sharp Clement, A J Taylor, and Kevin R Stewart. Scaling of terahertz radiation via optical rectification in electrooptic crystals. *Applied Physics Letters*, 66(2):121–123, 1995.

[70] Q Wu and X.C. Zhang. Freespace electrooptic sampling of terahertz beams. *Applied Physics Letters*, 67(24):3523–3525, 1995.

[71] D Grischkowsky, Søren Keiding, Martin van Exter, and Ch. Fattinger. Far-infrared time-domain spectroscopy with terahertz beams of dielectrics and semiconductors. *J. Opt. Soc. Am. B*, 7(10):2006–2015, oct 1990.

[72] Shunsuke Kono, Masahiko Tani, Ping Gu, and Kiyomi Sakai. Detection of up to 20 THz with a low-temperature-grown GaAs photoconductive antenna gated with 15 fs light pulses. *Applied Physics Letters*, 77(25):4104–4106, 2000.

[73] I-Chen Ho, Xiaoyu Guo, and X.-C. Zhang. Design and performance of reflective terahertz air-biased-coherent-detection for time-domain spectroscopy. *Opt. Express*, 18(3):2872–2883, feb 2010.

[74] Xiaofei Lu and X.-C. Zhang. Balanced terahertz wave air-biased-coherent-detection. *Applied Physics Letters*, 98(15):151111, 2011.

[75] J Lloyd-Hughes, H E Beere, D A Ritchie, and M B Johnston. Terahertz magne-

toconductivity of excitons and electrons in quantum cascade structures. *Phys. Rev. B*, 77(12):125322, mar 2008.

[76] Lionel Duvillaret. A Reliable Method for Extraction of Material Parameters in Terahertz Time-Domain Spectroscopy. *IEEE Journal of selected topics in quantum electronics*, 2(3):739–746, 1996.

[77] Lionel Duvillaret, Frédéric Garet, and Jean-Louis Coutaz. Highly precise determination of optical constants and sample thickness in terahertz time-domain spectroscopy. *Applied Optics*, 38(2):409, 1999.

[78] F Bréhat and B Wyncke. Measurement of the optical constants of crystal quartz at 10 K and 300 K in the far infrared spectral range: 10–600 cm^{-1}. *International Journal of Infrared and Millimeter Waves*, 18(9):1663–1679, 1997.

[79] Christian Wehrenfennig, Giles E Eperon, Michael B Johnston, Henry J Snaith, and Laura M Herz. High charge carrier mobilities and lifetimes in organolead trihalide perovskites. *Adv. Mater.*, 26(10):1584–1589, 2014.

[80] R A Kaindl, D Hägele, M A Carnahan, and D S Chemla. Transient terahertz spectroscopy of excitons and unbound carriers in quasi-two-dimensional electron-hole gases. *Phys. Rev. B*, 79(4):45320, jan 2009.

[81] Hee-Won Lee. Matrix Elements and Cross Section of Raman Scattering by Atomic Hydrogen. *Publications of The Korean Astronomical Society*, 22(1):21–33, 2007.

[82] Liang Luo, Long Men, Zhaoyu Liu, Yaroslav Mudryk, Xin Zhao, Yongxin Yao, Joong M Park, Ruth Shinar, Joseph Shinar, Kai-Ming Ho, Ilias E Perakis, Javier Vela, and Jigang Wang. Ultrafast terahertz snapshots of excitonic Rydberg states and electronic coherence in an organometal halide perovskite. *Nat. Commun.*, 8:15565, jun 2017.

[83] N G Park, M Grätzel, and T Miyasaka. *Organic-inorganic halide perovskite photovoltaics: from fundamentals to device architectures*. Springer International Publishing, 2016.

[84] Martin A Green, Keith Emery, Yoshihiro Hishikawa, Wilhelm Warta, Ewan D Dunlop, Dean H Levi, and Anita W Y Ho-Baillie. Solar cell efficiency tables (version 49). *Prog. Photovolt: Res. Appl.*, 25:3–13, 2017.

[85] Atsuhiko Miyata, Anatolie Mitioglu, Paulina Plochocka, Oliver Portugall, Jacob Tse-Wei Wang, Samuel D Stranks, Henry J Snaith, and Robin J Nicholas. Direct measurement of the exciton binding energy and effective masses for charge carriers in organic-inorganic tri-halide perovskites. *Nat. Phys.*, 11(7):582–587, 2015.

[86] Yasuhiro Yamada, Toru Nakamura, Masaru Endo, Atsushi Wakamiya, and Yoshihiko Kanemitsu. Photocarrier recombination dynamics in perovskite $CH_3NH_3PbI_3$ for solar cell applications. *J. Am. Chem. Soc.*, 136(33):11610–11613, 2014.

[87] Joseph S Manser and Prashant V Kamat. Band filling with free charge carriers in organometal halide perovskites. *Nat. Photon.*, 8(9):737–743, sep 2014.

[88] Lili Wang, Christopher McCleese, Anton Kovalsky, Yixin Zhao, and Clemens Burda. Femtosecond time-resolved transient absorption spectroscopy of $CH_3NH_3PbI_3$ perovskite films: evidence for passivation effect of PbI_2. *J. Am. Chem. Soc.*, 136(35):12205–12208, 2014.

[89] Ye Yang, Mengjin Yang, Zhen Li, Ryan Crisp, Kai Zhu, and Matthew C Beard. Comparison of recombination dynamics in $CH_3NH_3PbBr_3$ and $CH_3NH_3PbI_3$ perovskite films: influence of exciton binding energy. *J. Phys. Chem. Lett.*, 6(23):4688–4692, 2015.

[90] Samuel D Stranks, Giles E Eperon, Giulia Grancini, Christopher Menelaou, Marcelo J P Alcocer, Tomas Leijtens, Laura M Herz, Annamaria Petrozza, and Henry J Snaith. Electron-Hole Diffusion lengths exceeding 1 micrometer in an organometal trihalide perovskite absorber. *Science*, 342(6156):341–344, 2013.

[91] Samuel D Stranks, Victor M Burlakov, Tomas Leijtens, James M Ball, Alain Goriely, and Henry J Snaith. Recombination kinetics in organic-inorganic perovskites: excitons, free charge, and subgap states. *Phys. Rev. Applied*, 2(3):34007, 2014.

[92] Elizabeth S Parrott, Rebecca L Milot, Thomas Stergiopoulos, Henry J Snaith, Michael B Johnston, and Laura M Herz. Effect of structural phase transition on charge-carrier lifetimes and defects in $CH_3NH_3SnI_3$ perovskite. *J. Phys. Chem. Lett.*, 7(7):1321–1326, 2016.

[93] Rebecca L Milot, Giles E Eperon, Henry J Snaith, Michael B Johnston, and Laura M Herz. Temperature-dependent charge-carrier dynamics in $CH_3NH_3PbI_3$ perovskite thin films. *Adv. Funct. Mater.*, 25(39):6218–6227, 2015.

[94] W Shockley and W T Read. Statistics of the recombinations of holes and electrons. *Phys. Rev.*, 87:835–842, 1952.

[95] Wan-Jian Yin, Tingting Shi, and Yanfa. Yan. Unusual defect physics in $CH_3NH_3PbI_3$ perovskite solar cell absorber. *Appl. Phys. Lett.*, 104(6):063903, 2014.

[96] Dane W DeQuilettes, Susanne Koch, Sven Burke, Rajan K Paranji, Alfred J Shropshire, Mark E Ziffer, and David S Ginger*. Photoluminescence lifetimes exceeding 8 μs and quantum yields exceeding 30% in hybrid perovskite thin films by ligand passivation. *ACS Energy Lett.*, 1:438–444, 2016.

[97] Ayan A Zhumekenov, Makhsud I Saidaminov, Md Azimul Haque, Erkki Alarousu, Smritakshi Phukan Sarmah, Banavoth Murali, Ibrahim Dursun, Xiao-He Miao, Ahmed L Abdelhady, Tom Wu, Omar F Mohammed, and Osman M Bakr. Formamidinium lead halide perovskite crystals with unprecedented long carrier dynamics and diffusion length. *ACS Energy Lett.*, 1(1):32–37, 2016.

[98] William Shockley and Hans J Queisser. Detailed balance limit of efficiency of p-n junction solar cells. *J. Appl. Phys.*, 32(3):510–519, 1961.

[99] Christian Wehrenfennig, Mingzhen Liu, Henry J Snaith, Michael B Johnston, and Laura M Herz. Charge-carrier dynamics in vapour-deposited films of the organolead halide perovskite $CH_3NH_3PbI_{3-x}Cl_x$. *Energy Environ. Sci.*, 7(7):2269–2275, 2014.

[100] Ajay Ram Srimath Kandada and Annamaria Petrozza. Research update: luminescence in lead halide perovskites. *APL Mater.*, 4(9):91506, 2016.

[101] Andreas Paulke, Samuel D Stranks, Juliane Kniepert, Jona Kurpiers, Christian M Wolff, Natalie Schön, Henry J Snaith, Thomas J K Brenner, and Dieter Neher. Charge carrier recombination dynamics in perovskite and polymer solar cells. *Appl. Phys. Lett.*, 108(11):113505, 2016.

[102] Alessio Filippetti, Pietro Delugas, and Alessandro Mattoni. Radiative recombination and photoconversion of methylammonium lead iodide perovskite by first principles: properties of an inorganic semiconductor within a hybrid body. *J. Phys. Chem. C*, 118(43):24843–24853, 2014.

[103] Michele Saba, Michele Cadelano, Daniela Marongiu, Feipeng Chen, Valerio Sarritzu, Nicola Sestu, Cristiana Figus, Mauro Aresti, Roberto Piras,

Alessandra Geddo Lehmann, and Others. Correlated electron-hole plasma in organometal perovskites. *Nat. Commun.*, 5, 2014.

[104] Fan Zheng, Liang Z Tan, Shi Liu, and Andrew M Rappe. Rashba spin-orbit coupling enhanced carrier lifetime in $CH_3NH_3PbI_3$. *Nano Lett.*, 15(12):7794–7800, 2015.

[105] Eline M Hutter, Maria C Gelvez-Rueda, Anna Osherov, Vladimir Bulovic, Ferdinand C Grozema, Samuel D Stranks, and Tom J Savenije. Direct-indirect character of the bandgap in methylammonium lead iodide perovskite. *Nat. Mater.*, 16(1):115–120, jan 2017.

[106] Pooya Azarhoosh, Scott McKechnie, Jarvist M Frost, Aron Walsh, and Mark van Schilfgaarde. Research update: relativistic origin of slow electron-hole recombination in hybrid halide perovskite solar cells. *APL Mater.*, 4(9):91501, 2016.

[107] Gordon Lasher and Frank Stern. Spontaneous and stimulated recombination radiation in semiconductors. *Phys. Rev.*, 133(2A):A553, jan 1964.

[108] G W 'tHooft and C van Opdorp. Temperature dependence of interface recombination and radiative recombination in (Al,Ga)As heterostructures. *Appl. Phys. Lett.*, 42:813–815, 1983.

[109] T Matsusue and H Sakaki. Radiative recombination coefficient of free carriers in GaAs-AlGaAs quantum wells and its dependence on temperature. *Appl. Phys. Lett.*, 50:1429–1431, 1987.

[110] H Schlangenotto, H Maeder, and W Gerlach. Temperature dependence of the radiative recombination coefficient in silicon. *Phys. Status Solidi A*, 21(1):357–367, 1974.

[111] T Trupke, Mr A Green, P Würfel, P P Altermatt, A Wang, J Zhao, and R Corkish. Temperature dependence of the radiative recombination coefficient of intrinsic crystalline silicon. *J. Appl. Phys.*, 94(8):4930–4937, 2003.

[112] Ye Yang, David P Ostrowski, Ryan M France, Kai Zhu, Jao Van De Lagemaat, Joseph M Luther, and Matthew C Beard. Observation of a hot-phonon bottleneck in lead-iodide perovskites. *Nat. Photon.*, 10(1):53–59, 2016.

[113] Naresh K Kumawat, Amrita Dey, Aravindh Kumar, Sreelekha P Gopinathan, K L Narasimhan, and Dinesh Kabra. Band gap tuning of $CH_3NH_3Pb(Br_{1-x}Cl_x)_3$ hybrid perovskite for blue electroluminescence. *ACS Appl. Mater. Interfaces*, 7(24):13119–13124, 2015.

[114] Christian Wehrenfennig, Mingzhen Liu, Henry J Snaith, Michael B Johnston, and Laura M Herz. Homogeneous emission line broadening in the organo lead halide perovskite $CH_3NH_3PbI_{3-x}Cl_x$. *J. Phys. Chem. Lett.*, 5(8):1300–1306, 2014.

[115] Adam D Wright, Carla Verdi, Rebecca L Milot, Giles E Eperon, Miguel A Pérez-Osorio, Henry J Snaith, Feliciano Giustino, Michael B Johnston, and Laura M Herz. Electron-phonon coupling in hybrid lead halide perovskites. *Nat. Commun.*, 7:11755, may 2016.

[116] Sergiu Draguta, Siddharatha Thakur, Yurii V Morozov, Yuanxing Wang, Joseph S Manser, Prashant V Kamat, and Masaru Kuno. Spatially non-uniform trap state densities in solution-processed hybrid perovskite thin films. *J. Phys. Chem. Lett.*, 7(4):715–721, 2016.

[117] Giulia Grancini, Ajay Ram Srimath Kandada, Jarvist M Frost, Alex J Barker, Michele De Bastiani, Marina Gandini, Sergio Marras, Guglielmo Lanzani, Aron Walsh, and Annamaria Petrozza. Role of microstructure in the electron-hole

interaction of hybrid lead-halide perovskites. *Nat. Photon.*, 9(10):695–701, oct 2015.

[118] Claus F Klingshirn. *Semiconductor optics*. Springer Science & Business Media, 2012.

[119] A Poglitsch and D Weber. Dynamic disorder in methylammonium trihalogen plumbates (II) observed my millimeter-wave spectroscopy. *J. Chem. Phys.*, 87:6373–6378, 1987.

[120] Nicola Sestu, Michele Cadelano, Valerio Sarritzu, Feipeng Chen, Daniela Marongiu, Roberto Piras, Marina Mainas, Francesco Quochi, Michele Saba, Andrea Mura, and Others. Absorption f-sum rule for the exciton binding energy in methylammonium lead halide perovskites. *J. Phys. Chem. Lett.*, 6(22):4566–4572, 2015.

[121] Jacky Even, Laurent Pedesseau, and Claudine Katan. Analysis of multivalley and multibandgap absorption and enhancement of free carriers related to exciton screening in hybrid perovskites. *J. Phys. Chem. C*, 118(22):11566–11572, 2014.

[122] Y Yamada, T Nakamura, M Endo, A Wakamiya, and Y Kanemitsu. Photoelectronic responses in solution-processed perovskite $CH_3NH_3PbI_3$ solar cells studied by photoluminescence and photoabsorption spectroscopy. *IEEE J. Photovolt.*, 5(1):401–405, jan 2015.

[123] Valerio D'Innocenzo, Giulia Grancini, Marcelo J P Alcocer, Ajay Ram Srimath Kandada, Samuel D Stranks, Michael M Lee, Guglielmo Lanzani, Henry J Snaith, and Annamaria Petrozza. Excitons versus free charges in organo-lead tri-halide perovskites. *Nat. Commun.*, 5:3586, 2014.

[124] Tom J Savenije, Carlito S Ponseca, Lucas Kunneman, Mohamed Abdellah, Kaibo Zheng, Yuxi Tian, Qiushi Zhu, Sophie E Canton, Ivan G Scheblykin, Tonu Pullerits, Arkady Yartsev, and Villy Sundström. Thermally activated exciton dissociation and recombination control the carrier dynamics in organometal halide perovskite. *J. Phys. Chem. Lett.*, 5(13):2189–2194, 2014.

[125] Y P Varshni. Temperature dependence of the energy gap in semiconductors. *Physica*, 34(1):149–154, 1967.

[126] Teruya Ishihara. Optical properties of PbI-based perovskite structures. *JOL*, 60:269–274, 1994.

[127] Jacky Even, Laurent Pedesseau, Claudine Katan, Mikaël Kepenekian, Jean-Sébastien Lauret, Daniel Sapori, and Emmanuelle Deleporte. Solid-state physics perspective on hybrid perovskite semiconductors. *J. Phys. Chem. C*, 119(19):10161–10177, 2015.

[128] Aron Walsh. Principles of chemical bonding and band gap engineering in hybrid organicinorganic halide perovskites. *J. Phys. Chem. C*, 119(11):5755–5760, 2015.

[129] C Katan, L Pedesseau, M Kepenekian, A Rolland, and J Even. Interplay of spin-orbit coupling and lattice distortion in metal substituted 3D tri-chloride hybrid perovskites. *J. Mater. Chem. A*, 3:9232–9240, 2015.

[130] Shivam Singh, Cheng Li, Fabian Panzer, K L Narasimhan, Anna Graeser, Tanaji P Gujar, Anna Köhler, Mukundan Thelakkat, Sven Huettner, and Dinesh Kabra. Effect of thermal and structural disorder on the electronic structure of hybrid perovskite semiconductor $CH_3NH_3PbI_3$. *J. Phys. Chem. Lett.*, 7(15):3014–3021, 2016.

[131] Marina R Filip and Feliciano Giustino. GW quasiparticle band gap of the hybrid organic-inorganic perovskite $CH_3NH_3PbI_3$: effect of spin-orbit interaction, semicore electrons, and self-consistency. *Phys. Rev. B*, 90(24):245145, dec 2014.

[132] Marina R Filip, Carla Verdi, and Feliciano Giustino. GW band structures and carrier effective masses of $CH_3NH_3PbI_3$ and hypothetical perovskites of the type $APbI_3$: A = NH_4, PH_4, AsH_4, and SbH_4. *J. Phys. Chem. C*, 119(45):25209–25219, 2015.

[133] Manuel Cardona and Fred H Pollak. Energy-band structure of germanium and silicon: the k·p method. *Phys. Rev.*, 142(2):530–543, feb 1966.

[134] P Würfel. The chemical potential of radiation. *J. Phys. C: Solid State Physics*, 15(18):3967, 1982.

[135] Martin J Klein. Principle of Detailed Balance. *Phys. Rev.*, 97(6):1446–1447, mar 1955.

[136] Kensuke Oki, Bei Ma, and Yoshihiro Ishitani. Population decay time and distribution of exciton states analyzed by rate equations based on theoretical phononic and electron-collisional rate coefficients. *Phys. Rev. B*, 96(20):205204, nov 2017.

[137] J Szczytko, L Kappei, J Berney, F Morier-Genoud, M T Portella-Oberli, and B Deveaud. Determination of the Exciton Formation in Quantum Wells from Time-Resolved Interband Luminescence. *Phys. Rev. Lett.*, 93(13):137401, sep 2004.

[138] N F Mott. Metal-insulator transition. *Rev. Mod. Phys.*, 40(4):677, 1968.

[139] Peter Phillip Edwards and Michell J Sienko. Universality aspects of the metal-nonmetal transition in condensed media. *Phys. Rev. B*, 17(6):2575, 1978.

[140] Hartmut Haug and Stefan Schmitt-Rink. Electron theory of the optical properties of laser-excited semiconductors. *Prog. Quant. Electron.*, 9(1):3–100, 1984.

[141] Timothy W Crothers, Rebecca L Milot, Jay B Patel, Elizabeth S Parrott, Johannes Schlipf, M Peter, and Michael B Johnston. Photon Reabsorption Masks Intrinsic Bimolecular Charge-Carrier Recombination in $CH_3NH_3PbI_3$ Perovskite. *Nano Lett.*, 17:1–44, 2017.

[142] J.M. Richter, M. Abdi-Jalebi, A. Sadhanala, M. Tabachnyk, J.P. Rivett, L.M. Pazos-Outón, K.C. Gödel, M. Price, F. Deschler, and R.H. Friend. Enhancing photoluminescence yields in lead halide perovskites by photon recycling and light out-coupling. *Nat. Commun.*, 7:13941, 2016.

[143] A Marti, J L Balenzategui, and R F Reyna. Photon recycling and Shockley's diode equation. *J. Appl. Phys.*, 82(8):4067–4075, 1997.

[144] Thomas Kirchartz, Florian Staub, and Uwe Rau. Impact of photon recycling on the open-circuit voltage of metal halide perovskite solar cells. *ACS Energy Lett.*, 1(4):731–739, 2016.

[145] Michael Saliba, Wei Zhang, Victor M Burlakov, Samuel D Stranks, Yao Sun, James M Ball, Michael B Johnston, Alain Goriely, Ulrich Wiesner, and Henry J Snaith. Plasmonic-induced photon recycling in metal halide perovskite solar cells. *Adv. Funct. Mater.*, 25(31):5038–5046, 2015.

[146] Woon Seok Yang, Jun Hong Noh, Nam Joong Jeon, Young Chan Kim, Seungchan Ryu, Jangwon Seo, and Sang Il Seok. High-performance photovoltaic perovskite layers fabricated through intramolecular exchange. *Science*, 348(6240):1234–1237, 2015.

[147] Shreetu Shrestha, Gebhard J. Matt, Andres Osvet, Daniel Niesner, Rainer Hock, and Christoph J. Brabec. Assessing Temperature Dependence of Drift

Mobility in Methylammonium Lead Iodide Perovskite Single Crystals. *Journal of Physical Chemistry C*, 122(11):5935–5939, 2018.

[148] Hikaru Oga, Akinori Saeki, Yuhei Ogomi, Shuzi Hayase, and Shu Seki. Improved Understanding of the Electronic and Energetic Landscapes of Perovskite Solar Cells: High Local Charge Carrier Mobility, Reduced Recombination, and Extremely Shallow Traps. *J. Am. Chem. Soc.*, 136(39):13818–13825, 2014.

[149] Dewei Zhao, Yue Yu, Changlei Wang, Weiqiang Liao, Niraj Shrestha, Corey R Grice, Alexander J Cimaroli, Lei Guan, Randy J Ellingson, Kai Zhu, Xingzhong Zhao, Ren-Gen Xiong, and Yanfa Yan. Low-bandgap mixed tinlead iodide perovskite absorbers with long carrier lifetimes for all-perovskite tandem solar cells. *Nat. Energy*, 2:17018, mar 2017.

[150] Anna Amat, Edoardo Mosconi, Enrico Ronca, Claudio Quarti, Paolo Umari, Md. K Nazeeruddin, Michael Grätzel, and Filippo De Angelis. Cation-Induced Band-Gap Tuning in Organohalide Perovskites: Interplay of Spin-Orbit Coupling and Octahedra Tilting. *Nano Lett.*, 14:3608–3616, 2014.

[151] Waqaas Rehman, David P McMeekin, Jay B Patel, Rebecca L Milot, Michael B Johnston, Henry J Snaith, and Laura M Herz. Photovoltaic Mixed-Cation Lead Mixed-Halide Perovskites: Links Between Crystallinity, Photo-Stability and Electronic Properties. *Energy Environ. Sci.*, 10:361–369, 2017.

[152] Jay B Patel, Qianqian Lin, Olga Zadvorna, Christopher L Davies, Laura M Herz, and Michael B Johnston. Photocurrent Spectroscopy of Perovskite Solar Cells Over a Wide Temperature Range from 15 to 350 K. *J. Phys. Chem. Lett.*, 9(1):263–268, 2018.

[153] Chan La-O-Vorakiat, Huanxin Xia, Jeannette Kadro, Teddy Salim, Daming Zhao, Towfiq Ahmed, Yeng Ming Lam, Jian-Xin Zhu, Rudolph A Marcus,

Maria-Elisabeth Michel-Beyerle, and Elbert E M Chia. Phonon Mode Transformation Across the OrthohombicTetragonal Phase Transition in a Lead Iodide Perovskite $CH_3NH_3PbI_3$: A Terahertz Time-Domain Spectroscopy Approach. *J. Phys. Chem. Lett.*, 7(1):1–6, 2016.

[154] Miguel A Perez-Osorio, Rebecca L Milot, Marina R Filip, Jay B Patel, Laura M Herz, Michael B Johnston, and Feliciano Giustino. Vibrational Properties of the Organic–Inorganic Halide Perovskite $CH_3NH_3PbI_3$ from Theory and Experiment: Factor Group Analysis, First-Principles Calculations, and Low-Temperature Infrared Spectra. *J. Phys. Chem. C*, 119:25703, 2015.

[155] R Huber, B A Schmid, R A Kaindl, and D S Chemla. Femtosecond THz studies of intra-excitonic transitions. *Phys. Status Solidi B*, 245(6):1041–1048, 2008.

[156] Rupert Huber, Robert A Kaindl, Ben A Schmid, and Daniel S Chemla. Broadband terahertz study of excitonic resonances in the high-density regime in $GaAs - Al_xGa_{1-x}As$ quantum wells. *Phys. Rev. B*, 72(16):161314, oct 2005.

[157] Eric M Talbert, Holly F Zarick, Abdelaziz Boulesbaa, Naiya Soetan, Alexander A Puretzky, David B Geohegan, and Rizia Bardhan. Bromine substitution improves excited-state dynamics in mesoporous mixed halide perovskite films. *Nanoscale*, 9(33):12005–12013, 2017.

[158] Jarvist Moore Frost. Calculating polaron mobility in halide perovskites. *Phys. Rev. B*, 96(19):195202, nov 2017.

[159] H Fröhlich. Electrons in Lattice Fields. *Adv. Phys.*, 3(11):325–361, 1954.

[160] M Karakus, S A Jensen, F D'Angelo, D Turchinovich, M Bonn, and E Canovas. Phonon-Electron Scattering Limits Free Charge Mobility in Methylammonium Lead Iodide Perovskites. *J. Phys. Chem. Lett.*, 6:4991–4996, 2015.

[161] T Seifert, S Jaiswal, M Sajadi, G Jakob, S Winnerl, M Wolf, M Kläui, and T Kampfrath. Ultrabroadband single-cycle terahertz pulses with peak fields of 300 kV cm1 from a metallic spintronic emitter. *Applied Physics Letters*, 110(25):252402, 2017.

[162] C F Klingshirn. *Semiconductor Optics*. Springer, page 166, first edition, 1997.

[163] Hannah J Joyce and Callum J Docherty and Qiang Gao and H Hoe Tan and Chennupati Jagadish and James Lloyd-Hughes and Laura M Herz and Michael B Johnston. Electronic properties of GaAs, InAs and InP nanowires studied by terahertz spectroscopy. *Nanotechnology*, 24(21):214006, 2013.

[164] James Lloyd-Hughes and Tae-In Jeon. A Review of the Terahertz Conductivity of Bulk and Nano-Materials. *J. Infrared Millim. Terahertz Waves*, 33(9):871–9252, 2012.

[165] Hannah J Joyce, Jessica L Boland, Christopher L Davies, Sarwat A Baig, and Michael B Johnston. A review of the electrical properties of semiconductor nanowires: insights gained from terahertz conductivity spectroscopy. *Semicond. Sci. Technol.*, 31(10):103003, 2016.

[166] Krzysztof Galkowski, Anatolie Mitioglu, Atsuhiko Miyata, Paulina Plochocka, Oliver Portugall, Giles E Eperon, Jacob Tse-Wei Wang, Thomas Stergiopoulos, Samuel D Stranks, Henry J Snaith, and Others. Determination of the exciton binding energy and effective masses for methylammonium and formamidinium lead tri-halide perovskite semiconductors. *Energy & Environmental Science*, 9(3):962–970, 2016.

[167] P C Makado and N C McGill. Energy levels of a neutral hydrogen-like system in a constant magnetic field of arbitrary strength. *Journal of Physics C: Solid State Physics*, 19(6):873, 1986.

[168] C Aldrich and R L Greene. Hydrogen-Like Systems in Arbitrary Magnetic Fields A Variational Approch. *Phys. Status Solidi B*, 93(1):343–350, 1979.

[169] Constantinos C Stoumpos, Christos D Malliakas, and Mercouri G Kanatzidis. Semiconducting Tin and Lead Iodide Perovskites with Organic Cations: Phase Transitions, High Mobilities, and Near-Infrared Photoluminescent Properties. *Inorg. Chem.*, 52(15):9019–9038, 2013.

[170] Mark T Weller, Oliver J Weber, Jarvist M Frost, and Aron Walsh. Cubic Perovskite Structure of Black Formamidinium Lead Iodide, α-$[HC(NH_2)_2]PbI_3$, at 298 K. *J. Phys. Chem. Lett.*, 6(16):3209–3212, 2015.

[171] Douglas H Fabini, Constantinos C Stoumpos, Geneva Laurita, Andreas Kaltzoglou, Athanassios G Kontos, Polycarpos Falaras, Mercouri G Kanatzidis, and Ram Seshadri. Reentrant Structural and Optical Properties and Large Positive Thermal Expansion in Perovskite Formamidinium Lead Iodide. *Angewandte Chemie International Edition*, 55(49):15392–15396, 2016.

[172] Tianran Chen, Benjamin J Foley, Changwon Park, Craig M Brown, Leland W Harriger, Jooseop Lee, Jacob Ruff, Mina Yoon, Joshua J Choi, and Seung-Hun Lee. Entropy-driven structural transition and kinetic trapping in formamidinium lead iodide perovskite. *Science advances*, 2(10):e1601650, 2016.

[173] Tianran Chen, Wei-Liang Chen, Benjamin J. Foley, Jooseop Lee, Jacob P. C. Ruff, J. Y. Peter Ko, Craig M. Brown, Leland W. Harriger, Depei Zhang, Changwon Park, Mina Yoon, Yu-Ming Chang, Joshua J. Choi, and Seung-Hun Lee. Origin of long lifetime of band-edge charge carriers in organicinorganic lead iodide perovskites. *Proceedings of the National Academy of Sciences*, 114(29):7519–7524, 2017.

[174] T Baikie, Y Fang, J M Kadro, M Schreyer, F Wei, S G Mhaisalkar, M Grätzel,

and T J White. Synthesis and crystal chemistry of the hybrid perovskite ($CH_3NH_3PbI_3$) for solid-state sensitized solar applications. *J. Chem. Mater. A*, 1:5628, 2013.

[175] Douglas H Fabini, Ting Ann Siaw, Constantinos C Stoumpos, Geneva Laurita, Daniel Olds, Katharine Page, Jerry G Hu, Mercouri G Kanatzidis, Songi Han, and Ram Seshadri. Universal Dynamics of Molecular Reorientation in Hybrid Lead Iodide Perovskites. *Journal of the American Chemical Society*, 139(46):16875–16884, 2017.

[176] M A Carignano, Y Saeed, S Assa Aravindh, Iman S Roqan, Jacky Even, and Claudine Katan. A close examination of the structure and dynamics of $HC(NH_2)_2PbI_3$ by MD simulations and group theory. *Physical Chemistry Chemical Physics*, 18(39):27109–27118, 2016.

[177] R E Wasylishen, Osvald Knop, and J B Macdonald. Cation rotation in methylammonium lead halides. *Solid State Communications*, 56(7):581–582, 1985.

[178] Douglas H Fabini, Tom Hogan, Hayden A Evans, Constantinos C Stoumpos, Mercouri G Kanatzidis, and Ram Seshadri. Dielectric and Thermodynamic Signatures of Low-Temperature Glassy Dynamics in the Hybrid Perovskites $CH_3NH_3PbI_3$ and $HC(NH_2)_2PbI_3$. *The Journal of Physical Chemistry Letters*, 7(3):376–381, 2016.

[179] María C Gélvez-Rueda, Nicolas Renaud, and Ferdinand C Grozema. Temperature Dependent Charge Carrier Dynamics in Formamidinium Lead Iodide Perovskite. *The Journal of Physical Chemistry C*, 121(42):23392–23397, 2017.

[180] Jarvist M Frost, Keith T Butler, Federico Brivio, Christopher H Hendon, Mark Van Schilfgaarde, and Aron Walsh. Atomistic origins of high-performance in hybrid halide perovskite solar cells. *Nano Lett.*, 14(5):2584–2590, 2014.

[181] R W Hellwarth and I Biaggio. Mobility of an Electron in a Multimode Polar Lattice. *Phys. Rev. B*, 60:299–307, 1999.

[182] Christopher L Davies, Juliane Borchert, Chelsea Q Xia, Rebecca L Milot, Hans Kraus, Michael B Johnston, and Laura M Herz. Impact of the organic cation on the optoelectronic properties of formamidinium lead triiodide. *The journal of physical chemistry letters*, 9:4502–4511, 2018.

[183] Gengfeng Zheng, Fernando Patolsky, Yi Cui, Wayne U Wang, and Charles M Lieber. Multiplexed electrical detection of cancer markers with nanowire sensor arrays. *Nat. Biotechnol.*, 23(10):1294–1301, 2005.

[184] Otto L Muskens, Silke L Diedenhofen, Maarten H M van Weert, Magnus T Borgström, Erik P A M Bakkers, and Jaime Gómez Rivas. Epitaxial Growth of Aligned Semiconductor Nanowire Metamaterials for Photonic Applications. *Adv. Funct. Mater.*, 18(7):1039–1046, 2008.

[185] Tevye Kuykendall, Philipp Ulrich, Shaul Aloni, and Peidong Yang. Complete composition tunability of InGaN nanowires using a combinatorial approach. *Nat. Mater.*, 6(12):951–956, dec 2007.

[186] Premila Mohan, Junichi Motohisa, and Takashi Fukui. Fabrication of InPInAs-InP core-multishell heterostructure nanowires by selective area metalorganic vapor phase epitaxy. *Appl. Phys. Lett.*, 88(13):133105, 2006.

[187] Katsuhiro Tomioka, Junichi Motohisa, Shinjiroh Hara, Kenji Hiruma, and Takashi Fukui. GaAs/AlGaAs Core Multishell Nanowire-Based Light-Emitting Diodes on Si. *Nano Lett.*, 10(5):1639–1644, apr 2010.

[188] Thomas J Kempa, James F Cahoon, Sun-Kyung Kim, Robert W Day, David C Bell, Hong-Gyu Park, and Charles M Lieber. Coaxial multishell nanowires

with high-quality electronic interfaces and tunable optical cavities for ultrathin photovoltaics. *Proc. Natl. Acad. Sci. U.S.A.*, 109(5):1407–1412, 2012.

[189] Lincoln J Lauhon, Mark S Gudiksen, Deli Wang, and Charles M Lieber. Epitaxial core-shell and core-multishell nanowire heterostructures. *Nature*, 420(6911):57–61, 2002.

[190] S A Dayeh, A V Gin, and S T Picraux. Advanced core/multishell germanium/silicon nanowire heterostructures: Morphology and transport. *Appl. Phys. Lett.*, 98(16):163112, 2011.

[191] Dhruv Saxena, Sudha Mokkapati, Patrick Parkinson, Nian Jiang, Qiang Gao, Hark Hoe Tan, and Chennupati Jagadish. Optically pumped room-temperature GaAs nanowire lasers. *Nat. Photon.*, 7(12):963–968, dec 2013.

[192] Fang Qian, Silvija Gradečak, Yat Li, Cheng-Yen Wen, and Charles M Lieber. Core/Multishell Nanowire Heterostructures as Multicolor, High-Efficiency Light-Emitting Diodes. *Nano Lett.*, 5(11):2287–2291, nov 2005.

[193] Jesper Wallentin, Nicklas Anttu, Damir Asoli, Maria Huffman, Ingvar Åberg, Martin H Magnusson, Gerald Siefer, Peter Fuss-Kailuweit, Frank Dimroth, Bernd Witzigmann, H Q Xu, Lars Samuelson, Knut Deppert, and Magnus T Borgström. InP Nanowire Array Solar Cells Achieving 13.8Exceeding the Ray Optics Limit. *Science*, 339(6123):1057–1060, 2013.

[194] Fang Qian, Yat Li, Silvija Gradecak, Hong-Gyu Park, Yajie Dong, Yong Ding, Zhong Lin Wang, and Charles M Lieber. Multi-quantum-well nanowire heterostructures for wavelength-controlled lasers. *Nat. Mater.*, 7(9):701–706, sep 2008.

[195] Ruoxue Yan, Daniel Gargas, and Peidong Yang. Nanowire photonics. *Nat. Photon.*, 3(10):569–576, oct 2009.

[196] Teng Shi, Howard E Jackson, Leigh M Smith, Nian Jiang, Qiang Gao, H Hoe Tan, Chennupati Jagadish, Changlin Zheng, and Joanne Etheridge. Emergence of Localized States in Narrow GaAs/AlGaAs Nanowire Quantum Well Tubes. *Nano Lett.*, 15(3):1876–1882, 2015.

[197] David Lindgren, Kenichi Kawaguchi, Magnus Heurlin, Magnus T Borgström, Mats-Erik Pistol, Lars Samuelson, and Anders Gustafsson. Optical characterization of InAs quantum wells and dots grown radially on wurtzite InP nanowires. *Nanotechnology*, 24(22):225203, 2013.

[198] Andrew B Greytak, Carl J Barrelet, Yat Li, and Charles M Lieber. Semiconductor nanowire laser and nanowire waveguide electro-optic modulators. *Appl. Phys. Lett.*, 87(15):151103, 2005.

[199] Gabriele Bulgarini, Michael E Reimer, Maaike Bouwes Bavinck, Klaus D Jöns, Dan Dalacu, Philip J Poole, Erik P A M Bakkers, and Val Zwiller. Nanowire Waveguides Launching Single Photons in a Gaussian Mode for Ideal Fiber Coupling. *Nano Lett.*, 14(7):4102–4106, jun 2014.

[200] Dhruv Saxena, Fan Wang, Qian Gao, Sudha Mokkapati, Hark Hoe Tan, and Chennupati Jagadish. Mode Profiling of Semiconductor Nanowire Lasers. *Nano Lett.*, page DOI:10.1021/acs.nanolett.5b01713, jul 2015.

[201] Alexander V Senichev, Vadim G Talalaev, Igor V Shtrom, Horst Blumtritt, George E Cirlin, Jörg Schilling, Christoph Lienau, and Peter Werner. Nanospectroscopic Imaging of Twinning Superlattices in an Individual GaAs-AlGaAs CoreShell Nanowire. *ACS Photonics*, 1(11):1099–1106, nov 2014.

[202] K. Hiruma, K. Tomioka, P. Mohan, L. Yang, J. Noborisaka, B. Hua, A. Hayashida, S. Fujisawa, S. Hara, J. Motohisa, and T. Fukui. Fabrication of

axial and radial heterostructures for semiconductor nanowires by using selective-area metal-organic vapor-phase epitaxy. *J. Nanotechnol.*, 2012:169284, 2012.

[203] N Jiang, Q Gao, P Parkinson, J Wong-Leung, S Mokkapati, S Breuer, H H Tan, C L Zheng, J Etheridge, and C Jagadish. Enhanced Minority Carrier Lifetimes in GaAs/AlGaAs CoreShell Nanowires through Shell Growth Optimization. *Nano Lett.*, 13(11):5135–5140, oct 2013.

[204] Alfred Leitenstorfer, Cornelius Fürst, Alfred Laubereau, Wolfgang Kaiser, Günther Tränkle, and Günter Weimann. Femtosecond Carrier Dynamics in GaAs Far from Equilibrium. *Phys. Rev. Lett.*, 76(9):1545–1548, feb 1996.

[205] W H Knox, R L Fork, M C Downer, D A B Miller, D S Chemla, C V Shank, A C Gossard, and W Wiegmann. Femtosecond Dynamics of Resonantly Excited Excitons in Room-Temperature GaAs Quantum Wells. *Phys. Rev. Lett.*, 54(12):1306–1309, mar 1985.

[206] Lyubomir Ahtapodov, Jelena Todorovic, Phillip Olk, Terje Mjåland, Patrick Slåttnes, Dasa L Dheeraj, Antonius T J van Helvoort, Bjørn-Ove Fimland, and Helge Weman. A Story Told by a Single Nanowire: Optical Properties of Wurtzite GaAs. *Nano Lett.*, 12(12):6090–6095, dec 2012.

[207] Guoqiang Zhang, Kouta Tateno, Haruki Sanada, Takehiko Tawara, Hideki Gotoh, and Hidetoshi Nakano. Synthesis of GaAs nanowires with very small diameters and their optical properties with the radial quantum-confinement effect. *Appl. Phys. Lett.*, 95(12):123104, 2009.

[208] I Zelinka, P N Suganthan, G Chen, V Snášel, A Abraham, and O Rössler. *Nostradamus 2014: Prediction, Modeling and Analysis of Complex Systems.* Advances in Intelligent Systems and Computing. Springer, 2014.

[209] Marco Patriarca, Anirban Chakraborti, Kimmo Kaski, and Guido Germano. Kinetic Theory Models for the Distribution of Wealth: Power Law from Overlap of Exponentials. In Arnab Chatterjee, Sudhakar Yarlagadda, and BikasK Chakrabarti, editors, *Econophysics of Wealth Distributions SE - 10*, New Economic Windows, pages 93–110. Springer Milan, 2005.

[210] Mohammad Montazeri, Howard E Jackson, Leigh M Smith, Jan M Yarrison-Rice, Jung-Hyun Kang, Qiang Gao, Hark Hoe Tan, and Chennupati Jagadish. Transient Rayleigh Scattering: A New Probe of Picosecond Carrier Dynamics in a Single Semiconductor Nanowire. *Nano Lett.*, 12(10):5389–5395, 2012.

[211] Yuda Wang, Howard E Jackson, Leigh M Smith, Tim Burgess, Suriati Paiman, Qiang Gao, Hark Hoe Tan, and Chennupati Jagadish. Carrier Thermalization Dynamics in Single Zincblende and Wurtzite InP Nanowires. *Nano Lett.*, 14(12):7153–7160, 2014.

[212] Veer Dhaka, Jani Oksanen, Hua Jiang, Tuomas Haggren, Antti Nykänen, Reza Sanatinia, Joona-Pekko Kakko, Teppo Huhtio, Marco Mattila, Janne Ruokolainen, Srinivasan Anand, Esko Kauppinen, and Harri Lipsanen. Aluminum-Induced Photoluminescence Red Shifts in CoreShell GaAs/AlxGa1xAs Nanowires. *Nano Lett.*, 13(8):3581–3588, jul 2013.

[213] Moïra Hocevar, Le Thuy Thanh Giang, Rudeesun Songmuang, Martien den Hertog, Lucien Besombes, Joël Bleuse, Yann-Michel Niquet, and Nikos T Pelekanos. Residual strain and piezoelectric effects in passivated GaAs/AlGaAs core-shell nanowires. *Appl. Phys. Lett.*, 102(19):191103, 2013.

[214] Y Chen, R Cingolani, L C Andreani, F Bassani, and J Massies. Photoluminescence in quantum well and bulk GaAs: a direct comparative study. *Il Nuovo Cimento D*, 10(7):847–859, 1988.

[215] T Voss, C Bekeny, L Wischmeier, H Gafsi, S Börner, W Schade, A C Mofor, A Bakin, and A Waag. Influence of exciton-phonon coupling on the energy position of the near-band-edge photoluminescence of ZnO nanowires. *Appl. Phys. Lett.*, 89(18):182107, 2006.

[216] Nian Jiang, Jennifer Wong-Leung, Hannah J Joyce, Qiang Gao, Hark Hoe Tan, and Chennupati Jagadish. Understanding the True Shape of Au-Catalyzed GaAs Nanowires. *Nano Lett.*, 14(10):5865–5872, oct 2014.

[217] Sudha Mokkapati, Dhruv Saxena, Nian Jiang, Patrick Parkinson, Jennifer Wong-Leung, Qiang Gao, Hark Hoe Tan, and Chennupati Jagadish. Polarization Tunable, Multicolor Emission from CoreShell Photonic IIIV Semiconductor Nanowires. *Nano Lett.*, 12(12):6428–6431, dec 2012.

[218] Tyler Westover, Reese Jones, J. Y. Huang, George Wang, Elaine Lai, and a. Alec Talin. Photoluminescence, thermal transport, and breakdown in joule-heated GaN nanowires. *Nano Lett.*, 9(1):257–263, jan 2009.

[219] Changlin Zheng, Jennifer Wong-Leung, Qiang Gao, Hark Hoe Tan, Chennupati Jagadish, and Joanne Etheridge. Polarity-Driven 3-Fold Symmetry of GaAs/AlGaAs Core Multishell Nanowires. *Nano Lett.*, 13(8):3742–3748, 2013.

[220] Stefan Birner, T Zibold, T Andlauer, T Kubis, M Sabathil, A Trellakis, and Peter Vogl. nextnano: General Purpose 3-D Simulations. *Electron Devices, IEEE Transactions on*, 54(9):2137–2142, sep 2007.

[221] E Fermi. *Nuclear Physics: A Course Given by Enrico Fermi at the University of Chicago*. Midway reprint. University of Chicago Press, 1950.

[222] Fausto Rossi. Quantum Fermi's golden rule for semiconductor nanodevices. *Phys. Status Solidi C*, 5(1):35–38, 2008.

[223] Wang Zhiping, McMeekin David P., Sakai Nobuya, van Reenen Stephan, Wojciechowski Konrad, Patel Jay B., Johnston Michael B., and Snaith Henry J. Efficient and AirStable MixedCation Lead MixedHalide Perovskite Solar Cells with nDoped Organic Electron Extraction Layers. *Advanced Materials*, 29(5):1604186, 2017.

[224] Juan Arturo Alanis, Dhruv Saxena, Sudha Mokkapati, Nian Jiang, Kun Peng, Xiaoyan Tang, Lan Fu, Hark Hoe Tan, Chennupati Jagadish, and Patrick Parkinson. Large-scale statistics for threshold optimization of optically pumped nanowire lasers. *Nano letters*, 17(8):4860–4865, 2017.